THEORETICAL STUDIES OF THE STRUCTURE-PROPERTY RELATIONSHIPS OF HOLE- AND ELECTRON-TRANSPORT MATERIALS FOR ORGANIC PHOTOVOLTAIC APPLICATIONS

A Dissertation
Presented to
The Academic Faculty

by

Laxman Pandey

In Partial Fulfillment
of the Requirements for the Degree
Doctor of Philosophy in the
School of Chemistry and Biochemistry

Georgia Institute of Technology
August 2013

Copyright © 2013 by Laxman Pandey

THEORETICAL STUDIES OF THE STRUCTURE-PROPERTY RELATIONSHIPS OF HOLE- AND ELECTRON-TRANSPORT MATERIALS FOR ORGANIC PHOTOVOLTAIC APPLICATIONS

Approved by:

Professor Jean-Luc Brédas, Advisor
School of Chemistry and Biochemistry
Georgia Institute of Technology

Professor C. David Sherrill
School of Chemistry and Biochemistry
Georgia Institute of Technology

Professor Joseph W. Perry
School of Chemistry and Biochemistry
Georgia Institute of Technology

Professor Bernard Kippelen
School of Electrical and Computer Engineering
Georgia Institute of Technology

Professor Seth R. Marder
School of Chemistry and Biochemistry
Georgia Institute of Technology

Date Approved: 05/14/2013

ACKNOWLEDGEMENTS

This work has come together as a result of unflagging love, encouragement, and support of a number of people. First and foremost, I would like to express my deepest respect and gratitude to my advisor, Professor Jean-Luc Brédas, for providing me with an opportunity to conduct research under his supervision. His humility, patience, encouragement, and support have played immense role in my growth both as a scientist and a human being. I am also grateful for the support, guidance, and advise from my committee members, Professors Joseph W. Perry, Seth R. Marder, C. David Sherrill, and Bernard Kippelen.

I would like to extend my sincere gratitude to Drs. Chad Risko, John Sears, Veaceslav Corpceanu, Yuanping Yi, Joseph Norton, and Massimo Malagoli for their mentorship. They introduced me to the field of computational chemistry and shared their knowledge and know-how. My deepest appreciation goes to Dr. Risko for editing and correcting most of my work. Heartfelt thanks to the friends and colleagues at the Brédas group for the fun filled and educative working environment. Plenty of thanks and appreciation also goes out to Professors Seth R. Marder, Bernard Kippelen, Zhenan Bao, Michael McGehee, Alan Sellinger, and Alberto Salleo and Drs. Steve Barlow, Lauren Polander, Shree P. Tiwari, Rajib Mondal, Sangwon Ko, and Eric Hoke for fruitful collaborations.

Outside of the academic world, I would like to thank Prakiti didi and Raj Sr. dai for the help and support as friends and guardians. They have provided me with a home away from home for the last four years. The times spent with them along with Yogi dai,

Archana didi, Raj dai, Krishna didi, and Arun dai, as members of an extended family, will never be forgotten.

Most importantly, I would like to thank my parents, Mr. Pitambar Pandey and Mrs. Ganga Devi Pandey, for their sacrifices, unconditional love, and invaluable life-lessons. The optimism and persistence with which they have faced various adversities have provided me with the strength and spirit to face all challenges. My utmost respect to my eldest brother Suraj – words are not enough to appreciate his sacrifice in giving up his schooling, at such a tender age, to help provide for the family. I want him to know that his struggle is my strength. Brothers Suman and Sushil have been an integral part of my life. I cherish their friendship and togetherness through the thick and thin in life. My gratitude to Bhaujus and adorable Chori and Choras for the moments of joy in the past and in the future. This would not have been possible had in not been for the support and encouragement of my family and this dissertation belongs to them as much as it belongs to me.

Finally, I would like to thank my wife, Isha. Her love, belief, and inspirations have helped me strive forward even in the toughest times.

TABLE OF CONTENTS

LIST OF TABLES

LIST OF FIGURES

LIST OF ABBREVIATIONS

BHJ	Bulk-heterojunction
BT	Benzothiadiazole
B2T	Benzobisthiadiazole
CDFT	Constrained Density Functional Theory
CPDT	Cyclopentadithiophene
CPDP	Cyclopentadibenzene
CT	Charge-Transfer
CR	Charge-Recombination
CS	Charge-Separation
DA	Donor-Acceptor
DFT	Density Functional Theory
DFTB	Density Functional based Tight Binding
EA	Electron Affinity
ECE	Electron Collecting Electrode
EQE	External Quantum Efficiency
ETM	Electron-Transport Materials
FF	Fill Factor
GGA	Generalized Gradient Approximation
GIXS	Grazing Incidence X-ray Scattering
HCE	Hole Collecting Electrode
HF	Hartree-Fock
HOMO	Highest Occupied Molecular Orbital
HTM	Hole-Transport Materials

IP	Ionization Potential
IQE	Internal Quantum Efficiency
J_{SC}	Short-Circuit Current
LDA	Local Density Approximation
LRC	Long-Range Corrected
LUMO	Lowest Unoccupied Molecular Orbital
NTO	Natural Transition Orbitals
OPV	Organic Photovoltaics
$PC_{61}BM$	methanofullerene[6,6]-phenyl-C_{61}-butyric acid methyl ester
$PC_{71}BM$	methanofullerene[6,6]-phenyl-C_{71}-butyric acid methyl ester
PCE	Power Conversion Efficiency
RT	Room Temperature
SIE	Self-Interaction Error
T-Y-T	Thiophene-Acceptor-Thiophene
TDDFT	Time-Dependent Density Functional Theory
V_{OC}	Open-Circuit Voltage
XC	Exchange-Correlation

SUMMARY

Donor-acceptor and thiophene based π-conjugated molecules and polymers, along with fullerene derivatives, are extensively used active components in the photoactive layer of organic photovoltaic devices. In this dissertation, we make use of several computational methodologies to investigate structure-property relationships of these organic systems in their molecular forms. We begin with an overview of the field of organic photovoltaics and some of the important problems in organic solar cells that are currently being investigated. This is then followed by a brief review of the electronic-structure methods (*e.g*. Hartree-Fock theory, Density Functional Theory, and Time-dependent Density Functional Theory) that are employed.

We then present the main results of the dissertation. Chapter 3 provides a broad overview on how changes to the donor-acceptor copolymer chemical structure impacts its intrinsic geometric, electronic, and optical properties. Chapter 4 focuses on the characterization of the lowest excited-states and optical absorption spectra in donor-acceptor copolymers. In Chapter 5, we investigate the effects of alkyl side-chain placements in the π-conjugated backbone of oligothiophenes and how that impacts their intramolecular properties as well as the oligomer:fullerene interfacial interactions. Chapter 6 presents our investigation on the role of oligomer:fullerene configuration and reorganization energy on exciton-dissociation and charge-recombination processes. Finally, a synopsis of the work and further considerations are presented in Chapter 7.

CHAPTER 1

INTRODUCTION

With the ever increasing demand for energy and the concern for environmental impact from the use of petrochemical sources, the need for clean, sustainable energy sources is of prime concern for humanity today.[1-3] Almost limitless in supply and carbon neutral, the sun is a promising source. The surface of the earth receives more energy from the sun in one hour [4.3 x 10^{17} kJ] than the current total world energy usage in a year [4.1 x 10^{17} kJ]. Since the first demonstration of conversion of light into electricity by Becquerel,[4] progress has been made in photovoltaics technology and the current state-of-the-art inorganic solar cells boast power conversion efficiencies (PCE) about 40%.[5] Commercially available solar panels currently available have efficiencies approaching 20%.

Organic-based solar cells (organic photovoltaic (OPV) devices) have some ways go to be on par with the inorganic ones on the performance level, but signs are encouraging as recent years have witnessed steady improvements.[6] There are important differences between organic and inorganic semiconductors.[7] Organic semiconductors have π-electrons along their conjugated path and the intermolecular interactions are π-π, van der Waals, and / or dipole-dipole based. Inorganic semiconductors (such as silicon or gallium arsenide) have electrons delocalized along the σ-bonded lattice. These differences contribute to large differences in the dielectric constant of the materials – the organic materials having dielectric constants much lower compared to inorganic ones. This directly affects the nature of excitations upon illumination of the materials, providing a key difference between the organic and inorganic solar cells. Free electrons and

holes are created instantly at room temperature in inorganic solar cells upon absorption of photons whereas in the organic solar cells, the electrons and holes are still strongly bound through Coulombic forces. Different architectures have been successfully implemented in organic solar cells to separate these electron-hole pairs,[8,9] but the performance still remains well below those of the inorganic solar cells.[6,10] The drive for bringing improvements on organic semiconductors based solar cells, however, still remains strong.[11,12]

The push for organic semiconductors stems from their potential for flexible, lightweight, and lower-cost applications, and also to their synthetic accessibility.[13] Besides OPVs, organic semiconductors have potential uses in a range of (photo)electronic applications including light emitting diodes, field-effect transistors, switches, and photodiodes.[14] To make improvements there is a need for the study, understanding, and development of materials and device properties. The study of materials and device operation processes are therefore highly desired.

1.1. Organic photovoltaic devices and key processes

Organic photovoltaic devices convert photon energy to electrical energy. Some of the commonly used OPV device configurations are shown in **Figure 1.1**. The basic OPV device architecture has organic materials sandwiched between two electrodes. For successful separation of the Coulombically-bound electron-hole pairs into separated charges, the photoactive layer is comprised of hole-transport and electron-transport materials (HTM and ETM, respectively). The HTM and ETM have small ionization potential (IP) and large electron affinity (EA), respectively, that provides a driving force for exciton-dissociation. The HTM and ETM are assembled in either a simple bilayer configuration or a phase-separated nanostructured bulk-heterojunction[9] (BHJ). The BHJ also allows for a larger surface contact between the two materials. Indium tin oxide and aluminum are typically used as hole and electron collecting

electrodes (HCE and ECE), respectively. Many devices also include poly(3,4-ethylenedioxythiophene):poly(styrenesulfonate) as a hole-transporting layer.

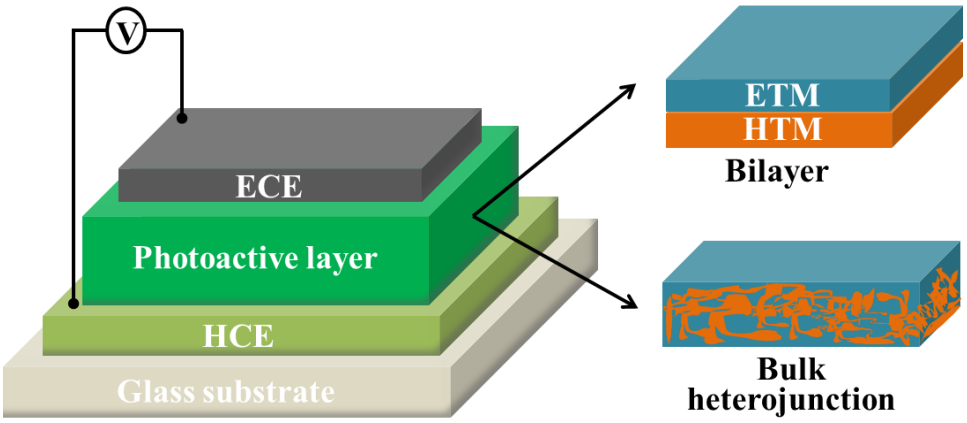

Figure 1.1 Schematic illustration of an OPV device: the photoactive layer is sandwiched between the hole- and electron-collecting electrodes (HCE and ECE, respectively).

For the conversion of light into electrical energy, five major steps are required to be fulfilled. These are illustrated in **Figure 1.2** and detailed below.

1.1.1. Absorption

The first stage of OPV operation is absorption of photons by the photoactive layer that leads to the formation of Coulombically bound electron-hole pairs called excitons.[15] This excited state provides a theoretical upper limit to the voltage one can get from a photovoltaic device. It is important to note that the exciton binding energies in organic semiconductors usually reach several hundreds of meV while they are only a few meV in inorganic semiconductors.

Having a photoactive layer that can maximize the absorption of photons (without sacrificing other key parameters) is a critical step towards building an efficient OPV device. Substantial research efforts have been made on the search for materials that can absorb photons efficiently throughout the entire solar spectrum, especially in the near-infrared range. The study

of donor-acceptor based small optical-gap semiconductors (a substantial part of this dissertation) is a step towards that direction.[16-20]

1.1.2. Exciton migration

Once created, the exciton needs to reach the hole- and electron-transport material interface for charge transfer to occur. If not already at the interface, the exciton has to diffuse through the material and migrate towards the interface. The diffusion process is described by the diffusion length, a parameter dependent on the material.[21] Radiative and non-radiative decay pathways provide loss mechanisms of the exciton state. Therefore, for high device performance, it is critical that such loss mechanisms are minimized to ensure that a maximum number of excitons successfully reach the interface. It has to be noted however, that when there is strong intermixing of the HTM and ETM in the photoactive layer, for instance, from intercalation of fullerene derivatives in between polymer side-chains, excitons can readily dissociate (without the involvement of the migration process) within 100 fs.[22]

1.1.3. Exciton dissociation

Upon photoexcitation, the exciton needs to dissociate into free charge carriers for the generation of a photocurrent. Unlike in the inorganic solar cells where the created exciton can easily dissociate into free charge carriers at room temperature, the exciton in the photoactive layer of an OPV device needs an energetic driving force for the dissociation to occur. Use of HTM and ETM provides that driving force through the charge-transfer process where the electron transfers from the HTM to the ETM as an intermediate step towards exciton dissociation (creation of free charge carriers through charge separation is the other step in the exciton-dissociation process). As described above, in many device architectures, the HTM and ETM are

arranged in nanostructured bulk-heterojunction.[9] This heterojunction provides a larger surface contact between the two materials when compared to a bilayer structure. The nanostructure also provides an opportunity for excitons to find closely located interface sites for the charge-transfer process to occur. To prevent decay of the photoexcited excitons back to ground state, it is critical that the excitons find these interfaces in close proximity because their diffusion lengths are small (< 20 nm) and their lifetimes are short (few hundred picoseconds to nanoseconds).[23,24]

1.1.4. Charge transport

Once separated, it is essential that the charges travel through the materials towards the charge collecting electrodes. The efficiency at which these charges are transported is very much dependent on how ordered the material structure is. A well-ordered structure has the possibility of having large carrier mobilities whereas disordered structures are prone to poor mobilities. Disorder provides sites for charge traps and the charge mobility is severely affected. The ordering and the structure is not only a function of the materials that make the device but are also largely dependent on the processing conditions. Molecular packing, morphology, disorder, and defects are important parameters that affect charge transport and govern the efficiency of a device. These subjects have attracted extensive interest within the OPV community.[25-30]

1.1.5. Charge collection

Photocurrent generation in OPVs require the charges to be collected at the charge collecting electrodes. The geometry, topology, nature of the metal-organic layer interface, and electrode work functions play important roles on the charge collection mechanism in a device.

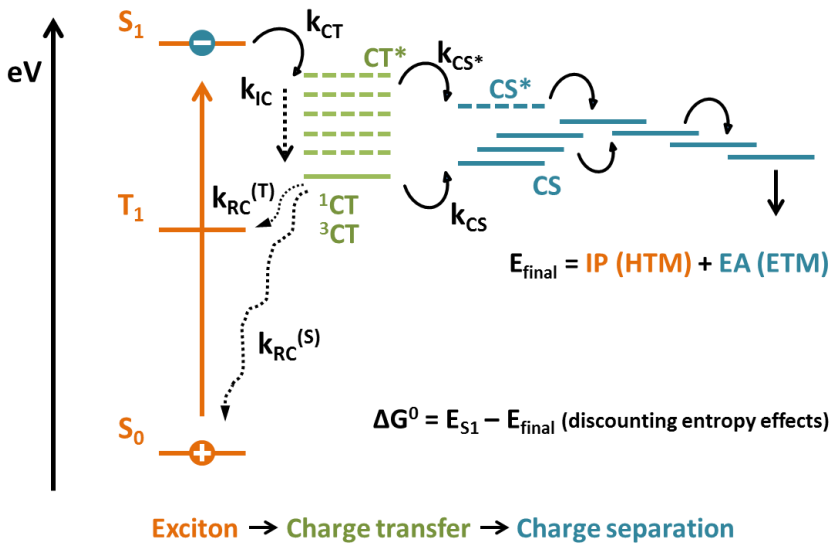

Figure 1.2 Electronic state diagram representing the mechanism of the photo-induced charge-carrier formation in organic photovoltaic cells: formation of exciton and exciton-dissociation at the HTM:ETM interface (through charge-transfer and charge separation).

1.2. Device performance

The performance of a photovoltaic device is determined based upon its current-voltage characteristics both in the dark and under illumination. A typical current-voltage plot is presented in **Figure 1.3**. The current density under illumination at zero applied voltage is the short-circuit current density J_{SC}. The voltage where the current density under illumination is zero is the open-circuit voltage V_{OC}, which is also the maximum voltage the device can supply. The fill factor *FF* of a device is defined as

$$FF = \frac{J_{\max} * V_{\max}}{V_{OC} * J_{SC}} \qquad (1.1)$$

and gives the fraction of maximum attainable power to the theoretical power maximum. The power conversion efficiency *PCE* is related to these parameters as

$$PCE = \frac{J_{SC} * V_{OC} * FF}{P_{IN}} \tag{1.2}$$

and represents the efficiency of a device under standard illumination conditions (air mass 1.5) at standard temperature and pressure relative to the incident power P_{IN}.

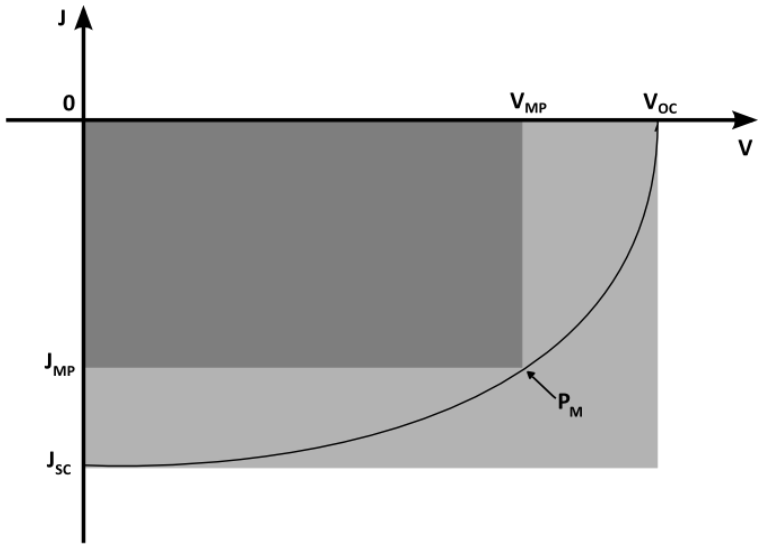

Figure 1.3 Current-voltage characteristics of a typical bulk-heterojunction solar cell: open-circuit voltage (V_{OC}), short-circuit current (J_{SC}), power maximum (P_M), fill factor (FF, ratio of areas between dark gray and light gray rectangles).

Other important parameters include the internal quantum efficiency *IQE*, which is the ratio of the number of electrons that contribute to the photocurrent to the number of incident photons absorbed by the photoactive layer. The external quantum efficiency *EQE*, on the other hand, is the ratio between the number of electrons that contribute to the photocurrent and the number of incident photons. The *EQE* quantifies the ability of an OPV to convert incident photons into photocurrent. Absorption losses – through i) relaxation of excitons that fail to diffuse to and separate at the photoactive materials' interface, ii) recombination of the geminate electron-hole pair at the interface (geminate recombination), iii) recombination of the dissociated or free charge carriers (non-geminate recombination) – and losses during charge collection are

events and processes that hamper the efficiency of a device. These are bound to be affected by both the intrinsic material properties and material interactions that influence packing, morphology, surface contacts, defects, etc. Increasing device performance requires minimizing these losses and maximizing J_{SC}, V_{OC}, and *FF*.

1.3. Inherent problems in OPV

There are a number of fundamental issues in OPV that the scientific community is trying to understand and resolve. Among them the following are some that relate to the work pertaining to this dissertation.

1.3.1. Absorption throughout the solar spectrum

The majority of the solar irradiance spans from ca. 4.5 – 0.8 eV (approximately 280 – 1500 nm).[31] Typical organic materials however absorb photons larger in energy than 2.1 eV (ca. 600 nm). This accounts to only ca. 20% of the total available photons.[31] If one can extend the absorption to ca. 1.2 eV, one can harvest over 50% of the available photons. Considering 100% external quantum efficiency, this brings a 300% increase in the cumulative short circuit current density (from ca. 11 to 34 mA/cm^2). These numerical estimates have inspired the OPV community to consider low optical-gap materials in the photoactive medium in a view to yield improvements on the device efficiency by bringing better overlap with the solar spectrum. Similarly, tandem cells using low band-gap materials have also gathered a lot of attention.[32,33]

1.3.2. Absorption vs. exciton migration

Balancing or resolving the trade-off between absorption and exciton migration is a major challenge in OPV. The photoactive layer is required to be thicker than the optical absorption

length L_A for efficient absorption of incident light. Given that the typical absorption coefficient α of OPV materials is ca. 10^5/cm and the L_A is the inverse of α, the photoactive layer thickness for absorption of majority of incident light is > 100 nm. The typical exciton diffusion lengths for organic semiconductors used in the photoactive layer of an OPV unfortunately is < 20 nm. Therefore, the hole- and electron-transport materials interface must be present within the 20 nm distance of each other to ensure the excitons diffuse to the interface before they decay. There have been a few architectures developed to tackle this problem. Although light trapping schemes (photonic crystal geometries,[34] folded architecture,[25,26] reflectivity mirrors[25,27]) have been developed, the bulk heterojunction[9] is the most widely used structure.

1.3.3. Current losses through decay and recombination

Besides the contribution of losses during absorption and exciton migration, processes related to exciton dissociation, charge transport and charge collection also contribute significantly to photocurrent losses. The efficiency of photocurrent generation in a photovoltaic device depends on the balance between charge-carrier generation, recombination and transport. These are bound to be affected by parameters such as the charge-carrier mobility, charge-carrier lifetime, electric-field strength, drift lengths, charge traps, impurities, etc. that are functions of both the molecular and bulk properties including the processing conditions.[35,36]

1.3.4. Voltage losses

As represented in **Equation 1.2**, the open-circuit voltage is an important parameter that influences the performance of a photovoltaic device. Considering typical optical gaps of HTM (1.6 eV) and V_{OC} (0.6 – 1.0 V) for OPV devices, there is a 0.6 – 1.0 V loss. Understanding the origin of V_{OC} and the parameters that contribute to this loss are subjects of current research.[37-39]

Although many factors including the dark current, photoconductivity, temperature, carrier recombination have been proposed to affect the V_{OC}, the largest contribution to the loss is the energy offset between the ionization potential *IP* and the electron affinity *EA* of the hole- and electron-transport materials (in the literature this offset is often referenced as the difference between highest occupied molecular orbital (HOMO) and lowest unoccupied molecular orbital (LUMO) energy of the HTM and ETM in the photoactive layer).[40] Finding appropriate materials that can help reduce this energy offset to minimize the voltage loss is a subject of interest to the OPV community.

1.4. Low optical-gap materials

To improve photocurrent generation in OPV devices, there has been a tremendous push for low optical-gap materials as the HTM in the photoactive layer.[20] This is in a view to attaining absorption over a large spectral region, including the near infrared where the photonic flux is at maximum.[41] One effective way of attaining low optical-gap materials is through a combination of electron-rich electron-donating (donor, D) and electron-deficient/electron-withdrawing (acceptor, A) fragments in the conjugated backbone (such materials are commonly referred as donor-acceptor (DA) materials).[42] The donor fragment contributes to a small IP (high-lying HOMO energy) while the acceptor contributes to a large EA (low-lying LUMO energy); this combination results in a material with smaller HOMO-LUMO and optical gaps. Such donor-acceptor based low optical-gap materials have been used in BHJ solar cells in both polymeric and small molecule forms with varying device successes.[10,19,43-47,48,49,50,51] A large part of this dissertation is related to understanding the structural and electronic properties of these materials and realizing the best theoretical methods to properly describe these properties.

1.5. Electron-transport materials

Fullerene-based systems are known for efficient electron transfer when used with hole-transport materials in a bulk-heterojunction solar cell,[9] and are the most widely used electron-transport materials.[52-54] They have good charge-carrier transport properties, but have some drawbacks as they absorb weakly in the visible spectrum, are highly expensive (as they require sophisticated fabrication technologies in preparation and purification stages), and contribute to large energy loss during electron transfer due to a large band offset (because of large electron affinity). Therefore efforts in the direction of finding alternatives that can absorb well in the visible spectrum, have easier synthetic and purification routes, and minimize energy losses are ongoing.[55-59]

1.6. Motivation and outline of the thesis

The optimization of key processes in the operation of organic photovoltaic devices, as mentioned above, requires understanding of both the molecular and bulk material properties. The first two processes (absorption and exciton dissociation) are functions of molecular properties of the hole- and electron-transport materials and their interactions at the interface. In relevance to these two processes, we aim to understand the molecular properties of the donor-acceptor-based and other hole-transport materials and their interactions with the electron-transport materials at the interface.

Since the early nineties, a substantial amount of work on the characterization and use of donor-acceptor copolymers for OPV applications has been published.[10,19,43-47] Much of the experimental (and theoretical) literature is fraught with scattered and inconsistent reports of the redox – e.g. thin film or solution studies using different standard electrodes – and optical – e.g.

thin film or solution studies, absorption maxima or absorption onsets, normalized absorption profiles – properties. Such inconsistencies make it difficult to understand the relationship between one set of systems and the next. We therefore use quantum-chemical methods to study structure-property relationships of a large number of donor-acceptor systems (based upon specific donor/acceptor fragment combinations) to provide a systematic study within the same framework. These studies provide information and insights relevant to absorption and charge-transfer processes.

Due to the presence of electron-rich and electron-deficient components in these donor-acceptor systems, the low-lying excited states have some amounts of charge-transfer character that conventional density functionals have difficulties properly describing. Gaining a good understanding of these lowest excited states (excitons) is critical since the charge-generation process directly depends on the dissociation of these excitons at the HTM:ETM interface. Therefore, we further use modern long-range corrected density functionals with system specific range separation parameters to study the low-lying excited states of select donor-acceptor materials.

Thiophene based systems have been extensively used as hole-transport materials in conjunction with fullerene based electron-transport materials. Various alkyl groups are attached to the thiophene units to influence solubility and other properties. Within structure-property context, we investigate how specific attachments of these alkyl groups and thiophene spacers influence geometric properties that impact ionization potential, HTM:ETM configurations and interactions, and charge-transfer state energies that influence key parameters such as the open-circuit voltage.

Exciton-dissociation and charge-recombination processes are important factors that can determine whether the photoexcitation results to useful photocurrent or a loss. To improve on the performance, the exciton-dissociation rate needs to be maximized and the recombination rate needs to be reduced. We investigate how these rates are affected for various hole- and electron-transport material configurations.

In Chapter 2, we review the computational methods relevant to the work related to this dissertation. We begin with the Schrödinger equation and Born-Oppenheimer approximation and describe Hartree-Fock. Then we move on to Kohn-Sham density functional theory and the density functional approximations. Next, we briefly describe time-dependent density functional theory for excited states. The Chapter ends with a list of software and program suites that were used during the course of the work.

In Chapter 3, we highlight the impact of the various donor-acceptor constructs on the oscillator strengths of the low-lying excited states. This property is of key importance regarding the ability of the material to efficiently absorb light. We also discuss the impact of the thiophene spacers – often stated to be included in the donor-acceptor copolymer design to simply aid in planarization of the backbone – both on the electronic structure and the optical properties, in particular the oscillator strengths. Our results demonstrate key ideas such as the influence of the steric effects on the copolymer geometric structure; the impact of frontier orbital energetic alignment and torsion angles between the donor/acceptor components on the level of mixing and localization/delocalization of copolymer HOMO and LUMO wave functions, and how this affects the material absorption strength in addition to the transport and optical gaps.

The focus of the work in Chapter 4 is to characterize the lowest excited states of a series of donor-acceptor copolymers that have been used in some of the best performing bulk-heterojunction organic solar cells. We apply state-of-the-art long-range corrected functionals for the characterization. We find that these functionals require the use of system specific range separation parameters. Without optimization of the parameter for each system, these functionals over-estimate the excitation energies.

In chapter 5, we investigate the influence of alkyl substitutions and placement of thiophene spacers on the backbone twisting of thiophene based hole-transport materials. The alkyl substitutions greatly influence the torsional angles that impact the materials ionization potential. The alkyl groups and the backbone twisting determine the material configurations and interactions with the (fullerene based) electron-transport materials. This has an influence on the charge-transfer energies that in turn affect parameters such as the open-circuit voltage.

Building up on the study of individual molecular properties of hole- and electron-transport materials, the work in Chapter 6 investigates interactions between HTM and ETM based on various configurations. The influence on binding energies, electronic couplings, charge-transfer state energies, as well as exciton-dissociation and charge-recombination rates is evaluated as a function of the molecular configurations. We find that the binding energies and electronic couplings are strongly influenced by positions and configurations. Importantly, charge-recombination rates are affected more strongly than exciton-dissociation rates as a function of varying reorganization energies.

Overall, this work uses a number of quantum-chemical methods to study molecular properties of donor-acceptor and thiophene-based hole-transport materials and fullerene based electron-transport materials of relevance to bulk-heterojunction organic solar cells. The results present insights on the material design and structure-property relationships that are relevant to absorption and exciton-dissociation processes in OPV devices.

1.7. References

(1) Baum, R. *Chem. Eng. News* **2005**, *83*, 5.

(2) Lewis, N. S. *MRS Bull.* **2007**, *32*, 808.

(3) Figgen, D.; Rauhut, G.; Dolg, M.; Stoll, H. *Chem. Phys.* **2005**, *311*, 227.

(4) Becquerel, E. *C. R. Acad. Sci.* **1839**, *9*, 561.

(5) Green, M. A.; Emery, K.; King, D. L.; Hishikawa, Y.; Warta, W. *Prog. Photovoltaics Res. Appl.* **2006**, *14*, 455.

(6) Green, M. A.; Emery, K.; Hishikawa, Y.; Warta, W.; Dunlop, E. D. *Prog. Photovoltaics Res. Appl.* **2012**, *20*, 606.

(7) Sun, S.-S.; Dalton, L. R. *Introduction to organic electronic and optoelectronic materials and devices*; CRC Press: Boca Ralton, FL, 2008.

(8) Tang, C. W. *Appl. Phys. Lett.* **1986**, *48*, 183.

(9) Yu, G.; Gao, J.; Hummelen, J. C.; Wudl, F.; Heeger, A. J. *Science* **1995**, *270*, 1789.

(10) Lin, Y. Z.; Li, Y. F.; Zhan, X. W. *Chem. Soc. Rev.* **2012**, *41*, 4245.

(11) Nelson, J. *Mater. Today* **2011**, *14*, 462.

(12) Mishra, A.; Bäuerle, P. *Angew. Chem. Int. Ed.* **2012**, *51*, 2020.

(13) Brabec, C. J.; Hauch, J. A.; Schilinsky, P.; Waldauf, C. *MRS Bulletin* **2005**, *30*, 50.

(14) So, F. *Organic electronics : materials, processing, devices and applications*; CRC Press: Boca Raton, FL, 2010.

(15) Gregg, B. A. *MRS Bull.* **2005**, *30*, 20.

(16) Havinga, E. E.; ten Hoeve, W.; Wynberg, H. *Synth. Met.* **1993**, *55*, 299.

(17) Roncali, J. *Chem. Rev.* **1997**, *97*, 173.

(18) van Mullekom, H. A. M.; Vekemans, J.; Havinga, E. E.; Meijer, E. W. *Mater. Sci. Eng. R.* **2001**, *32*, 1.

(19) Cheng, Y. J.; Yang, S. H.; Hsu, C. S. *Chem. Rev.* **2009**, *109*, 5868.

(20) Facchetti, A. *Chem. Mater.* **2010**, *23*, 733.

(21) Peumans, P.; Yakimov, A.; Forrest, S. R. *J. Appl. Phys.* **2003**, *93*, 3693.

(22) Banerji, N.; Cowan, S.; Leclerc, M.; Vauthey, E.; Heeger, A. J. *J. Am. Chem. Soc.* **2010**, *132*, 17459.

(23) Lunt, R. R.; Giebink, N. C.; Belak, A. A.; Benziger, J. B.; Forrest, S. R. *J. Appl. Phys.* **2009**, *105*, 053711.

(24) Mikhnenko, O. V.; Azimi, H.; Scharber, M.; Morana, M.; Blom, P. W. M.; Loi, M. A. *Energy Environ. Sci.* **2012**, *5*, 6960.

(25) Kline, R. J.; McGehee, M. D. *J. Macromol. Sci., Polym. Rev.* **2006**, *46*, 27.

(26) Chabinyc, M. L. *Polym. Rev.* **2008**, *48*, 463.

(27) Ray, B.; Alam, M. A. *Sol. Energy Mater. Sol. Cells* **2012**, *99*, 204.

(28) Kumar, A.; Hong, Z.; Sista, S.; Yang, Y. *Adv. Energy Mater.* **2011**, *1*, 124.

(29) Ojala, A.; Burckstummer, H.; Hwang, J.; Graf, K.; von Vacano, B.; Meerholz, K.; Erk, P.; Wurthner, F. *J. Mater. Chem.* **2012**, *22*, 4473.

(30) Jurow, M. J.; Hageman, B. A.; DiMasi, E.; Nam, C.-Y.; Pabon, C.; Black, C. T.; Drain, C. M. *J. Mater. Chem. A* **2013**.

(31) Bundgaard, E.; Krebs, F. C. *Sol. Energy Mater. Sol. Cells* **2007**, *91*, 954.

(32) Ameri, T.; Dennler, G.; Lungenschmied, C.; Brabec, C. J. *Energy Environ. Sci.* **2009**, *2*, 347.

(33) Dou, L.; You, J.; Yang, J.; Chen, C.-C.; He, Y.; Murase, S.; Moriarty, T.; Emery, K.; Li, G.; Yang, Y. *Nat. Photonics* **2012**, *6*, 180.

(34) Duche, D.; Simon, J. J.; Escoubas, L.; Torchio, P.; Le Rouzo, J.; Vervisch, W.; Flory, F. In *ICTON Mediterranean Winter Conference,2009. ICTON-MW 2009. 3rd* 2009, p 1.

(35) Servaites, J. D.; Ratner, M. A.; Marks, T. J. *Energy Environ. Sci.* **2011**, *4*, 4410.

(36) Nalwa, K. S.; Kodali, H. K.; Ganapathysubramanian, B.; Chaudhary, S. *Appl. Phys. Lett.* **2011**, *99*, 263301.

(37) Scharber, M. C.; Mühlbacher, D.; Koppe, M.; Denk, P.; Waldauf, C.; Heeger, A. J.; Brabec, C. J. *Adv. Mater.* **2006**, *18*, 789.

(38) W. J. Potscavage, J.; Yoo, S.; Kippelen, B. *Appl. Phys. Lett.* **2008**, *93*, 193308.

(39) Vandewal, K.; Tvingstedt, K.; Gadisa, A.; Inganas, O.; Manca, J. V. *Phys. Rev. B: Condens. Matter* **2010**, *81*, 125204.

(40) Rand, B. P.; Burk, D. P.; Forrest, S. R. *Phys. Rev. B* **2007**, *75*, 115327.

(41) Smestad, G. P.; Krebs, F. C.; Lampert, C. M.; Granqvist, C. G.; Chopra, K. L.; Mathew, X.; Takakura, H. *Sol. Energy Mater. Sol. Cells* **2008**, *92*, 371.

(42) Havinga, E. E.; ten Hoeve, W.; Wynberg, H. *Polym. Bull.* **1992**, *29*, 119.

(43) Park, S. H.; Roy, A.; Beaupre, S.; Cho, S.; Coates, N.; Moon, J. S.; Moses, D.; Leclerc, M.; Lee, K.; Heeger, A. J. *Nat. Photonics* **2009**, *3*, 297.

(44) Chen, H.-Y.; Hou, J.; Zhang, S.; Liang, Y.; Yang, G.; Yang, Y.; Yu, L.; Wu, Y.; Li, G. *Nat. Photonics* **2009**, *3*, 649.

(45) He, Z.; Zhong, C.; Huang, X.; Wong, W.-Y.; Wu, H.; Chen, L.; Su, S.; Cao, Y. *Adv. Mater.* **2011**, *23*, 4636.

(46) Walker, B.; Tamayo, A. B.; Dang, X.-D.; Zalar, P.; Seo, J. H.; Garcia, A.; Tantiwiwat, M.; Nguyen, T.-Q. *Adv. Funct. Mater.* **2009**, *19*, 3063.

(47) Sun, Y.; Welch, G. C.; Leong, W. L.; Takacs, C. J.; Bazan, G. C.; Heeger, A. J. *Nat. Mater.* **2012**, *11*, 44.

(48) http://www.osa-direct.com/osad-news/solarmer-energy-achieves-record-efficiency-of-813-for-organic-photovoltaic-device.html (accessed November 2012)

(49) http://www.pv-tech.org/news/nrel_validates_konarkas_8.3_power_plastic_efficiency_record (accessed November 2012)

(50) http://www.plusplasticelectronics.com/energy/polyera-serves-up-new-ink-line-for-polymer-solar-cells-45729.aspx (accessed November 2012)

(51) http://www.businesswire.com/news/home/20120821005794/en/Phillips-66-China-University-Technology-Solarmer-Energy (accessed November 2012)

(52) Lenes, M.; Morana, M.; Brabec, C. J.; Blom, P. W. M. *Adv. Funct. Mater.* **2009**, *19*, 1106.

(53) He, Y.; Chen, H.-Y.; Hou, J.; Li, Y. *J. Am. Chem. Soc.* **2010**, *132*, 5532.

(54) Ross, R. B.; Cardona, C. M.; Guldi, D. M.; Sankaranarayanan, S. G.; Reese, M. O.; Kopidakis, N.; Peet, J.; Walker, B.; Bazan, G. C.; Van Keuren, E.; Holloway, B. C.; Drees, M. *Nat. Mater.* **2009**, *8*, 208.

(55) Bloking, J. T.; Han, X.; Higgs, A. T.; Kastrop, J. P.; Pandey, L.; Norton, J. E.; Risko, C.; Chen, C. E.; Brédas, J.-L.; McGehee, M. D.; Sellinger, A. *Chem. Mater.* **2011**, *23*, 5484.

(56) Lin, Y.; Cheng, P.; Li, Y.; Zhan, X. *Chem. Commun.* **2012**, *48*, 4773.

(57) Nevil, N.; Ling, Y.; Mierloo, S. V.; Kesters, J.; Piersimoni, F.; Adriaensens, P.; Lutsen, L.; Vanderzande, D.; Manca, J.; Maes, W.; Doorslaer, S. V.; Goovaerts, E. *Phys. Chem. Chem. Phys.* **2012**, *14*, 15774.

(58) Nielsen, C. B.; Voroshazi, E.; Holliday, S.; Cnops, K.; Rand, B. P.; McCulloch, I. *J. Mater. Chem. A* **2013**.

(59) Abdullah, S. M.; Ahmad, Z.; Aziz, F.; Sulaiman, K. *Org. Electron.* **2012**, *13*, 2532.

CHAPTER 2

ELECTRONIC STRUCTURE METHODS FOR CONJUGATED ORGANICS

This chapter will review the methods used in this study of the ground- and excited-state properties of π-conjugated materials. We begin with the non-relativistic Schrödinger equation and its simplified form using the Born-Oppenheimer approximation and Hartree-Fock theory. A brief overview of density functional theory and density functional approximations that incorporate various exchange-correlation energy functionals, including recent long-range corrected functionals, will then be provided. The section that follows describes time-dependent density functional theory used to describe excited-state properties. The concepts, notation, and terminology discussed in this chapter are mostly taken from Jensen,[1] Szabo and Ostlund,[2] and Koch and Holstein.[3]

2.1. Schrödinger equation and the total electronic Hamiltonian

The quantum nature of a stationary system of particles can be described by the Schrödinger equation:

$$\hat{H}\left|\Psi_i\right\rangle = E_i\left|\Psi_i\right\rangle \tag{2.1}$$

an eigenvalue equation, where $\hat{H}$ is the non-relativistic molecular Hamiltonian, $\left|\Psi_i\right\rangle$ the wave function, and E_i an allowed energy level. The Hamiltonian for a system of M nuclei and N electrons is given in atomic units by:

$$\hat{\boldsymbol{H}} = -\frac{1}{2}\sum_{\boldsymbol{A}=1}^{\boldsymbol{M}}\frac{1}{\boldsymbol{M_A}}\nabla_{\boldsymbol{A}}^2 - \frac{1}{2}\sum_{\boldsymbol{i}=1}^{\boldsymbol{N}}\nabla_{\boldsymbol{i}}^2 - \sum_{\boldsymbol{i}=1}^{\boldsymbol{N}}\sum_{\boldsymbol{A}=1}^{\boldsymbol{M}}\frac{\boldsymbol{Z_A}}{\boldsymbol{r_{iA}}} + \sum_{\boldsymbol{A}=1}^{\boldsymbol{M}}\sum_{\boldsymbol{B}>1}^{\boldsymbol{M}}\frac{\boldsymbol{Z_A Z_B}}{\boldsymbol{R_{AB}}} + \sum_{\boldsymbol{i}=1}^{\boldsymbol{N}}\sum_{\boldsymbol{j}>1}^{\boldsymbol{N}}\frac{1}{\boldsymbol{r_{ij}}} \qquad (2.2)$$

with the first two terms describing the kinetic energy of the nuclei and electrons, $\hat{T}_N$ and $\hat{T}_e$, respectively. The potential energy part of the Hamiltonian that represents the electrostatic interaction among the nuclei and the electrons is given by the remaining three terms where the first represents nucleus-electron attractions, $\hat{V}_{Ne}$, the second term the nucleus-nucleus repulsions, $\hat{V}_N$, and the third term the electron-electron repulsions, $\hat{V}_e$. The Schrödinger equation is formally a second-order differential equation in 3(M + N) variables and is closed-form solvable for only simple systems. Approximations are therefore necessary for solutions of non-trivial chemical systems.

2.2. Born-Oppenheimer approximation

As a consequence of large disparity in the nuclear and electronic masses (even the lightest nucleus, ^{1}H, is roughly 1800 times heavier than an electron and this increases with the atomic number; for example, the mass ratio is over 22,000 for the carbon nucleus),[4] the electronic motion almost instantaneously accommodates to the motion of the nuclei. This forms the basis for the *Born-Oppenheimer approximation* where electrons move within a stationary field of fixed nuclei. As a result, the total Hamiltonian (**Equation 2.2**) simplifies to the so-called electronic Hamiltonian:

$$\hat{H}_{elec} = \hat{T}_e + \hat{V}_{Ne} + \hat{V}_{ee} \qquad (2.3)$$

and leads to the electronic Schrödinger equation:

$$\hat{H}_{elec}\Psi_{el} = E_{elec}\Psi_{elec} \qquad (2.4)$$

where the electronic wave function, Ψ_{el}, depends only on the electron coordinates (that are a function of the nuclear coordinates). The total energy is, therefore:

$$E_{tot} = E_{elec} + E_{nuc} \tag{2.5}$$

where E_{nuc} is the (fixed) nuclear repulsion energy.

2.3. Independent-particle approximation and the Hartree-Fock theory

The independent-particle model transforms the electronic Schrödinger equation (**Equation 2.4**) from a solution of an N-electron Hamiltonian to that of N 1-electron Hamiltonians. The wave function becomes a simple product of spin-orbital wave functions for each electron:

$$\Psi^{HP}(\boldsymbol{x}_1, \boldsymbol{x}_2, \cdots, \boldsymbol{x}_N) = \chi_i(\boldsymbol{x}_1)\chi_j(\boldsymbol{x}_2)\cdots\chi_k(\boldsymbol{x}_N)\,. \tag{2.6}$$

This expression is also known as the Hartree product; however, it is important to note that the expression does not satisfy the antisymmetry principle.

In Hartree-Fock (HF) theory, the wave function is represented as a single Slater determinant of spin-orbitals as:

$$\Psi(\boldsymbol{x}_1, \boldsymbol{x}_2, ..., \boldsymbol{x}_N) = \frac{1}{\sqrt{N!}}\begin{vmatrix} \chi_i(\boldsymbol{x}_1) & \chi_j(\boldsymbol{x}_1) & \cdots & \chi_k(\boldsymbol{x}_1) \\ \chi_i(\boldsymbol{x}_2) & \chi_j(\boldsymbol{x}_2) & \cdots & \chi_k(\boldsymbol{x}_2) \\ \vdots & \vdots & \cdots & \vdots \\ \chi_i(\boldsymbol{x}_N) & \chi_j(\boldsymbol{x}_N) & \cdots & \chi_k(\boldsymbol{x}_N) \end{vmatrix}. \tag{2.7}$$

The spin orbital, $\chi(\boldsymbol{x})$, is defined as:

$$\chi(\boldsymbol{x}) = \begin{cases} \psi(\boldsymbol{r})\alpha \\ \text{or} \\ \psi(\boldsymbol{r})\beta \end{cases} \tag{2.8}$$

Minimizing the expectation value of the electronic Hamiltonian with respect to the spin-orbitals yields the HF energy:

$$E_{HF} = \sum_{i}^{N} \left(i \left| \hat{h} \right| i \right) + \frac{1}{2} \sum_{i}^{N} \sum_{j}^{N} \left(ii \left| \hat{h} \right| jj \right) - \left(ij \left| \hat{h} \right| ji \right) \tag{2.9}$$

where

$$\left(\mathrm{i} \left| \hat{\mathrm{h}} \right| \mathrm{i} \right) = \int \chi_i^*(\boldsymbol{x}_1) \left\{ -\frac{1}{2} \nabla_i^2 - \sum_{A}^{M} \frac{\boldsymbol{Z}_A}{\boldsymbol{r}_{iA}} \right\} \chi_i(\boldsymbol{x}_1) d\boldsymbol{x}_1 \tag{2.10}$$

defines the contribution due to the kinetic energy and the electron-nucleus attraction and

$$\left(\mathrm{ii} \left| \hat{\mathrm{h}} \right| \mathrm{jj} \right) = \int \int \left| \chi_i(\boldsymbol{x}_1) \right|^2 \frac{1}{\boldsymbol{r}_{12}} \left| \chi_j(\boldsymbol{x}_2) \right|^2 d\boldsymbol{x}_1 d\boldsymbol{x}_2 \tag{2.11}$$

$$\left(\mathrm{ij} \left| \hat{\mathrm{h}} \right| \mathrm{ji} \right) = \int \int \chi_i(\boldsymbol{x}_1) \chi_j^*(\boldsymbol{x}_1) \frac{1}{\boldsymbol{r}_{12}} \chi_j(\boldsymbol{x}_2) \chi_i^*(\boldsymbol{x}_2) d\boldsymbol{x}_1 d\boldsymbol{x}_2 \tag{2.12}$$

are the so-called Coulomb and exchange integrals, respectively.

Typically, the orbitals are expanded using a finite basis set of atom-centered Gaussian orbitals. The orbitals are optimized variationally to yield the lowest single-determinant energy subject to spatial and spin symmetry restrictions and orbital orthonormality conditions.

HF is a mean-field theory that excludes explicit electron-electron correlation. Although the ground-state properties of a well-behaved conjugated system are reasonably well represented by the HF method, the lack of explicit electron-electron correlation brings limitations to the description of properties like the optical spectra, excited-state geometries, and transition structures. Many techniques and methods have been developed to incorporate the correlation effects to varying degrees; some examples include configuration interaction,[5] Møller-Plesset perturbation theory,[6] and coupled cluster[7] methods.

2.3.1. Density functional theory

Density functional theory (DFT) is one of the most widely used methods for studying the ground-state electronic structure of π-conjugated systems. The basis of DFT comes from the seminal work of Kohn, Hohenberg, and Sham[8,9] that relates the ground-state electronic energy of a system to its ground-state electronic density. As opposed to the many-body wave function methods where the wave function is a function of 3N variables, the electronic density in DFT is a function of three spatial variables. This reformulation in the solving of the electronic Schrödinger equation using electronic density instead of the wave function allows the use of DFT to study systems with sizes that would be very difficult to treat with wave function-based methods.

2.3.1.1. The Hohenberg-Kohn theorems

The first theorem by Hohenberg and Kohn states: *The ground-state energy from Schrödinger's equation is a unique functional of the electron density*. In other words, there exists a one-to-one mapping between the ground-state external potential and the ground-state electron density. Therefore, the average value of an observable can be written as a functional of the electron density:

$$\langle A \rangle = A[\rho(\boldsymbol{r})] \tag{2.13}$$

and the total energy of a system can be expressed as:

$$E_v[\rho] = T_v[\rho] + E_{Ne}[\rho] + E_{ee}[\rho] \tag{2.14}$$

where $T_v[\rho]$ represents the kinetic energy while $E_{Ne}[\rho]$ and $E_{ee}[\rho]$ represent electrostatic interactions accounting for nuclear-electron attraction and electron-electron repulsion respectively. The universal functional of Hohenberg and Kohn consists of the kinetic and electron-electron terms:

$$E_{HK}[\rho] = T_v[\rho] + E_{ee}[\rho]. \quad (2.15)$$

As the functional form of equation (**2.15**) is not known exactly, the Schrödinger equation is solved using approximations. The electron-electron term in the universal functional includes non-classical (quantum) electron-electron interaction terms including exchange, correlation, and self-interaction.

The second Hohenberg-Kohn theorem, essentially the variational principle, states that *the electron density that minimizes the energy of the overall functional is the true electron density corresponding to the full solution of the Schrödinger equation*. This allows one to variationally calculate the ground-state energy and density from a trial density.

2.3.1.2. The Kohn-Sham theorem

Since a good working representation of the kinetic energy through the density has proved difficult, the application of true density functional theory (orbital-free models) in computational chemistry has been far from ideal. This problem has been addressed through the introduction of orbitals by Kohn and Sham.[9] They proposed the reduction of the difficult many-body problem of interacting electrons in a static external potential by a simpler system of non-interacting electrons in an effective potential. The Kohn-Sham formalism splits the kinetic energy functional into two parts: the first an orbital-based term that can be calculated exactly, while the second term is a small correction term. The exact kinetic energy of the non-interacting reference system, T_S, is

$$T_S = -\frac{1}{2}\sum_{i}^{N}\langle \varphi_i | \nabla^2 | \varphi_i \rangle. \quad (2.16)$$

The kinetic energy correction term is accounted for by introducing the following expression:

$$F[\rho(\mathbf{r})] = T_S[\rho(\mathbf{r})] + J[\rho(\mathbf{r})] + E_{XC}[\rho(\mathbf{r})] \quad (2.17)$$

where the *exchange-correlation energy*, E_{XC}, is defined as:

$$E_{XC}[\rho] \equiv \left(T[\rho] - T_S[\rho]\right) + \left(E_{ee}[\rho] - J[\rho]\right) = T_C[\rho] + E_{ncl}[\rho]. \tag{2.18}$$

In addition to the non-classical electron-electron interaction contribution, the exchange-correlation energy functional contains the kinetic energy correction mentioned above. In other words, E_{XC} contains everything that is unknown and needs to be approximated. The Kohn-Sham Hamiltonian that describes a system of non-interacting particles is therefore:

$$\left[-\frac{1}{2}\nabla^2 + \upsilon_{KS}(r)\right]\varphi_i(r) = \varepsilon_i\varphi_i(r). \tag{2.19}$$

The effective Kohn-Sham potential υ_{KS} is chosen such that:

$$\rho(\boldsymbol{r}) = \sum_{i}^{N} \left|\varphi_i(\boldsymbol{r})\right|^2, \tag{2.20}$$

where ρ is the ground-state density and φ the Kohn-Sham orbitals. The effective potential υ_{KS} includes the external potential υ_{ext} (the nuclei-electron Coulomb interaction), the Hartree potential or mean-field Coulomb potential (Coulomb repulsion of an electron density with itself) and the exchange-correlation potential υ_{XC} as illustrated in the following equation

$$\upsilon_{KS} = \upsilon_{ext}(\boldsymbol{r}) + \int \frac{\rho(\boldsymbol{r}')}{\left|\boldsymbol{r} - \boldsymbol{r}'\right|} d\boldsymbol{r}' + \upsilon_{XC}(\boldsymbol{r}). \tag{2.21}$$

The exact expression for the exchange-correlation potential υ_{XC} or the explicit form of exchange-correlation energy E_{XC} is not known, therefore υ_{XC} is simply defined as

$$\upsilon_{XC}(\boldsymbol{r}) = \frac{\delta E_{XC}}{\delta\rho(\boldsymbol{r})} \tag{2.22}$$

and needs to be approximated.

2.3.1.3. Approximate exchange-correlation functionals

Although Kohn-Sham DFT is exact in principle, it requires approximation to the exchange-correlation energy E_{XC} to be practically applicable. In terms of total electron density $\rho(r)$ and exchange-correlation energy density per electron $\varepsilon_{\boldsymbol{XC}}$, an approximation to E_{XC} is expressed as:

$$E_{XC} = \int \rho(\boldsymbol{r})\varepsilon_{\boldsymbol{XC}}(\boldsymbol{r})\, d\boldsymbol{r} \,. \tag{2.23}$$

As discussed by Perdew and co-workers,[10] a ladder of approximations can be used to construct $\varepsilon_{\boldsymbol{XC}}(\boldsymbol{r})$ as a function of local ingredients at $\boldsymbol{r}$. The rungs are defined by the kind of information included, with the higher rungs representing functionals that include an increased level of physical information.

Local density approximation

The local density approximation (LDA) is the simplest approximation to the true Kohn-Sham functional. In LDA, it is assumed that the density in the locality of $\boldsymbol{r}$ is a slowly varying function and can be treated as a uniform electron gas. In actuality, the key to the success of the functional varies on how the electron density varies. The valence electron density in many bulk materials (e.g. metals) varies slowly; therefore, LDA was extensively used in the solid-state physics community. For atoms and molecules, however, the electron density is no longer slowly varying; hence, LDA does not perform well for molecular properties.

The analytical form of the exchange energy in LDA is known. This is also true for the correlation energy in the high and low density limits.[1] For intermediate densities, Monte Carlo

simulations of the uniform gas have been used to determine the correlation energy.[11] Some of the most popular LDA correlation functionals are VWN[12] and PW.[13]

Generalized gradient approximation

One way to account for the inhomogeneity of the electron density in molecular systems is to include information on the gradient of the electron density $\nabla\rho(\boldsymbol{r})$ along with the local density at $\boldsymbol{r}$. Functionals that include gradients of the electron density are known as generalized gradient approximations (GGA). Amongst the many GGA functionals that have been developed, the ones that have gained wide usage in the computational chemistry community are: B88[14] and PBE[15] for exchange and LYP[16] and PBE[15] for correlation.

Meta-GGA

A logical direction to take to bring about improvements in functionals from LDA and GGA would be to include higher- (second-) order derivative of the electron density $\nabla^2\rho(\boldsymbol{r})$. In addition to the Laplacian of density, these functionals also include the orbital kinetic energy density, $\tau = (1/2)\nabla^2\rho(\boldsymbol{r})\sum_{\boldsymbol{i}}\left|\nabla\varphi_{\boldsymbol{i}}\right|^2$. TPSS[17] and the Minnesota functionals (from Truhlar and Zhao)[18] are amongst the most widely used meta-GGA functionals.

Hybrid functionals

The exchange contribution to the total energy is generally much larger than the correlation contribution. Including (non-local) exact HF exchange to the semi local functional is a further way to improve DFT functionals.[19] This fractional mixing of exact (HF) exchange with DFT exchange and correlation functionals is the idea behind the hybrid functionals.

One of the underlying reasons for the improvements brought about by the hybrid functionals is the reduction of the self-interaction error from the admixture of HF exchange in the functional (HF theory is self-interaction-free from the cancelation of the Coulomb and exchange energies, see **Equation 2.9**).

The general form of a hybrid functional is given by the following expression:

$$E_{XC} = a_0 E_X^{HF} + (1 - a_0) E_X^{DFA} + E_C^{DFA}. \quad (2.24)$$

One such global hybrid functional is B3LYP.[16,20,21] This functional has been used successfully to characterize the properties of a large array of molecular systems. The functional form of B3LYP is:

$$E_{XC}^{B3LYP} = 0.2E_X^{HF} + 0.8E_X^{LDA} + 0.72\Delta E_X^{B88} + 0.81E_C^{LYP} + 0.19E_C^{VWN}. \quad (2.25)$$

There are many other hybrid functionals that have been developed and used.[22-25] There is no global rule on the optimal amount of exact HF exchange as this seems to vary with both the systems under study and the properties of interest.

Range separated hybrid functionals

The recent years have seen many developments in density functional approximations.[26] Because of the relevance to this thesis work (Chapter 4), we will briefly discuss range-separated hybrid functionals, particularly the long-range corrected (LRC) functionals.

In LRC functionals, the Coulomb operator is separated into short- and long-range as first introduced by the teams of Savin[27] and Gill.[28] Typically, the range separation is brought about using the error function as shown below:

$$\frac{1}{r} = \frac{erfc(\omega)}{r} + \frac{erf(\omega)}{r}. \quad (2.26)$$

The separation of the Coulomb operator was introduced to take advantage of both the strengths and shortcomings of the local and semilocal approximations to the exchange-correlation functional. These approximations perform well in the short range, but suffer from incorrect behavior of the exchange-correlation potential at long range. This is a consequence of the inexactness of the one-electron density or the self-interaction error (SIE).

In order to correct for this, the exchange DFA is mixed with HF (exact) exchange in the long-range. This is because for atomic and molecular systems, the SIE-free HF potential has the correct asymptotic limit.

Baer, Kronik, and co-workers have pioneered finding optimal range-separation parameters in such LRC functionals.[29,30] A general form of the LRC functional is expressed below (it should be noted that $E_X^{SR\text{-}HF}$ can be entirely omitted in some long-range corrected functionals).

$$E_{XC}^{LC\text{-}DFA} = E_X^{SR\text{-}DFA} + E_X^{SR\text{-}HF} + E_X^{LR\text{-}HF} + E_C^{DFA}. \qquad (2.27)$$

For solid-state considerations, however, the corrections are carried out for the short-range. Such screened functionals include HF in the short-range and DFA in the long-range.[31-33]

2.3.2. Time-dependent density functional theory

Time-dependent density functional theory (TDDFT) is an extension of DFT with a time-dependent external potential. It is a method used to study excited states or properties of interest involving time-dependent fields and has become a powerful tool in the study of the excited-state properties of molecules. The central idea to TDDFT is the Runge-Gross theorem[34] that proves a one-to-one correspondence between the external time-dependent potential $\upsilon_{XC}(\boldsymbol{r},t)$ and the electronic density $\rho(\boldsymbol{r},t)$ from a fixed initial state.

Figure 2.1 shows a comparison of DFT with TDDFT. The upper bullets show that DFT [TDDFT] is based on the Hohenberg-Kohn[8] [Runge-Gross][34] theorem that maps one-to-one correspondence between external potential [external time-dependent potential] and the density [time-dependent density]. The second bullets show that the total energies [total actions] are unique functionals of the density. The third bullets signify that for the time-independent problem, the ground state of a system can be determined through the minimization of the total energy functional. For time-dependent systems, the time-dependent problem can be solved by the stationary point of the functional action (an analogous quantity to the energy).[35] For DFT [TDDFT], the stationary points of the total energy [action] give the exact density of the system.

DFT (Hohenberg-Kohn)	TDDFT (Runge-Gross)
• $v(\boldsymbol{r}) \Leftrightarrow \rho(\boldsymbol{r})$	• $v(\boldsymbol{r},t) \Leftrightarrow \rho(\boldsymbol{r},t)$
• $\langle \Phi \vert \hat{\mathrm{H}} \vert \Phi \rangle = \mathrm{E}[\rho]$	• $\int_{t_0}^{t_1} \left\langle \Phi(t) \middle\vert i\frac{\partial}{\partial t}\hat{\mathrm{H}}(t) \middle\vert \Phi(t) \right\rangle dt = A[\rho]$
• $\frac{\delta E[\rho]}{\delta \rho(r)} = 0 \quad \Rightarrow \rho(\boldsymbol{r})$	• $\frac{\delta A[\rho]}{\delta \rho(\boldsymbol{r},t)} = 0 \quad \Rightarrow \rho(\boldsymbol{r},t)$

Figure 2.1 Side by side comparison of DFT with TDDFT.

Under small external time-dependent potential (for example, optical absorption), one can use perturbation theory instead of solving the full time-dependent Kohn-Sham equations to determine the behavior of the system. Linear response TDDFT can be used to evaluate excited-state energies and transition moments to derive the optical absorption properties of molecular systems. Linear response TDDFT, however, becomes inadequate for situations where the time-dependent potential is strong such as for molecules under strong laser fields.

2.4. Software

The electronic-structure methods used or discussed in this dissertation were implemented in the following software packages: Gaussian03 (Revision E.01),[36] Gaussian09 (Revision B.01),[37] Q-Chem 3.2,[38] NWChem,[39] and DFTB+.[40]

2.5. References

(1) Jensen, F. *Introduction to computational chemistry*; Wiley: Chichester ; New York, 2007.

(2) Szabo, A.; Ostlund, N. S. *Modern quantum chemistry : introduction to advanced electronic structure theory*; Dover Publications: Mineola, N.Y., 1996.

(3) Koch, W.; Holthausen, M. C. *A Chemist's Guide to Density Functional Theory*; Second ed.; WILEY-VCH, 2001.

(4) http://physics.nist.gov/cuu/Constants/index.html

(5) Sherrill, C. D.; Schaefer Iii, H. F. In *Adv. Quantum Chem.*; Per-Olov Löwdin, J. R. S. M. C. Z., Erkki, B., Eds.; Academic Press: 1999; Vol. Volume 34, p 143.

(6) Møller, C.; Plesset, M. S. *Phys. Rev.* **1934**, *46*, 618.

(7) Bartlett, R. J. *J. Phys. Chem.* **1989**, *93*, 1697.

(8) Hohenberg, P.; Kohn, W. *Phys. Rev.* **1964**, *136*, B864.

(9) Kohn, W.; Sham, L. J. *Phys. Rev.* **1965**, *140*, A1133.

(10) Perdew, J. P.; Ruzsinszky, A.; Tao, J.; Staroverov, V. N.; Scuseria, G. E.; Csonka, G. I. *J. Chem. Phys.* **2005**, *123*, 062201.

(11) Ceperley, D. M.; Alder, B. J. *Phys. Rev. Lett.* **1980**, *45*, 566.

(12) Vosko, S. H.; Wilk, L.; Nusair, M. *Can. J. Phys.* **1980**, *58*, 1200.

(13) Perdew, J. P.; Wang, Y. *Phys. Rev. B* **1992**, *45*, 13244.

(14) Becke, A. D. *Phys. Rev. A: At., Mol., Opt. Phys.* **1988**, *38*, 3098.

(15) Perdew, J. P.; Burke, K.; Ernzerhof, M. *Phys. Rev. Lett.* **1996**, *77*, 3865.

(16) Lee, C.; Yang, W.; Parr, R. G. *Phys. Rev. B* **1988**, *37*, 785.

(17) Tao, J.; Perdew, J. P.; Staroverov, V. N.; Scuseria, G. E. *Phys. Rev. Lett.* **2003**, *91*, 146401.

(18) Zhao, Y.; Truhlar, D. *Theor. Chem. Acc.* **2008**, *120*, 215.

(19) Becke, A. D. *J. Chem. Phys.* **1993**, *98*, 1372.

(20) Becke, A. D. *J. Chem. Phys.* **1993**, *98*, 5648.

(21) Stephens, P. J.; Devlin, F. J.; Chabalowski, C. F.; Frisch, M. J. *J. Phys. Chem.* **1994**, *98*, 11623.

(22) Boese, A. D.; Handy, N. C. *J. Chem. Phys.* **2002**, *116*, 9559.

(23) Perdew, J. P.; Ernzerhof, M.; Burke, K. *J. Chem. Phys.* **1996**, *105*, 9982.

(24) Staroverov, V. N.; Scuseria, G. E.; Tao, J.; Perdew, J. P. *J. Chem. Phys.* **2003**, *119*, 12129.

(25) Staroverov, V. N.; Scuseria, G. E.; Tao, J.; Perdew, J. P. *J. Chem. Phys.* **2004**, *121*, 11507.

(26) Cohen, A. J.; Mori-Sánchez, P.; Yang, W. *Chem. Rev.* **2011**, *112*, 289.

(27) Savin, A.; Flad, H.-J. *Int. J. Quantum Chem.* **1995**, *56*, 327.

(28) Gill, P. M. W.; Adamson, R. D.; Pople, J. A. *Mol. Phys.* **1996**, *88*, 1005.

(29) Refaely-Abramson, S.; Baer, R.; Kronik, L. *Phys. Rev. B* **2011**, *84*, 075144.

(30) Baer, R.; Livshits, E.; Salzner, U. *Annu. Rev. Phys. Chem.* **2010**, *61*, 85.

(31) Bylander, D. M.; Kleinman, L. *Phys. Rev. B* **1990**, *41*, 7868.

(32) Heyd, J.; Scuseria, G. E.; Ernzerhof, M. *J. Chem. Phys.* **2003**, *118*, 8207.

(33) Krukau, A. V.; Vydrov, O. A.; Izmaylov, A. F.; Scuseria, G. E. *J. Chem. Phys.* **2006**, *125*, 224106.

(34) Runge, E.; Gross, E. K. U. *Phys. Rev. Lett.* **1984**, *52*, 997.

(35) Marques, M. A. L.; Gross, E. K. U. *Annu. Rev. Phys. Chem.* **2004**, *55*, 427.

(36) Frisch, M. J. T., G. W.; Schlegel, H. B.; Scuseria, G. E.; Robb, M. A.; Cheeseman, J. R.; Montgomery, Jr., J. A.; Vreven, T.; Kudin, K. N.; Burant, J. C.; Millam, J. M.; Iyengar, S. S.; Tomasi, J.; Barone, V.; Mennucci, B.; Cossi, M.; Scalmani, G.; Rega, N.; Petersson, G. A.; Nakatsuji, H.; Hada, M.; Ehara, M.; Toyota, K.; Fukuda, R.; Hasegawa, J.; Ishida, M.; Nakajima, T.; Honda, Y.; Kitao, O.; Nakai, H.; Klene, M.; Li, X.; Knox, J. E.; Hratchian, H. P.; Cross, J. B.; Bakken, V.; Adamo, C.; Jaramillo, J.; Gomperts, R.; Stratmann, R. E.; Yazyev, O.; Austin, A. J.; Cammi, R.; Pomelli, C.; Ochterski, J. W.; Ayala, P. Y.; Morokuma, K.; Voth, G. A.; Salvador, P.; Dannenberg, J. J.; Zakrzewski, V. G.; Dapprich, S.; Daniels, A. D.; Strain, M. C.; Farkas, O.; Malick, D. K.; Rabuck, A. D.; Raghavachari, K.; Foresman, J. B.; Ortiz, J. V.; Cui, Q.; Baboul, A. G.; Clifford, S.; Cioslowski, J.; Stefanov, B. B.; Liu, G.; Liashenko, A.; Piskorz, P.; Komaromi, I.; Martin, R. L.; Fox, D. J.; Keith, T.; Al-Laham, M. A.; Peng, C. Y.; Nanayakkara, A.; Challacombe, M.; Gill, P. M. W.; Johnson, B.; Chen, W.; Wong, M. W.; Gonzalez, C.; and Pople, J. A; E.01 ed.; Gaussian Inc.: Wallingford CT, **2004**.

(37) Frisch, M. J. T., G. W.; Schlegel, H. B.; Scuseria, G. E.; Robb, M. A.; Cheeseman, J. R.; Scalmani, G.; Barone, V.; Mennucci, B.; Petersson, G. A.; Nakatsuji, H.; Caricato, M.; Li, X.; Hratchian, H. P.; Izmaylov, A. F.; Bloino, J.; Zheng, G.; Sonnenberg, J. L.; Hada, M.; Ehara, M.; Toyota, K.; Fukuda, R.; Hasegawa, J.; Ishida, M.; Nakajima, T.; Honda, Y.; Kitao, O.; Nakai, H.; Vreven, T.; Montgomery, Jr., J. A.; Peralta, J. E.; Ogliaro, F.; Bearpark, M.; Heyd, J. J.; Brothers, E.; Kudin, K. N.; Staroverov, V. N.; Kobayashi, R.; Normand, J.; Raghavachari, K.; Rendell, A.; Burant, J. C.; Iyengar, S. S.; Tomasi, J.; Cossi, M.; Rega, N.; Millam, N. J.; Klene, M.; Knox, J. E.; Cross, J. B.; Bakken, V.; Adamo, C.; Jaramillo, J.; Gomperts, R.; Stratmann, R. E.; Yazyev, O.; Austin, A. J.; Cammi, R.; Pomelli, C.; Ochterski, J. W.; Martin, R. L.; Morokuma, K.; Zakrzewski, V. G.; Voth, G. A.; Salvador, P.; Dannenberg, J. J.; Dapprich, S.; Daniels, A. D.; Farkas, Ö.; Foresman, J. B.; Ortiz, J. V.; Cioslowski, J.; Fox, D. J. ; B.01 ed.; Gaussian Inc., Wallingford CT, **2010**.

(38) Shao, Y.; Molnar, L. F.; Jung, Y.; Kussmann, J.; Ochsenfeld, C.; Brown, S. T.; Gilbert, A. T. B.; Slipchenko, L. V.; Levchenko, S. V.; O'Neill, D. P.; DiStasio Jr, R. A.; Lochan, R. C.; Wang, T.; Beran, G. J. O.; Besley, N. A.; Herbert, J. M.; Yeh Lin, C.; Van Voorhis, T.; Hung Chien, S.; Sodt, A.; Steele, R. P.; Rassolov, V. A.; Maslen, P. E.; Korambath, P. P.; Adamson, R. D.; Austin, B.; Baker, J.; Byrd, E. F. C.; Dachsel, H.; Doerksen, R. J.; Dreuw, A.; Dunietz, B. D.; Dutoi, A. D.; Furlani, T. R.; Gwaltney, S. R.; Heyden, A.; Hirata, S.; Hsu, C.-P.; Kedziora, G.; Khalliulin, R. Z.; Klunzinger, P.; Lee, A. M.; Lee, M. S.; Liang, W.; Lotan, I.; Nair, N.; Peters, B.; Proynov, E. I.; Pieniazek, P. A.; Min Rhee, Y.; Ritchie, J.; Rosta, E.; David Sherrill, C.; Simmonett, A. C.; Subotnik, J. E.; Lee Woodcock Iii, H.; Zhang, W.; Bell, A. T.; Chakraborty, A. K.; Chipman, D. M.; Keil, F. J.; Warshel, A.; Hehre, W. J.; Schaefer Iii, H. F.; Kong, J.; Krylov, A. I.; Gill, P. M. W.; Head-Gordon, M. *Phys. Chem. Chem. Phys.* **2006**, *8*, 3172.

(39) Valiev, M.; Bylaska, E. J.; Govind, N.; Kowalski, K.; Straatsma, T. P.; Van Dam, H. J. J.; Wang, D.; Nieplocha, J.; Apra, E.; Windus, T. L.; de Jong, W. A. *Comput. Phys. Commun.* **2010**, *181*, 1477.

(40) Aradi, B.; Hourahine, B.; Frauenheim, T. *J. Phys. Chem. A* **2007**, *111*, 5678.

CHAPTER 3

DONOR-ACCEPTOR COPOLYMERS OF RELEVANCE FOR ORGANIC PHOTOVOLTAICS: A THEORETICAL INVESTIGATION OF THE IMPACT OF CHEMICAL-STRUCTURE MODIFICATIONS ON THE ELECTRONIC AND OPTICAL PROPERTIES

3.1. Introduction

As pointed out in Chapter 1, DA copolymers have been recognized as important materials in the realm of OPV. The coupling of the donor and acceptor units is expected to lead to a material with smaller HOMO-LUMO and optical gaps than either of the constituent parts.[1-13] Upon coupling the DA moieties, the wave-function characteristics of the isolated donor and acceptor HOMOs and LUMOs and their relative energetic alignment constitute key parameters that will determine the degree of orbital mixing, conjugation length, and energetic distribution of the frontier molecular orbitals in the DA copolymers, thus controlling the intrinsic electronic and optical properties.

Achieving the small optical gaps necessary to efficiently harvest photons can be readily accomplished using DA copolymers; however, finding small-optical-gap polymers that, in combination with an ETM, can lead to efficient exciton dissociation and simultaneously maintain large V_{OC} together with large J_{SC} (to yield high PCE), remains a challenge. It is useful to note that, while the DA π-conjugated materials that have mostly been explored in OPVs are

copolymers, there is now increased interest in DA small molecules, mainly due to the potential for high purity and well-ordered systems (which can lead to larger charge-carrier mobilities).[14,15]

There has been considerable theoretical work[11,16-26] to elucidate the electronic and optical properties of DA copolymers, and in some cases to predict how a large range of materials might perform in BHJ or bilayer OPV devices.[23] Here, we have chosen to systematically investigate a series of DA systems to gather a broad understanding of the electronic and photophysical properties of these materials as a function of the DA units. In particular, we address a number of themes that are rarely fully discussed in detail. For instance, we highlight the impact of the various DA constructs on the oscillator strengths of the low-lying excited states, key parameters that define the ability of the material to efficiently absorb light. We also discuss the impact of the thiophene spacers – often stated to be included in the DA copolymer design to aid simply in the planarization of the backbone – both on the electronic structure and the optical properties, in particular the oscillator strengths.

We consider two common donor architectures where a central five-membered ring is fused on both sides by either thiophene rings (structure denoted as CPDT) or benzene rings (CPDP), see **Figure 3.1**. These donors constitute the most widely used electron-rich fragments in small optical-gap DA copolymers for bulk-heterojunction OPV. The donor architectures were further varied through substitution of the carbon at the 9-position by either nitrogen or silicon atoms (denoted X in **Figure 3.1**) to explore the impact of such substitution on the geometric and electronic properties (as was done in many instances[17,27-34]). Twelve commonly used acceptors were chosen to study a variety of monomer constructs. The electron-poor units are coupled to the donor in one of two configurations, either directly or via bis-thiophene linkages (denoted Y and T-Y-T in **Figure 3.1**); the latter are often employed to increase the planarity of the conjugated

backbone. In total, this leads to the investigation of 144 different DA monomer configurations. In addition, we have evaluated the energies of the frontier molecular levels for a representative electron-transport material, methanofullerene[6,6]-phenyl-C_{61}-butyric acid methyl ester ($PC_{61}BM$), to compare to those of the copolymers.

While OPV performance is largely dependent on the materials properties within the bulk heterojunction that are influenced by molecular/polymer packing, morphology, and disorder/defects, a necessary requirement for good device performance is for the materials to present suitable intrinsic properties. Therefore, our goal here is to gain an in-depth understanding of the intrinsic structural, electronic, and optical properties of the DA copolymers. To do so, we will first discuss the properties of the isolated donors and acceptors and then turn to the coupled DA systems.

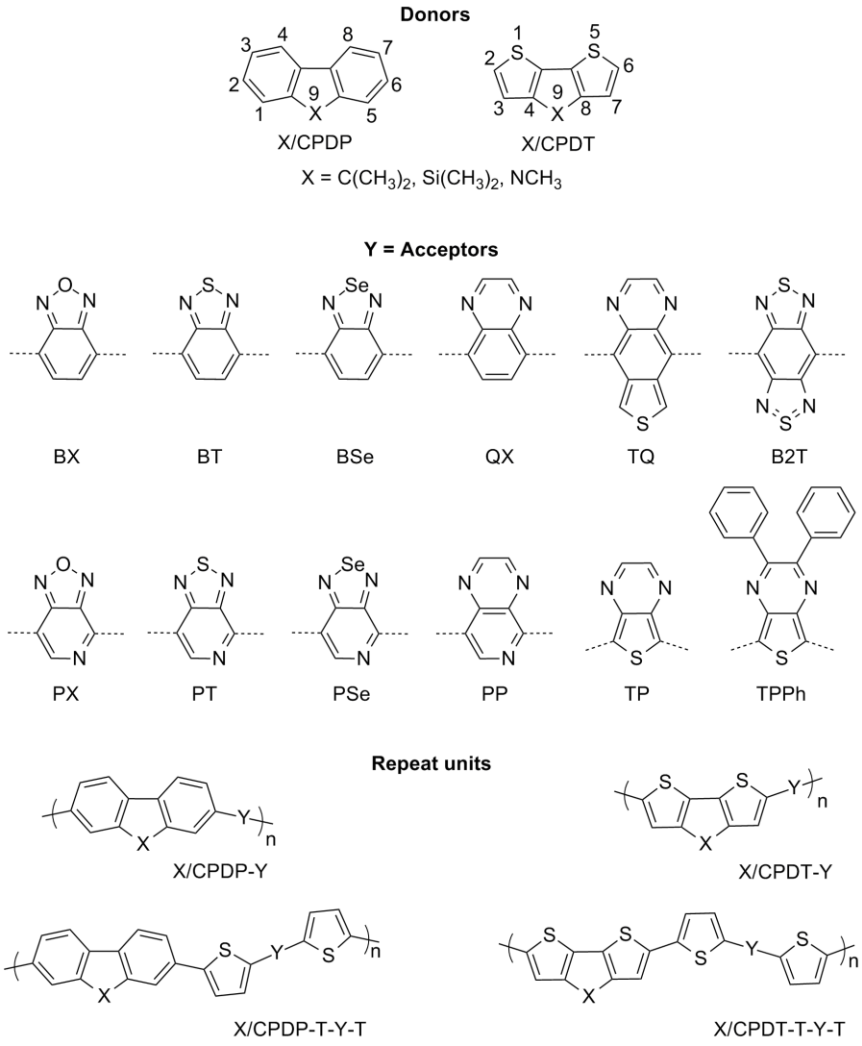

Figure 3.1 Schematic illustration of an OPV device: the photoactive layer is sandwiched between the hole- and electron-collecting electrodes (HCE and ECE, respectively). Chemical structures of the donors (X/CPDP, X/CPDT, atom numbers listed for clarity), acceptors (isolated (Y), and bis-thiophene substituted (T-Y-T)), and copolymer repeat units considered in this work. The acceptor abbreviations stand for: BX ≡ benzo[*c*][1,2,5]oxadiazole; BT ≡ benzo[*c*][1,2,5]thiadiazole; BSe ≡ benzo[*c*][1,2,5]selenadiazole; QX ≡ Quinoxaline; B2T ≡ Benzo[1,2-*c*:4,5-*c'*]bis[1,2,5]thiadiazole; TQ ≡ thieno[3,4-*g*]quinoxaline; PX ≡ [1,2,5]oxadiazolo[3,4-*c*]pyridine; PT ≡ [1,2,5]thiadiazolo[3,4-*c*]pyridine; PSe ≡ [1,2,5]selenadiazolo[3,4-*c*]pyridine; PP ≡ pyrido[3,4-*b*]pyridine; TP ≡ thieno[3,4-*b*]pyrazine; TPPh ≡ diphenylthieno[3,4-*b*]pyrazine.

3.2. Computational methodology

The isolated donors and acceptors and DA oligomeric structures (with n = 1 to 4 repeat units) were evaluated at the DFT level with the global hybrid B3LYP functional[35-38] in conjunction with a 6-31G(d,p) basis set.[39,40] The low-lying singlet excited states of the DA oligomers were evaluated at the neutral ground-state geometries using TDDFT with B3LYP and the same basis. We note that the solubilizing chains often appended along the conjugated backbone are represented here as methyl groups to reduce the computational cost while still accounting for the electron-donating ability of the substituent.[41] All calculations were performed using the Gaussian03 (Revision E.01) suite of programs.[42]

It is important to keep in mind that the use of the B3LYP functional can have limitations with regard to the proper description of charge-transfer excited states. In this context, recent work with *tuned* long-range corrected (LRC) functionals (including our work described in the following Chapter) has highlighted significant improvements in terms of these descriptions.[43-48] However, since we are interested here in the trends among analogous systems and given the substantial cost associated with the tuning of the range-separation parameter for every oligomer unit considered, B3LYP remains a reasonable choice for our purpose while providing a consistent framework for the comparison of the results.

3.3. Results and discussion

For the sake of conciseness, we will restrict the oligomer data discussed below to the tetramer (n = 4) cases. Details of the calculated electronic and optical properties for the structures we studied can be found in the Ancillary Material.

3.3.1. Electronic structure of the isolated donor and acceptor fragments

Based on the $C(CH_3)_2$, NCH_3, or $Si(CH_3)_2$ X-substituent, the CPDP and CPDT donor fragments are referred to as C/CPDP, N/CPDP, or Si/CPDP and C/CPDT, N/CPDT, or Si/CPDT, respectively. The HOMO energies of these donor fragments are calculated to range between -5.1 eV to -5.8 eV (see **Table A.3.1**); the HOMO energies of the X/CPDP donor fragments are more energetically stable (by ≈ 0.2–0.6 eV) than those of the X/CPDT fragments, which reflects the larger aromaticity of the benzene rings vs. thiophene rings. However, replacing $Si(CH_3)_2$ with NCH_3 in the 9-position destabilizes the HOMO energy by 0.46 eV and 0.20 eV in the X/CPDP and X/CPDT fragments, respectively; this is due to the interplay between the resonant electron-donating effect and inductive electron-withdrawing effect of the nitrogen. As expected, the variations in electronic structure between the $C(CH_3)_2$ and $Si(CH_3)_2$ systems are very small.

Turning to the LUMO energies of the acceptor fragments (Y), **Figure 3.2** illustrates that they vary considerably with an energetic separation of some 1.6 eV between the LUMOs of the weakest acceptor, quinoxaline[49] (QX), and the strongest acceptor, benzodithiadizole[50] (B2T). The pyridine derivatives (PSe,[51] PT,[52] PX,[53] and PP[54]) present, as expected, more stable LUMO energies (larger, *i.e.*, more exothermic, electron affinities) than their respective benzene counterparts (BSe,[92] BT,[92] BX,[55] and QX[56]) as a result of the inductive electron-withdrawing effect of the pyridine nitrogen.[17] Similarly, the larger inductive electron-withdrawing effect from oxygen compared to sulfur (or selenium) results in a more stable LUMO for BX and PX compared to BT and PT (or BSe and PSe). Note that BSe and PSe have slightly more stable LUMO energies compared to BT and PT (-2.44 eV and -2.91 eV vs. -2.35 and -2.83 eV, respectively), which is consistent with previously reported results[57,58] (also matching the trend reported for their DA oligomer analogs[59]). With similar electronegativities, this highlights the

contribution of the resonant effect (weaker N-Se coupling compared to N-S due to the longer bond length) on the LUMO energy stabilization. Extension of the conjugation due to the fusion of an additional thiophene ring in TQ compared to QX stabilizes the LUMO energy by 0.58 eV. The addition of two phenyl substituents in TPPh compared to TP results in minimal effects on the LUMO energy because of the limited conjugation of the phenyl groups to the TP core (the phenyl groups are twisted by some 42° out of the plane of TP).

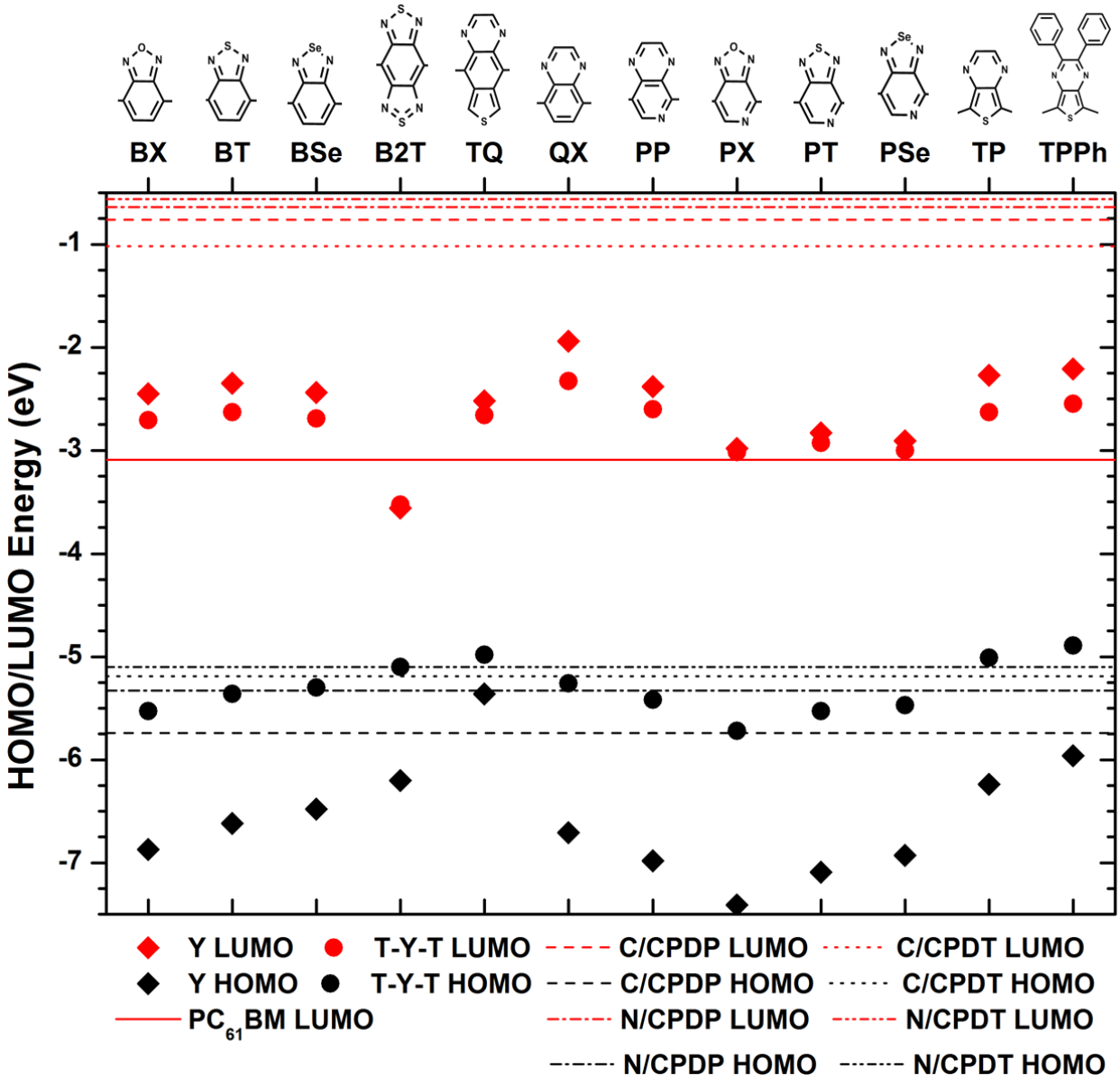

Figure 3.2 HOMO and LUMO energies of the isolated C/CPDP, C/CPDT, N/CPDP, and N/CPDT donors and unsubstituted (Y) and bis-thiophene substituted (T-Y-T) acceptors, as determined at the B3LYP/6-31G(d,p) level of theory. The LUMO energy of $PC_{61}BM$ is included for reference.

In many of the DA copolymers designed for BHJ solar cells, the isolated acceptors (Y) are coupled on both sides by thiophene units to form T-Y-T segments.[60-62] The increased conjugation brought by the thiophene rings is generally expected to contribute to a higher HOMO energy (smaller ionization potential) through enhanced delocalization of the DA HOMO wave function. Also, in some systems, these substitutions can have important implications on increasing/maintaining coplanarity along the conjugated backbone, see below.[11] The HOMO wave functions of the T-Y-T structures (see SI) are largely delocalized over both the acceptor and thiophene moieties, whereas the LUMO wave functions are mainly localized along their acceptor fragments. These characteristics are a simple consequence of a closer energetic alignment of the HOMO energies of the isolated acceptor fragments and thiophene ($\Delta E(HOMO) \approx 0.1 - 1.0$ eV), while there is a much larger difference in their respective LUMO energies ($\Delta E(LUMO) \approx 1.7 - 3.3$ eV). Another consequence is that the bis-thiophene substituted acceptors display only slightly more energetically stabilized LUMOs, at most by ~ 0.4 eV, compared to their isolated counterparts, see **Figure 3.2** and **Table A.3.2**. The extent of stabilization depends on the acceptor strength, where the strongest acceptors (presenting the largest LUMO energy difference between themselves and thiophene) show minimal impact of the addition of the thiophene rings while the weaker acceptors have the largest LUMO energy stabilization. Compared to the isolated acceptors, the destabilization of the HOMO energies for the bis-thiophene-substituted acceptors is substantial (by ≈ 0.4–1.7 eV). Thus, the HOMO destabilization in the bis-thiophene-substituted acceptors has a much larger contribution to the

lowering of the fundamental gap compared to the contribution from the LUMO stabilization.[18] Inspection of **Figure 3.2** provides a very important message. The HOMO energies of the donor and T-Y-T fragments being very similar, a strong mixing of the HOMO wave functions of the two components is possible. This will be much less the case when considering the LUMOs.[63]

3.3.2. DA oligomer geometric and electronic structures

The labeling used for the DA oligomers is given in **Figure 3.1**. The ground-state geometric structures of the DA oligomers are very much influenced by the choice of the donor and acceptor fragments. The structures present varying degrees of linearity (or lack thereof) along the long molecular axis and of deviations from coplanarity. **Figure 3.3** provides the labeling of the torsion angles while **Table 3.1** gathers the torsion angles along the conjugated backbones of select DA oligomers.

In general, the X/CPDP-Y oligomers deviate more from a coplanar architecture compared to X/CPDT-Y oligomers; this is a consequence of the steric interactions between the hydrogen atoms in the 1-, 3-, 5-, and 7-positions of X/CPDP (vs. the 3- and 7-positions of X/CPDT) and the nearest-neighbor atoms of the acceptor fragment. The torsion angles are the largest for oligomers with the TQ, QX, and PP acceptors due to the increased bulkiness of these acceptor heterocycles. The additional increase in torsion angle in systems with the TQ acceptor is a result of the increased bulkiness from the extension of the heterocycle and the steric hindrance from the two hydrogen atoms in the 6- and 8-positions. Large deviations from planarity impact the electronic structure of the oligomers through reduction of the wave-function delocalization.

Introduction of the thiophene rings between the donors and acceptors, in general, reduces these torsion angles.[11] These smaller twists are a result of limiting the steric interactions, especially with the neighboring six-membered rings in the X/CPDP-Y fragment; coupling the

bis-thiophene-substituted acceptors to the X/CPDT-based donors has a lesser impact on the degree of twisting. We note that there can be a substantial energy cost, varying from 2.3 to 63.4 kcal/mol (or, in the context of thermal energy, from some 1200 K to 30,000 K), required to coplanarize the DA oligomers that present torsion angles $\geq$ 25°.

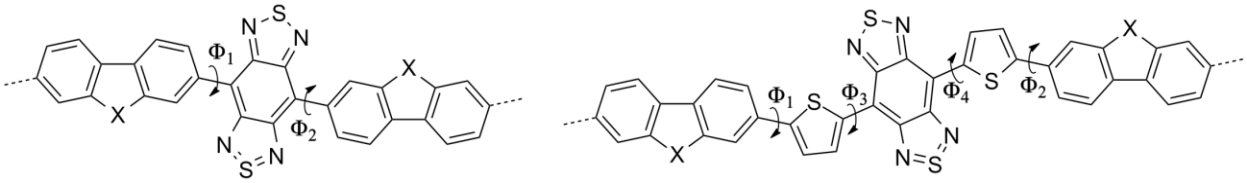

Figure 3.3 Illustration of the torsion angles along the conjugated backbones of the DA oligomers.

Table 3.1 Illustration of the torsion angles along the conjugated backbones of the DA oligomers. Torsion angles (°) along the conjugated backbone and the total energy difference (kcal/mol) between a constrained coplanar conformation (to keep Φ = 0°, fully relaxed otherwise) and the fully relaxed geometries for select oligomers as determined at the B3LYP/6-31G(d,p) level of theory. See **Figure 3.3** for definitions of the torsion angles.

	Φ_1	Φ_2	Φ_3	Φ_4	ΔE_{tot} [b]
N/CPDP-BT	39	35	-	-	13.0
N/CPDP-B2T	37	37	-	-	
N/CPDP-TQ	54	55	-	-	63.4[a]
N/CPDP-QX	47	44	-	-	26.9
N/CPDP-PP	43	25	-	-	13.8
N/CPDP-PT	35	3	-	-	
N/CPDP-TP	22	13	-	-	0.9
N/CPDP-T-BT-T	27	26	9	5	2.9
N/CPDP-T-B2T-T	23	23	1	1	
N/CPDP-T-TQ-T	25	27	42	41	25.4[a]
N/CPDP-T-QX-T	28	26	6	21	3.5
N/CPDP-T-PP-T	27	26	0	18	3.1
N/CPDP-T-PT-T	26	26	0	5	
N/CPDP-T-TP-T	25	25	0	1	2.3
N/CPDT-BT	1	3	-	-	
N/CPDT-B2T	0	0	-	-	
N/CPDT-TQ	27	35	-	-	14.9[a]
N/CPDT-QX	11	5	-	-	0.1
N/CPDT-PP	0	7	-	-	
N/CPDT-PT	0	0	-	-	
N/CPDT-TP	0	0	-	-	
N/CPDT-T-BT-T	7	7	1	1	
N/CPDT-T-B2T-T	0	0	0	0	
N/CPDT-T-TQ-T	20	11	40	40	20.5[a]
N/CPDT-T-QX-T	13	11	17	2	0.4
N/CPDT-T-PP-T	3	10	1	12	
N/CPDT-T-PT-T	2	6	0	1	
N/CPDT-T-TP-T	1	3	1	1	

[a] We note that in constraining Φ to 0 degrees, the relaxed TQ heterocycle is no longer coplanar due to increased steric interactions. Torsion angles for C/CPDP-(TP, QX, BT, TQ, and B2T) have been reported previously.[25] [b] ΔE_{tot} are included for representative examples.

As anticipated from our earlier discussions, the HOMO wave function in the DA oligomers is generally delocalized over both donor and acceptor fragments. In most cases, these

wave functions correspond to the out-of-phase combination of the HOMOs of the donor and acceptor fragments, see **Figure 3.4** and **Figure 3.5**. The LUMO wave functions of most systems, on the other hand, are predominantly composed of the acceptor LUMO and are localized over the acceptor fragments. Obviously, the level of mixing and localization/delocalization of the HOMO and LUMO wave functions in the DA oligomers is also a function of the torsion angles along the donor and acceptor conjugation bridge. Inspection of **Figure 3.2**, **Figure 3.4**, and **Figure 3.5** highlights the roles of energetic alignment and (departure from) coplanarity. For C/CPDP-QX, the LUMO wave function is localized over the acceptor fragment due to the combination of a large mismatch between the LUMO energies and large torsion angles. With slightly better matching of the LUMO energies and substantial decrease in torsion angles (we note that the C/ and N/ torsion angles are comparable), the LUMO in C/CPDT-QX is delocalized over both the donor and acceptor components.

Interestingly, see **Figure 3.5**, the strongly stabilized LUMO of the B2T acceptor energetically matches better with the C/CPDT HOMO than the C/CPDT LUMO; as a result, the C/CPDT-B2T LUMO also displays some contribution from the HOMO of C/CPDT (see **Figures A.3.1** and **A.3.2**). In addition, the C/CPDT-B2T HOMO is composed of the C/CPDT HOMO and has contributions from both the HOMO and LUMO wave functions of B2T. This strongly impacts the fundamental gap of X/CPDP-B2T, *vide infra*.

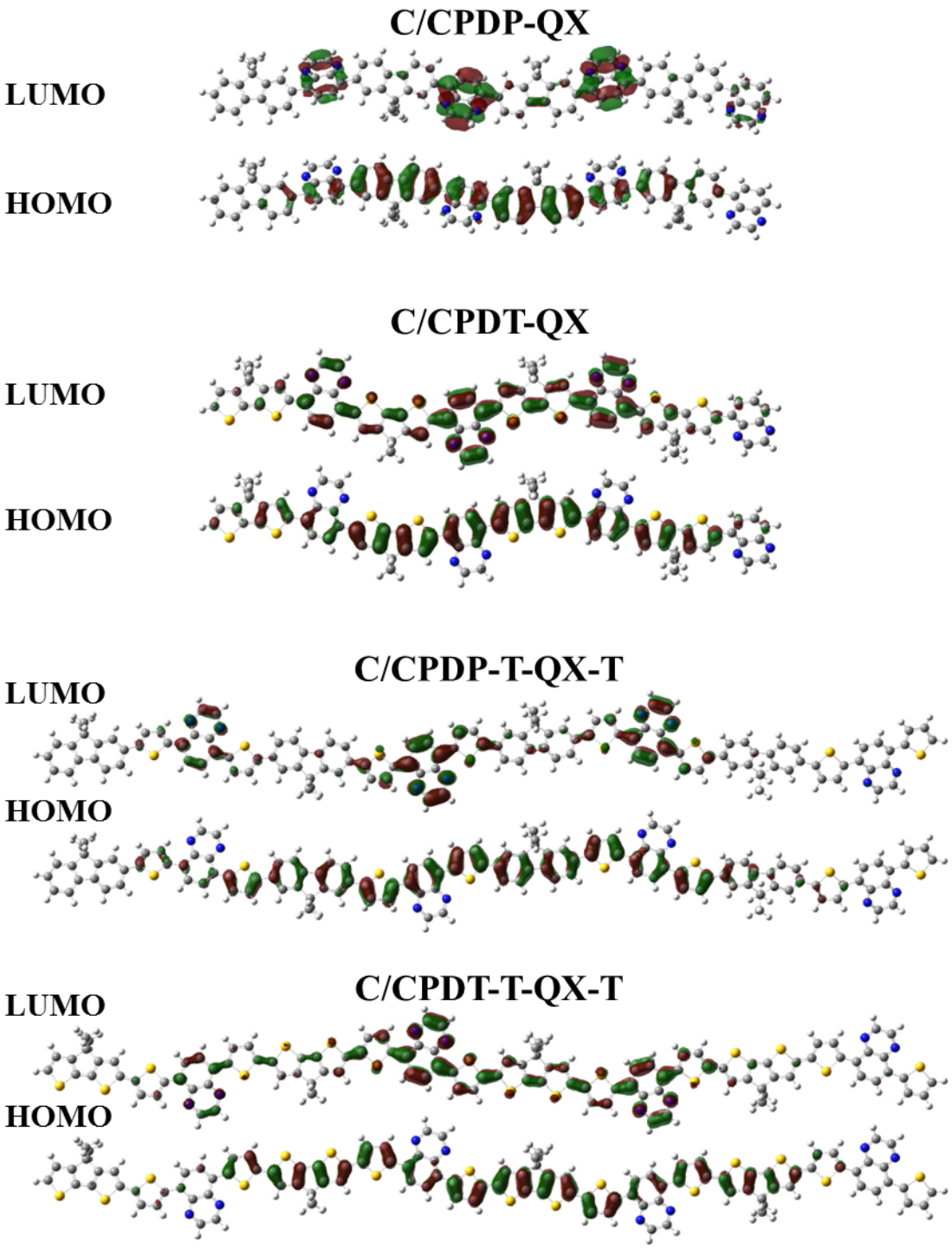

Figure 3.4 Illustrations of the frontier molecular orbitals (isovalue surface 0.02 a.u.) for the C/CPDP-QX, C/CPDT-QX, C/CPDP-T-QX-T, and C/CPDT-T-QX-T tetramers evaluated at the B3LYP/6-31G(d,p) level.

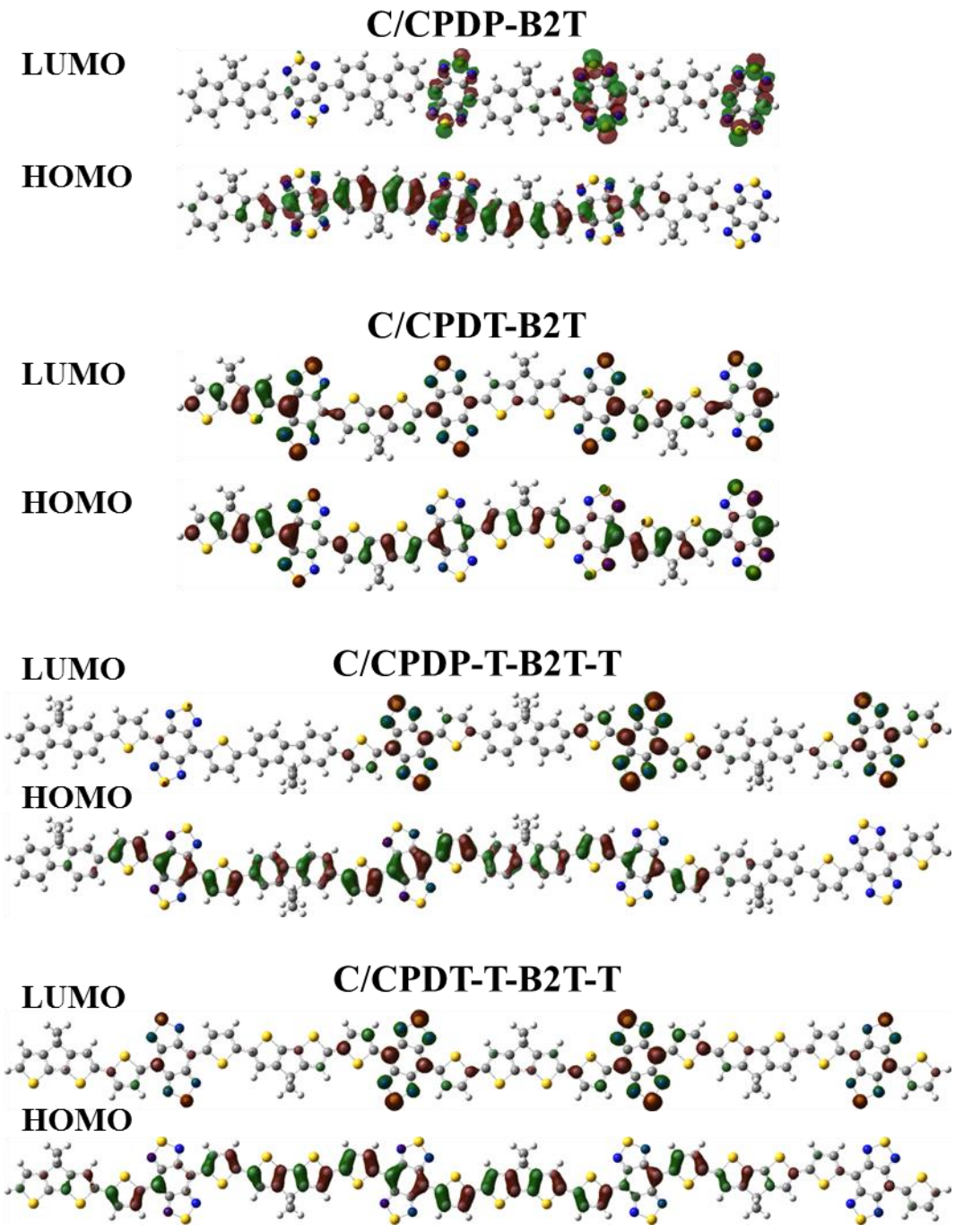

Figure 3.5 Illustrations of the frontier molecular orbitals (isovalue surface 0.02 a.u.) for the C/CPDP-B2T, C/CPDT-B2T, C/CPDP-T-B2T-T, and C/CPDT-T-B2T-T tetramers evaluated at the B3LYP/6-31G(d,p) level.

Figure 3.6 illustrates the HOMO and LUMO energies and fundamental gaps for the DA tetramers as a function of the acceptor fragments. The X/CPDP-Y oligomers have energetically-stabilized HOMOs compared to the X/CPDT-Y oligomers, which is consistent with the trends for the isolated donor fragments. The X/CPDP-T-Y-T HOMO energies are significantly destabilized (by 0.11–0.43 eV) when compared to X/CPDP-Y oligomers, as a result of a more coplanar configuration across the backbone and increased delocalization of the HOMO wave function (it should be borne in mind that the extents of localization/delocalization we are referring to here, are simple qualitative descriptions from inspection of the MOs). The effect of the various X-substituents on the DA tetramer HOMO energy is smaller (0.04 eV – 0.16 eV) than in the isolated donors. Although small, we recall that such differences can play a significant role on the open-circuit voltage of the solar cell.[31,64] The fundamental gap of the DA tetramers is a function of the HOMO and LUMO energy trends as discussed above, with X/CPDP-based tetramers presenting a larger fundamental gap compared to X/CPDT-based tetramers. The X/CPDP-T-Y-T tetramers have substantially reduced fundamental gap compared to the X/CPDP-Y tetramers while the effect is much smaller in the X/CPDT-based tetramers.

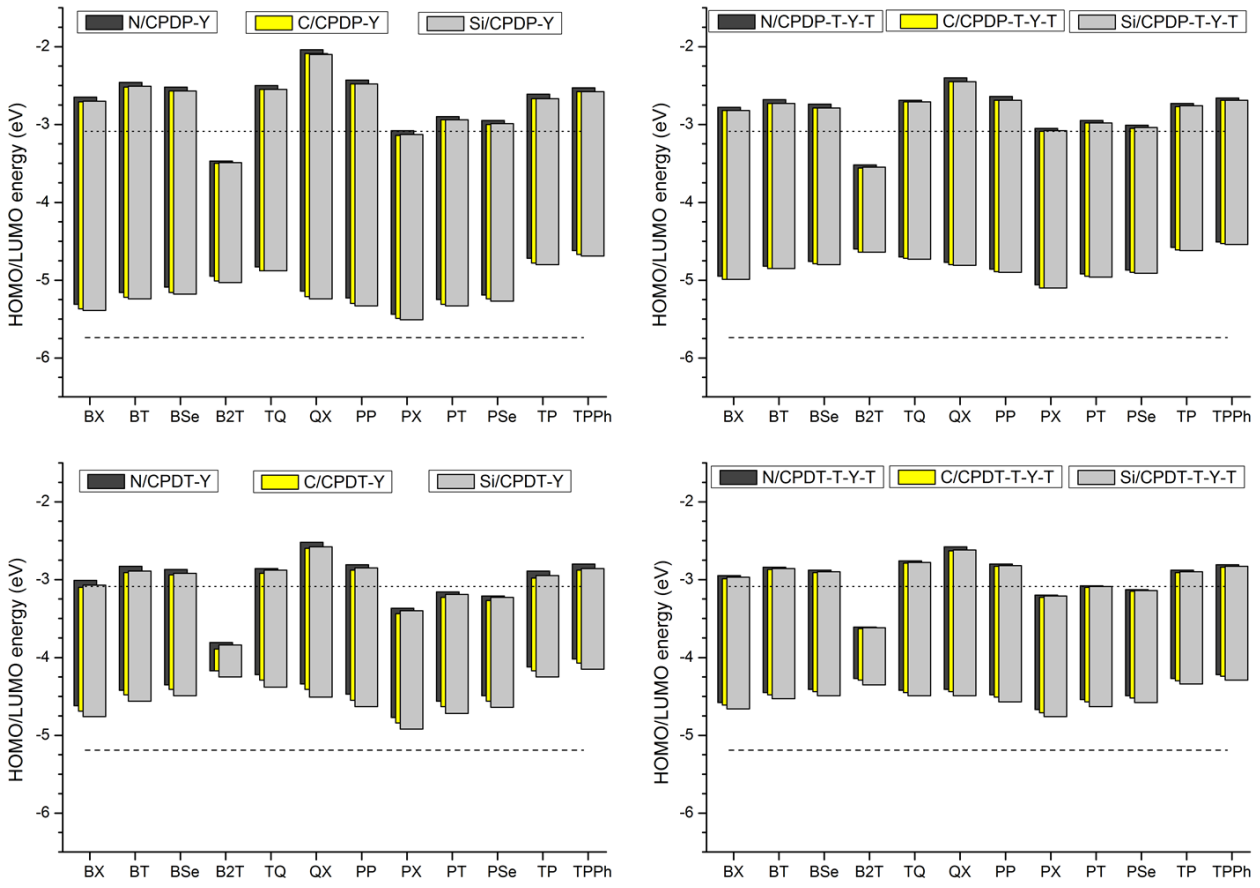

Figure 3.6 Energies of HOMO (bottom of rectangular box) and LUMO (top of rectangular box) and fundamental gaps of the tetramers as determined at the B3LYP/6-31G(d,p) level. The HOMO energy of the isolated C/CPDP or C/CDPT fragments (dashed lines) and the PC61BM LUMO energy (dotted lines) are included for reference.

Figure 3.6 also illustrates the relationship between the LUMO energies of the DA tetramers and $PC_{61}BM$. Note that a number of tetramers are calculated to have energetically stabilized LUMOs compared to that of $PC_{61}BM$, most notably all of the tetramers containing the B2T and PX acceptors; this can negatively impact the ability of the corresponding copolymers to transfer electrons to the fullerene electron-transport material.

3.3.3. DA oligomer lowest excitation energies and absorption strengths

Time-dependent density functional theory at the B3LYP/6-31G(d,p) level has been used to gain insight into the vertical singlet ($S_0 \rightarrow S_n$) electronic transitions. The evolution of the first vertical transition energy ($S_0 \rightarrow S_1$, E_{OP}) and the $S_0 \rightarrow S_1$ transition configurations are described in detail in the Supporting Information. The $S_0 \rightarrow S_1$ transitions can be principally described as HOMO→LUMO one-electron excitations; as a result, the magnitude and trends in optical gaps are similar to those of the fundamental gaps.

The ability to effectively absorb photons is an important parameter that governs the efficiency of OPVs. The oscillator strength of an electronic excitation is directly determined by the square of the transition dipole moment between the ground and excited state, which is namely a function of the spatial overlap between the ground-state and excited-state wave functions. **Figure 3.7** shows the evolution of the oscillator strength (*f*) for vertical transitions from the ground state to the lowest-lying excited state ($S_0 \rightarrow S_1$) for the DA tetramers. The oscillator strengths in X/CPDT-based oligomers, in general, are larger than those for the X/CPDP tetramers, which relates to the more coplanar nature of the geometric structure. DA oligomers with bisthiophene-substituted acceptors have considerably larger oscillator strengths; this increase comes from the contributions of: (i) extended conjugated paths that contribute to larger transition moments; and (ii) increased coplanarity (especially for the X/CPDP-based oligomers) that improves the spatial overlap of the wave functions.

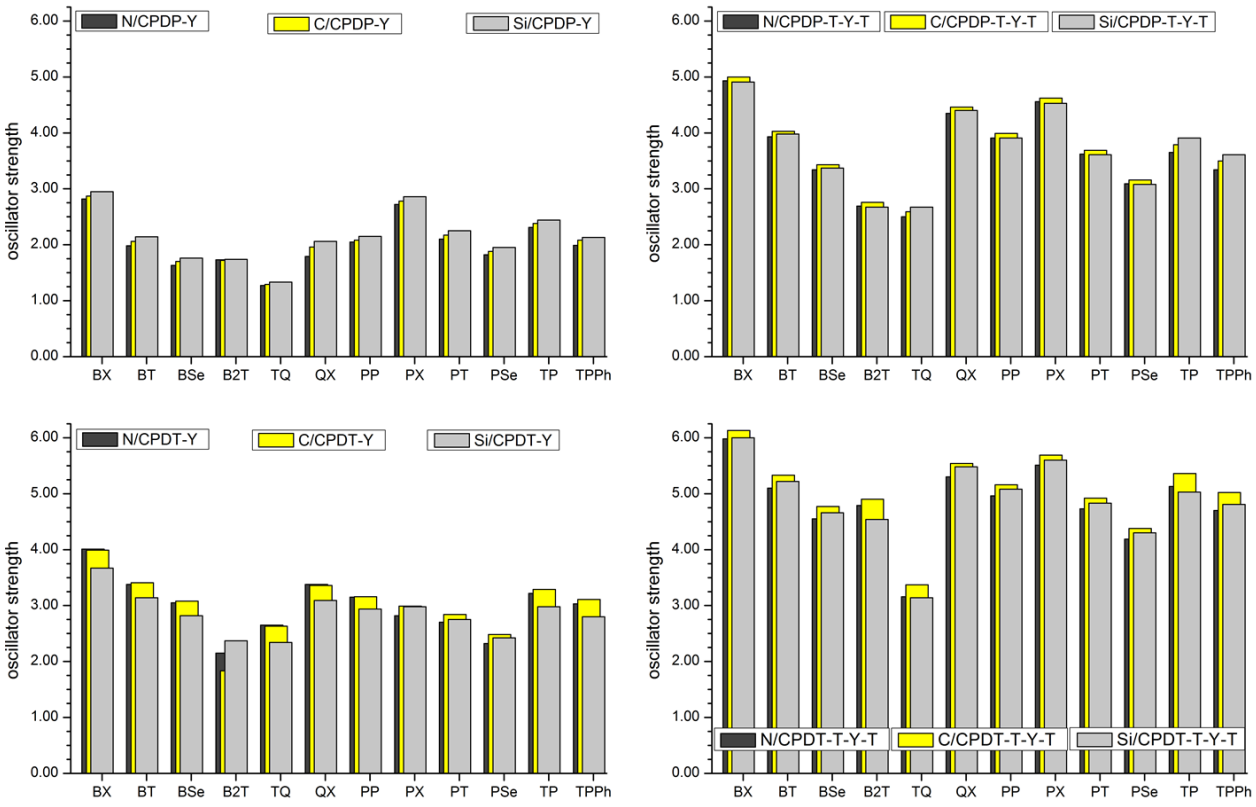

Figure 3.7 Energies of HOMO (bottom of rectangular box) and LUMO (top of rectangular box) and fundamental gaps of the tetramers as determined at the B3LYP/6-31G(d,p) level. The HOMO energy of the isolated C/CPDP or C/CDPT fragments (dashed lines) and the PC61BM LUMO energy (dotted lines) are included for reference. Oscillator strength (f) for the first vertical transition (S0→ S1) for the DA tetramers as determined at the TD-B3LYP/6-31G(d,p) level.

There is effectively no change in the calculated oscillator strengths as a function of the X-substituent in the X/CPDP-based oligomers. In X/CPDT-based oligomers, there occurs some increase in oscillator strength (up to 8 and 12% for the X/CPDT-Y and X/CPDT-T-Y-T oligomers, respectively) when X changes from $Si(CH_3)_2$ to $C(CH_3)_2$. This is possibly a contribution from a decrease in the backbone curvature (see **Figure A.3.5**), or reduced distortion of the cyclopentadithiophene unit (due to the smaller atomic size of carbon vs. silicon) as described by Scharber *et al.*[65].

Available experimental data are compared to the calculated data in **Table 3.2**. A direct comparison is in fact difficult as there are many parameters that differ from one set of measurements to another. For instance, data from electrochemical techniques differ as there is no consistent use of standard electrodes or solvents. For the optical gap, the difficulty in comparison comes from the measurements taking place either in solution (with varying solvents) or in thin films. Additionally, the optical gaps are sometimes reported from the absorption onset and at other times from the absorption maximum. Keeping these limitations in mind as well as the limits of the quantum-mechanical methods used in the calculations (*e.g.* the density functional approximations used and oligomer calculations *in vacuo* at 0 K *vs.* polymer property measurements in solution or the solid state), there is generally a good agreement between the calculated data and the available experimental results. The ionization potentials and electron affinities are generally underestimated with the IP somewhat more so than the EA, whereas the calculated values for the optical gaps, E_{OP}, values match well with the experimental values.

Table 3.2 Calculated (Koopmans) gas phase IP, EA, EG, and EOP values compared to available experimental data.

Oligomer	Experimental (eV)					Calculated (eV)			
	IP	EA	E_G (IP-EA)	E_{OP}	Ref.	-HOMO energy	-LUMO energy	E_G	E_{OP}
N/CPCP-T-BX-T	5.47	3.65	1.82	1.87$^{\sigma}$	[a]	4.95	2.78	2.18	1.87
N/CPCP-T-BT-T	5.45	3.60	1.85	1.88$^{\sigma}$	[a]	4.82	2.68	2.13	1.82
N/CPCP-T-QX-T	5.46	3.42	2.04	2.02$^{\sigma}$	[a]	4.77	2.40	2.37	2.02
N/CPCP-T-PP-T	5.52	3.67	1.85	1.89$^{\sigma}$	[a]	4.86	2.64	2.21	1.88
N/CPCP-T-PX-T	5.55	3.93	1.62	1.67$^{\sigma}$	[a]	5.06	3.05	2.02	1.74
N/CPCP-T-PT-T	5.53	3.80	1.73	1.75$^{\sigma}$	[a]	4.92	2.95	1.97	1.68
C/CPDP-T-BT-T				2.28$^{\tau}$	[b]	4.85	2.73	2.12	1.80
C/CPDP-T-TPPh-T	5.60	3.60	2.00	1.55$^{\sigma}$	[c]	4.53	2.69	1.84	1.56
Si/CPDP-T-BT-T	5.39			1.82$^{\sigma}$	[d]	4.85	2.73	2.13	1.81
N/CPDT-BT	4.81	3.08	1.73	1.43$^{\sigma}$	[e]	4.48	2.91	1.57	1.34
C/CPDT-BT	5.30	3.57	1.73	1.40$^{\sigma}$	[f]	4.48	2.91	1.57	1.34
C/CPDT-BSe	4.90	3.28	1.62	1.35$^{\sigma}$	[g]	4.41	2.94	1.47	1.23
Si/CPDT-BT	5.05	3.27	1.78	1.45$^{\sigma}$	[h]	4.56	2.89	1.67	1.41
N/CPDT-T-BT-T	5.00	3.43	1.57	1.46$^{\sigma}$	[i]	4.45	2.88	1.53	1.25
N/CPDT-T-B2T-T	5.05	4.30	0.83	0.54$^{\sigma}$	[j]	4.47	3.61	0.66	0.59

It should be noted that various -R groups are attached in the experimentally reported polymer architectures. Also, the electrochemistry techniques are very broad (variety of standard electrodes, solvents used). The optical gaps are estimated either from the absorption maximum or absorption onset in solution (variety of solvents) or in thin films. $^{\sigma}$ Absorption onset. $^{\tau}$ Absorption maxima. References: [a] Blouin *et al.*,[17] [b] Svensson *et al.*,[28] [c] Perzon *et al.*,[66] Zhang *et al.*,[43] [d] Wang *et al.*,[31] [e] Yue *et al.*,[67] [f] Muhlbacher *et al.*,[68] [g] Hou *et al.*,[69] [h] Hou et al.,[33] [i] Zhou et al,[62] [j] Steckler *et al*.[70]

3.4. Conclusions

The literature on donor-acceptor copolymers (or small molecules) includes constructs that, on the one hand, consist of purely donor and acceptor moieties and, on the other hand, also include thiophene spacers along the conjugated backbone.[60-62] Our main goal in this Chapter was to investigate the extent of the electronic couplings between the donor and acceptor units as well as the role of the thiophene spacers and to determine the donor-acceptor copolymer geometric, electronic, and optical properties. To derive a broad understanding, we considered a large series of copolymers based on six representative donors and twelve acceptors, in the absence and in the presence of the thiophene spacers.

Individually, the acceptors considered herein present a large variation in LUMO energies (electron affinities). On bis-thiophene substitution (thiophenes sandwiching the acceptor), the LUMO energies are somewhat stabilized (up to 0.4 eV) with the weaker acceptors presenting the largest stabilization. Compared to the isolated units, the HOMO energies of the bis-thiophene-substituted acceptors are significantly destabilized (0.4 – 1.7 eV), a consequence of large wave-function delocalization resulting from the close alignment of the isolated acceptor and thiophene HOMO energies. This destabilization in fact brings the bis-thiophene-substituted acceptor HOMO energies close to the HOMO energies of the donors, allowing in principle for a strong mixing of the respective HOMO wavefunctions across the DA oligomers.

The level of mixing of the HOMO or LUMO wavefunctions, and their subsequent localization/delocalization, however, is a function not only of the energetic alignment of the respective molecular orbitals but also of the torsion angles between the units. We find that the thiophene spacers help planarize the copolymer backbone, for instance, by 10 – 25 ° in the X/CPDP-T-Y-T compared to the X/CPDP-Y oligomers. Overall, the HOMO energy for the X/CPDP-T-Y-T oligomers is 0.1 – 0.4 eV higher than for the X/CPDP-Y oligomers; there is also a 55 – 120 % increase in oscillator strength for the X/CPDP-T-Y-T oligomers compared to X/CPDP-Y.

The benzobisthiadiazole (B2T) acceptor presents characteristics that differ from the other systems. Due to its very strong acceptor character, its strongly stabilized LUMO energetically matches better with the HOMO of C/CPDT than the LUMO; as a result, the C/CPDT-B2T LUMO displays some contribution from C/CPDT HOMO in addition to B2T LUMO. This provides an unusual example of the role of energetic alignment in the mixing of donor and acceptor wavefunctions in donor-acceptor copolymers.

In this Chapter, we have thus been able to quantify the extent to which the thiophene spacers destabilize the acceptor HOMO energies, stabilize their LUMO energies, planarize the donor-acceptor copolymer backbone, and as a result impact the overall electronic and optical properties. The quantitative and qualitative descriptions of the excited states that determine the donor-acceptor copolymer optical properties are discussed in more detail in the next Chapter. It must be emphasized, however, that both i) intramolecular sterics that can arise from the use of solubilizing groups and ii) intermolecular interactions of the hole- and electron-transport materials in the active layer can further impact these properties. Our first steps in investigating the HTM:ETM interactions are discussed in Chapters 5 and 6.

3.5. References

(1) Havinga, E. E.; ten Hoeve, W.; Wynberg, H. *Polym. Bull.* **1992**, *29*, 119.

(2) van Mullekom, H. A. M.; Vekemans, J.; Havinga, E. E.; Meijer, E. W. *Mater. Sci. Eng. R.* **2001**, *32*, 1.

(3) Günes, S.; Neugebauer, H.; Sariciftci, N. S. *Chem. Rev.* **2007**, *107*, 1324.

(4) Thompson, B. C.; Fréchet, J. M. J. *Angew. Chem. Int. Ed.* **2008**, *47*, 58.

(5) Li, Y.; Zou, Y. *Adv. Mater.* **2008**, *20*, 2952.

(6) Cheng, Y. J.; Yang, S. H.; Hsu, C. S. *Chem. Rev.* **2009**, *109*, 5868.

(7) Li, C.; Liu, M.; Pschirer, N. G.; Baumgarten, M.; Müllen, K. *Chem. Rev.* **2010**, *110*, 6817.

(8) Liang, Y.; Yu, L. *Acc. Chem. Res.* **2010**, *43*, 1227.

(9) Roncali, J. *Acc. Chem. Res.* **2009**, *42*, 1719.

(10) Facchetti, A. *Chem. Mater.* **2010**, *23*, 733.

(11) Boudreault, P.-L. T.; Najari, A.; Leclerc, M. *Chem. Mater.* **2010**, *23*, 456.

(12) Brocks, G.; Tol, A. *J. Phys. Chem.* **1996**, *100*, 1838.

(13) Roncali, J. *Chem. Rev.* **1997**, *97*, 173.

(14) Walker, B.; Tamayo, A. B.; Dang, X.-D.; Zalar, P.; Seo, J. H.; Garcia, A.; Tantiwiwat, M.; Nguyen, T.-Q. *Adv. Funct. Mater.* **2009**, *19*, 3063.

(15) Sun, Y.; Welch, G. C.; Leong, W. L.; Takacs, C. J.; Bazan, G. C.; Heeger, A. J. *Nat. Mater.* **2012**, *11*, 44.

(16) Yang, L.; Feng, J.-K.; Ren, A.-M.; Sun, J.-Z. *Polymer* **2006**, *47*, 1397.

(17) Blouin, N.; Michaud, A.; Gendron, D.; Wakim, S.; Blair, E.; Neagu-Plesu, R.; Belletete, M.; Durocher, G.; Tao, Y.; Leclerc, M. *J. Am. Chem. Soc.* **2008**, *130*, 732.

(18) Karsten, B. P.; Viani, L.; Gierschner, J.; Cornil, J.; Janssen, R. A. J. *J. Phys. Chem. A* **2008**, *112*, 10764.

(19) Karsten, B. P.; Bijleveld, J. C.; Viani, L.; Cornil, J.; Gierschner, J.; Janssen, R. A. J. *J. Mater. Chem.* **2009**, *19*, 5343.

(20) Pappenfus, T. M.; Schmidt, J. A.; Koehn, R. E.; Alia, J. D. *Macromolecules* **2011**, *44*, 2354.

(21) Beaupré, S.; Belletête, M.; Durocher, G.; Leclerc, M. *Macromol. Theory Simul.* **2011**, *20*, 13.

(22) Chen, H.-Y.; Hou, J.; Hayden, A. E.; Yang, H.; Houk, K. N.; Yang, Y. *Adv. Mater.* **2010**, *22*, 371.

(23) O'Boyle, N. M.; Campbell, C. M.; Hutchison, G. R. *J. Phys. Chem. C* **2011**, *115*, 16200.

(24) Risko, C.; McGehee, M. D.; Bredas, J.-L. *Chem. Sci.* **2011**, *2*, 1200.

(25) Wu, W.-C.; Chen, W.-C. *J. Polym. Res.* **2006**, *13*, 441.

(26) Banerji, N.; Gagnon, E.; Morgantini, P.-Y.; Valouch, S.; Mohebbi, A. R.; Seo, J.-H.; Leclerc, M.; Heeger, A. J. *J. Phys. Chem. C* **2012**, *116*, 11456.

(27) Herguth, P.; Jiang, X.; Liu, M. S.; Jen, A. K. Y. *Macromolecules* **2002**, *35*, 6094.

(28) Svensson, M.; Zhang, F.; Veenstra, S. C.; Verhees, W. J. H.; Hummelen, J. C.; Kroon, J. M.; Inganäs, O.; Andersson, M. R. *Adv. Mater.* **2003**, *15*, 988.

(29) Blouin, N.; Michaud, A.; Leclerc, M. *Adv. Mater.* **2007**, *19*, 2295.

(30) Kim, J. Y.; Lee, K.; Coates, N. E.; Moses, D.; Nguyen, T.-Q.; Dante, M.; Heeger, A. J. *Science* **2007**, *317*, 222.

(31) Wang, E.; Wang, L.; Lan, L.; Luo, C.; Zhuang, W.; Peng, J.; Cao, Y. *Appl. Phys. Lett.* **2008**, *92*, 033307.

(32) Liao, L.; Dai, L.; Smith, A.; Durstock, M.; Lu, J.; Ding, J.; Tao, Y. *Macromolecules* **2007**, *40*, 9406.

(33) Hou, J.; Chen, H.-Y.; Zhang, S.; Li, G.; Yang, Y. *J. Am. Chem. Soc.* **2008**, *130*, 16144.

(34) Beaujuge, P. M.; Pisula, W.; Tsao, H. N.; Ellinger, S.; Mullen, K.; Reynolds, J. R. *J. Am. Chem. Soc.* **2009**, *131*, 7514.

(35) Becke, A. D. *J. Chem. Phys.* **1993**, *98*, 5648.

(36) Lee, C.; Yang, W.; Parr, R. G. *Phys. Rev. B* **1988**, *37*, 785.

(37) Vosko, S. H.; Wilk, L.; Nusair, M. *Can. J. Phys.* **1980**, *58*, 1200.

(38) Stephens, P. J.; Devlin, F. J.; Chabalowski, C. F.; Frisch, M. J. *J. Phys. Chem.* **1994**, *98*, 11623.

(39) Hariharan, P. C.; Pople, J. A. *Theor. Chim. Acta* **1973**, *28*, 213.

(40) Francl, M. M.; Pietro, W. J.; Hehre, W. J.; Binkley, J. S.; Gordon, M. S.; Defrees, D. J.; Pople, J. A. *J. Chem. Phys.* **1982**, *77*, 3654.

(41) As the main interest of this work was to evaluate the intrinsic electronic and optical properties of the DA conjugated backbone, the use of methyl groups is sufficient to include the electron donating effects arising from the alkyl chains appended along the backbones. We note however that when bulky alkyl groups are present, and if these groups interact with a portion of the conjugated backbone, the geometry of the conjugated backbone could be modified and in turn lead to different descriptions of the electronic structure.

(42) Frisch, M. J. T., G. W.; Schlegel, H. B.; Scuseria, G. E.; Robb, M. A.; Cheeseman, J. R.; Montgomery, Jr., J. A.; Vreven, T.; Kudin, K. N.; Burant, J. C.; Millam, J. M.; Iyengar, S. S.; Tomasi, J.; Barone, V.; Mennucci, B.; Cossi, M.; Scalmani, G.; Rega, N.; Petersson, G. A.; Nakatsuji, H.; Hada, M.; Ehara, M.; Toyota, K.; Fukuda, R.; Hasegawa, J.; Ishida, M.; Nakajima, T.; Honda, Y.; Kitao, O.; Nakai, H.; Klene, M.; Li, X.; Knox, J. E.; Hratchian, H. P.; Cross, J. B.; Bakken, V.; Adamo, C.; Jaramillo, J.; Gomperts, R.; Stratmann, R. E.; Yazyev, O.; Austin, A. J.; Cammi, R.; Pomelli, C.; Ochterski, J. W.; Ayala, P. Y.; Morokuma, K.; Voth, G. A.; Salvador, P.; Dannenberg, J. J.; Zakrzewski, V. G.; Dapprich, S.; Daniels, A. D.; Strain, M. C.; Farkas, O.; Malick, D. K.; Rabuck, A. D.; Raghavachari, K.; Foresman, J. B.; Ortiz, J. V.; Cui, Q.; Baboul, A. G.; Clifford, S.; Cioslowski, J.; Stefanov, B. B.; Liu, G.; Liashenko, A.; Piskorz, P.; Komaromi, I.; Martin, R. L.; Fox, D. J.; Keith, T.; Al-Laham, M. A.; Peng, C. Y.; Nanayakkara, A.; Challacombe, M.; Gill, P. M. W.; Johnson, B.; Chen, W.; Wong, M. W.; Gonzalez, C.; and Pople, J. A. *Gaussian, Inc., Wallingford CT* **2004**.

(43) Sobolewski, A. L.; Domcke, W. *Chem. Phys.* **2003**, *294*, 73.

(44) Dreuw, A.; Weisman, J. L.; Head-Gordon, M. *J. Chem. Phys.* **2003**, *119*, 2943.

(45) Dreuw, A.; Head-Gordon, M. *J. Am. Chem. Soc.* **2004**, *126*, 4007.

(46) Chai, J.-D.; Head-Gordon, M. *J. Chem. Phys.* **2008**, *128*, 084106.

(47) Dreuw, A.; Head-Gordon, M. *Chem. Rev.* **2005**, *105*, 4009.

(48) Pandey, L.; Doiron, C.; Sears, J. S.; Bredas, J. L. *Phys. Chem. Chem. Phys.* **2012**, *14*, 14243.

(49) Kanbara, T.; Yamamoto, T. *Macromolecules* **1993**, *26*, 3464.

(50) Ono, K.; Tanaka, S.; Yamashita, Y. *Angew. Chem., Int. Ed. Engl.* **1994**, *33*, 1977.

(51) Brown, N. M. D.; Bladon, P. *Tetrahedron* **1968**, *24*, 6577.

(52) Mataka, S.; Takahashi, K.; Tashiro, M.; Lin, W.-H., *Senryo to Yakuhin* **1988**, 33, 338-48.

(53) Saito, A.; Tanabe, H.; Ueno, K. *Jpn Kokai Tokkyo Koho* **2003**, JP 2003123973.

(54) Temple, C.; Wheeler, G. P.; Elliott, R. D.; Rose, J. D.; Comber, R. N.; Montgomery, J. A. *J. Med. Chem.* **1983**, *26*, 91.

(55) Tsveniashvili, V. Sh.; Todres, Z. V.; Zhdanov, S. I. *Zhurnal Obshchei Khimii* **1968**, 38(8), 1894-7.

(56) Barluenga, J.; Aznar, F.; Liz, R.; Cabal, M.-P. *Synthesis* **1985**, *1985*, 313.

(57) Vasilieva, N. V.; Irtegova, I. G.; Gritsan, N. P.; Lonchakov, A. V.; Makarov, A. Y.; Shundrin, L. A.; Zibarev, A. V. *J. Phys. Org. Chem.* **2010**, *23*, 536.

(58) Atherton, N. M.; Ockwell, J. N.; Dietz, R. *J. Chem. Soc. (A)* **1967**, 771.

(59) Yang, L.; Feng, J.-K.; Ren, A.-M. *J. Mol. Struct. Theochem* **2007**, *816*, 161.

(60) Yang, R.; Tian, R.; Yan, J.; Zhang, Y.; Yang, J.; Hou, Q.; Yang, W.; Zhang, C.; Cao, Y. *Macromolecules* **2004**, *38*, 244.

(61) McNeill, C. R.; Halls, J. J. M.; Wilson, R.; Whiting, G. L.; Berkebile, S.; Ramsey, M. G.; Friend, R. H.; Greenham, N. C. *Adv. Funct. Mater.* **2008**, *18*, 2309.

(62) Zhou, E.; Nakamura, M.; Nishizawa, T.; Zhang, Y.; Wei, Q.; Tajima, K.; Yang, C.; Hashimoto, K. *Macromolecules* **2008**, *41*, 8302.

(63) We based our decision to study the architecture in this manner as such thiophene spacers depicted in the literature are often drawn in reference to the acceptor unit. The thiophene spacers are generally discussed as a means to simply planarize the D and A units (many of which are comprised of six-membered rings that lead to substantial twists along the backbone and, hence, disrupt the conjugation). While we could have also chosen to discuss the electronic effects as T-donor-T vs. acceptor units, we feel that it is quite instructive to have framed the discussion in this manner.

(64) Ashraf, R. S.; Chen, Z.; Leem, D. S.; Bronstein, H.; Zhang, W.; Schroeder, B.; Geerts, Y.; Smith, J.; Watkins, S.; Anthopoulos, T. D.; Sirringhaus, H.; de Mello, J. C.; Heeney, M.; McCulloch, I. *Chem. Mater.* **2010**, *23*, 768.

(65) Scharber, M. C.; Koppe, M.; Gao, J.; Cordella, F.; Loi, M. A.; Denk, P.; Morana, M.; Egelhaaf, H.-J.; Forberich, K.; Dennler, G.; Gaudiana, R.; Waller, D.; Zhu, Z.; Shi, X.; Brabec, C. J. *Adv. Mater.* **2010**, *22*, 367.

(66) Perzon, E.; Wang, X.; Zhang, F.; Mammo, W.; Delgado, J. L.; de la Cruz, P.; Inganäs, O.; Langa, F.; Andersson, M. R. *Synth. Met.* **2005**, *154*, 53.

(67) Yue, W.; Zhao, Y.; Shao, S.; Tian, H.; Xie, Z.; Geng, Y.; Wang, F. *J. Mater. Chem.* **2009**, *19*, 2199.

(68) Muhlbacher, D.; Scharber, M.; Morana, M.; Zhu, Z. G.; Waller, D.; Gaudiana, R.; Brabec, C. *Adv. Mater.* **2006**, *18*, 2884.

(69) Hou, J.; Chen, T. L.; Zhang, S.; Chen, H.-Y.; Yang, Y. *J. Phys. Chem. C* **2009**, *113*, 1601.

(70) Steckler, T. T.; Zhang, X.; Hwang, J.; Honeyager, R.; Ohira, S.; Zhang, X. H.; Grant, A.; Ellinger, S.; Odom, S. A.; Sweat, D.; Tanner, D. B.; Rinzler, A. G.; Barlow, S.; Bredas, J. L.; Kippelen, B.; Marder, S. R.; Reynolds, J. R. *J. Am. Chem. Soc.* **2009**, *131*, 2824.

CHAPTER 4

LOWEST EXCITED STATES AND OPTICAL ABSORPTION SPECTRA OF DONOR-ACCEPTOR COPOLYMERS FOR ORGANIC PHOTOVOLTAICS: A CHARACTERIZATION FROM TUNED LONG-RANGE CORRECTED DENSITY FUNCTIONALS

4.1. Introduction

Importance of low optical-gap DA systems in polymer photovoltaics has been highlighted in the previous chapters. The small optical gap in these materials, intended to increase the overlap between the polymer absorption profile and the incident solar radiation, is mainly related to the presence of low-lying excited states that are expected *a priori* to display significant charge-transfer (CT) character. Gaining a good understanding of the nature of the lowest-lying excited states (excitons) of the copolymers is key since the charge-generation process relies on the dissociation of these excitons at the polymer/fullerene interface. Thus, the description of these low-lying excited states, for instance with DFT,[1,2] can provide insight into the design of improved polymers for OPV.[3]

Optical excitations in these polymers can be computed at the TDDFT level.[4-6] However, conventional semi-local and standard hybrid DFT functionals (such as the popular B3LYP functional[7-9]) are known to fail in giving a proper description of CT excitations, quantitatively and even qualitatively.[10-14] This failure can be traced back to the nonlocal character of the asymptotic 1/r dependence of the CT energy that is either entirely missed in pure semi-local

functionals or only partially accounted for in standard hybrid approaches.[11,15] While standard hybrid approaches include globally a fixed amount of exact nonlocal exchange, LRC hybrid functionals present a distance-dependent fraction of exact exchange through a splitting of the Coulomb operator (see **Equation 2.26**). Here, a semilocal functional approximation describes the short range (first term in **Equation 2.26**) and there is full inclusion of exact exchange in the long range (second term in **Equation 2.26**). In this way, long-range corrected functionals should in principle improve the description of excited states with a CT character. However, in many cases, when using the default values of the range-separation parameter ω, they have been shown to provide unsatisfactory results due to an overestimation of the energies[3,16] of CT states (we note that the smaller the ω value, the larger the extent of the short-range region). Importantly, ω has been demonstrated to be sensitive to the system under consideration.[17-19] Thus, a (physically-based) tuning of the range-separation parameter, an approach pioneered by Baer, Kronik, and their co-workers,[15,20-25] has been shown to improve the description of the fundamental gap and thereby of CT excitations.

Here, we employ two tuned LRC functionals[14,26] to examine the absorption spectra and low-lying excited states in a series of low optical-gap donor-acceptor copolymers of relevance for organic solar-cell applications. The same polymers have been studied recently with the popular B3LYP functional,[3] which will allow us to assess the differences brought by tuned LRC functionals.

After presenting the methodology undertaken, we examine the evolution of the optimized range-separation parameter with size and nature of the system as well as the magnitude of the errors associated with the gap-fitting procedure; a comparison between the long-range corrected functionals is provided. We then compare and discuss the performance of the LRC functionals

(with both tuned and default range-separation parameters) with regard to experiment and to the conventional B3LYP hybrid functional in terms of optical gaps and optical absorption spectra. Importantly, tuned LRC functionals are seen to provide a more localized description of the lowest excited state (exciton) than initially anticipated.

4.2. Methodology

We have considered the low-optical-gap polymers displayed in **Figure 4.1**. The ground-state geometries of oligomers with one to six repeat units [27] were optimized at the B3LYP/6-31G(d,p)[28,29] level using Q-Chem 3.2.[30] Since the combination of electron-rich and electron-deficient moieties in these oligomers is expected *a priori* to result in a CT character of the low-lying excitations, the tuning of the range-separation parameter is based on gap fitting:

$$J_{IP}(\omega) = \left|\varepsilon_H^{\omega}(N) + E_{gs}^{\omega}(N-1) - E_{gs}^{\omega}(N)\right| \tag{4.1}$$

$$J_{EA}(\omega) = \left|\varepsilon_H^{\omega}(N+1) + E_{gs}^{\omega}(N) - E_{gs}^{\omega}(N+1)\right| \tag{4.2}$$

$$J_{gap}(\omega) = J_{IP}(\omega) + J_{EA}(\omega) \tag{4.3}$$

where $\varepsilon_H^{\omega}(N)$ is the HOMO orbital energy for the N-electron system and $E_{gs}^{\omega}(N)$ is the corresponding SCF energy. For each system in its optimized geometry and each functional, the ω value that minimized $J_{gap}(\omega)$ was chosen as the (optimal) tuned ω value. A similar approach to evaluating the optical gap in a donor-acceptor system was recently reported.[21]

The single-point computations of the open-shell cation and anion states were performed with the unrestricted Kohn-Sham formalism. The LRC functionals from Chai and Head-Gordon (ωB97) [14] and from Baer, Neuhauser, and Livshits (BNL) [26] were employed with a 6-31G(d,p) basis.

Optical absorption spectra were simulated (based on a 0.35 eV FWHM Gaussian broadening of the vertical transition energies and associated oscillator strengths) with TDDFT using the LRC functionals (with both default and tuned ω values) as well as with B3LYP and the same 6-31G(d,p) basis (Q-Chem 3.2). Additionally, we have explored the impact of the polarity of the solvent on the computed absorption spectra by considering the polarizable continuum model (PCM) [31,32] under the linear-response approximation (non-equilibrium excited-state solvation), with the choice of solvent parameters corresponding to the solvents used in the reported experimental spectra.[33-36] The TDDFT calculations for the largest oligomers (five and six repeat units) and in the presence of the dielectric medium were performed using Gaussian-09 Revision B.01.[37] SG1grids were employed in all cases to ensure that the Gaussian-09 results matched results from Q-Chem. The B3LYP/6-31G(d,p) structures, the optimized values of the range-separation parameters, and the entirety of the TDDFT results are included in the Ancillary Materials.

4.3. Results and discussion

4.3.1. System dependence of the range-separation parameter

The chemical structures of the six polymers examined in this work are presented in **Figure 4.1**. The ground-state geometries are similar to the tetramer structures described by Risko *et al.*[3] The evolution of the tuned range-separation parameter with system size is plotted as a function of number of repeat units in **Figure 4.2**. In most systems, the characteristic lengths $(1/\omega)$ [15] increase from *ca.* 5.1 bohr (1 bohr = 0.53 Å) for the monomers and saturate after about 4 repeat units to reach 8 – 8.5 bohr. The exceptions are: (i) PCDTBT, which presents a longer conjugated path per repeat unit and where the characteristic length saturates after 2–3 repeat

units to ~6.6 bohr; and (ii) PCPDTBT, for which the characteristic length has not been reached after 6 repeat units. As discussed by Refaely-Abramson *et al.* [15] and Körzdörfer *et al.*,[18] these results confirm that the characteristic lengths depend on the chemical nature of the system and the system size. In our earlier work,[18] we suggested that the characteristic length is, in an interesting way, a description of the extent of conjugation in the system. For the sake of comparison, we note that for oligothiophenes $1/\omega$ saturates to about 6.75 bohr, which means that the polymers investigated here, provided they maintain a (nearly) coplanar backbone in the solid state, appear to be more conjugated than polythiophene itself. Importantly, the tuned ω values (on the order of 0.10 – 0.15 $bohr^{-1}$ in the longest oligomers) are significantly different from the default values for the ωB97 and BNL functionals (0.4 and 0.5 $bohr^{-1}$, respectively). As we describe below, this will have a substantial impact on the computed optical properties.

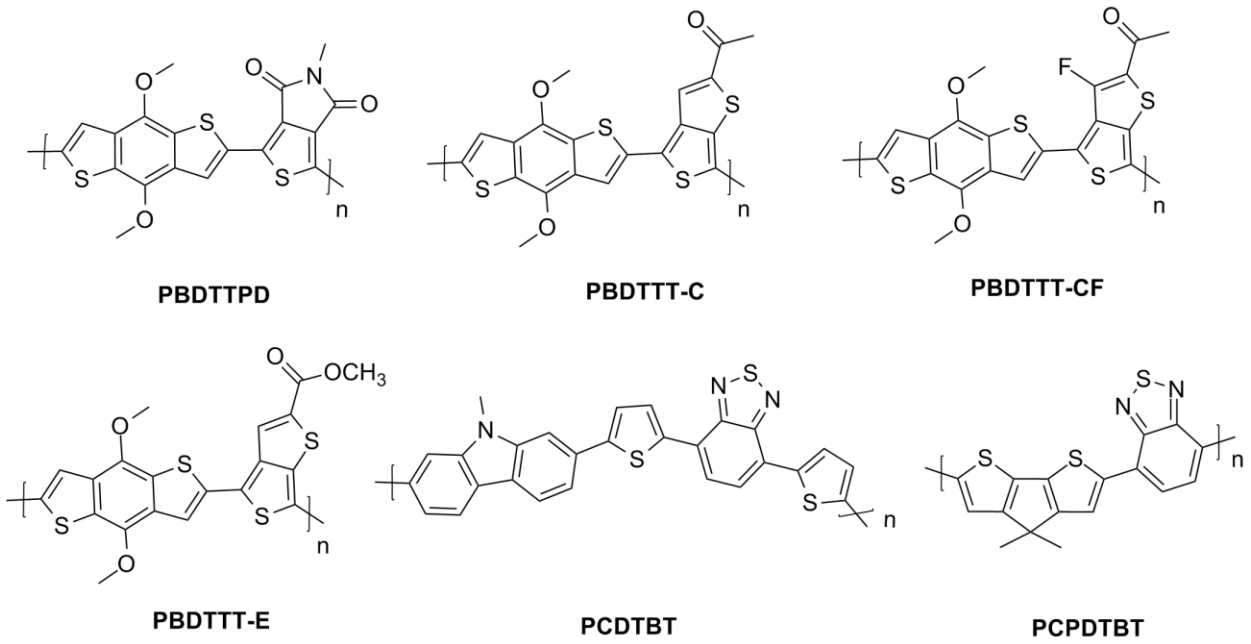

Figure 4.1 Chemical structures of the copolymers considered in this work. In the calculations, values of n from 1 to 6 were considered (each oligomer being capped by hydrogen atoms). The abbreviations (that are those commonly used in the OPV literature) stand for: PBDTTPD[33] ≡ poly[4,8-bis-alkyloxy-benzo[1,2-*b*:4,5-*b'*]dithiophene-2,6-diyl-N-alkylthieno[3,4-*c*]pyrrole-4,6-dione-1,2,diyl]; PBDTTT-C[34] ≡ poly[4,8-bis-alkyloxy-benzo[1,2-*b*:4,5-*b'*]dithiophene-2,6-diyl-*alt*-4-(alkyl-1-one)thieno[3,4-*b*]thiophene-2,6-diyl]; PBDTTT-CF[34] ≡ poly[4,8-bis-alkyloxy-

benzo[1,2-*b*:4,5- *b′*]dithiophene-2,6-diyl-*alt*-4-(alkyl-1-one)-3-fluorothieno[3,4-*b*]thiophene-2,6-diyl]; PBDTTT-E[34] ≡ poly[4,8-bis-alkyloxy-benzo[1,2-*b*:4,5-*b′*]dithiophene-2,6-diyl-*alt*-4-alkylester-thieno[3,4-*b*]thiophene-2,6-diyl]; PCDTBT[35] ≡ poly[N-alkyl-2,7-carbazole-*alt*-5,5-(4′,7′-di-2-thienyl-2′,1′,3′-benzothiadiazole); PCPDTBT[36] ≡ poly[2,6-(4,4-bis-alkyl-4*H*-cyclopenta[2,1-*b*;3,4-*b′*]dithiophene)-alt-4,7-(2,1,3-benzothiadiazole)].

The lower panel of **Figure 4.2** presents the errors related to the gap-fitting procedure for which J_{gap} should be ideally equal to 0. The gap-fitting errors for the longer oligomers are typically around 0.04 eV; in all cases, they are well below 0.1 eV. Such small errors in the gap fitting, in principle, should lead to a reliable description of the energies of the lowest excited states even if they possess a significant CT character.

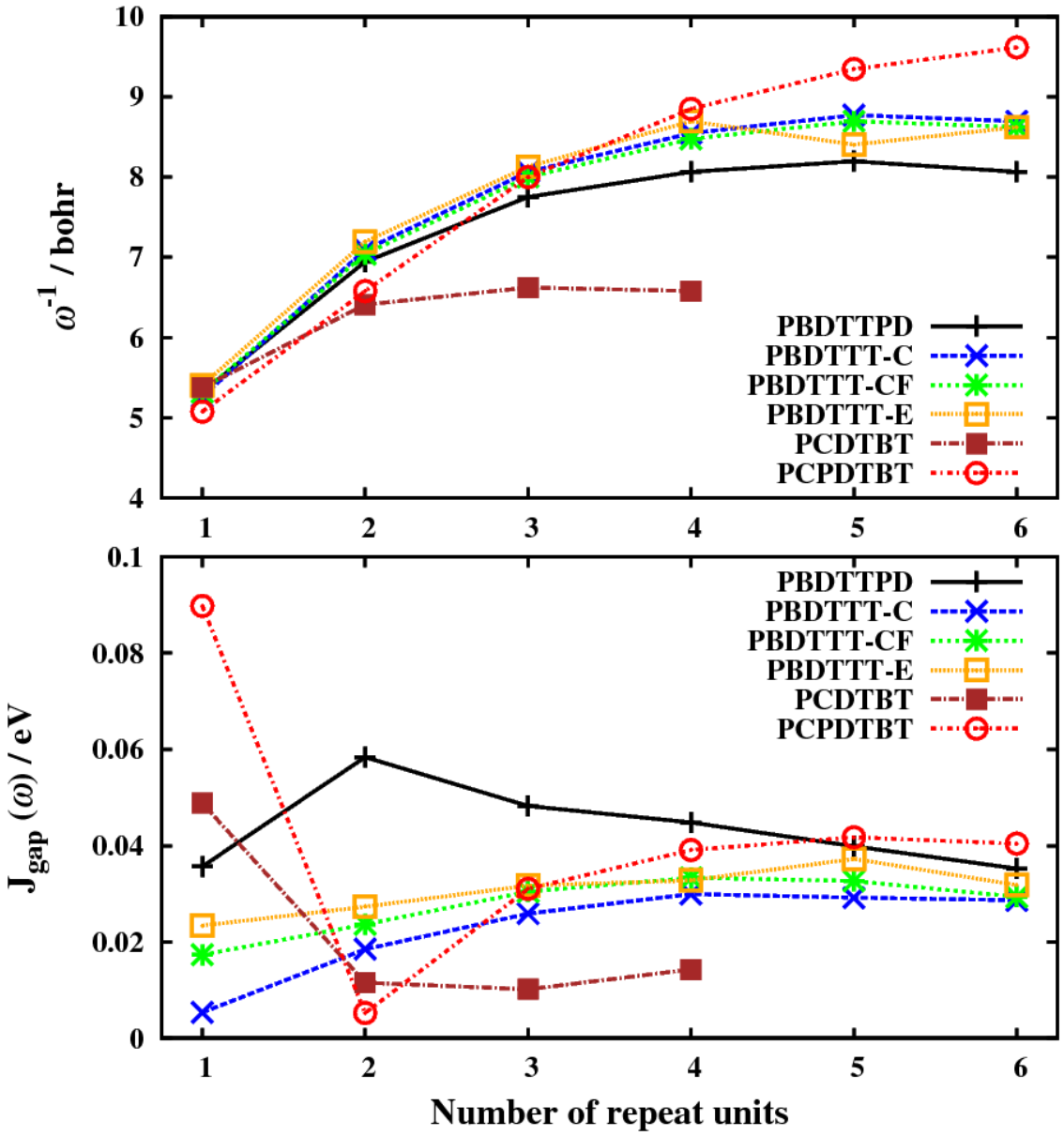

Figure 4.2 Characteristic lengths 1/ω (top panel) and corresponding values of $J_{gap}(\omega)$ (bottom panel) as a function of oligomer size from tuned ωB97/6-31G(d,p).

4.3.2. Is the choice of semi-local functional approximation at short-range critical?

With a view to explore the dependence of the characteristic lengths and the description of the CT energies, oscillator strengths, and optical absorption spectra on the specific choice of the LRC functional, we also carried out gap-fitting for BNL and evaluated the vertical excited-state

properties at the TDDFT level for the oligomers of **Figure 4.1** with 1 to 4 repeat units. The optimized ω values are very similar for both functionals (see **Table A.4.1**), with the largest difference between the two functionals in the tuned ω value for a given oligomer size being just 0.014 $bohr^{-1}$. Nearly identical optical absorption spectra are obtained for ωB97 and BNL with the tuned range-separation parameter, see **Figure 4.3**. These results confirm that, when tuning the range-separation parameter, the differences in the semilocal approximations to exchange and correlation (modified form of B97[38] and LYP[8] in ωB97 and BNL, respectively) do not significantly impact the description of the computed optical properties.[18] As a result, the gap-fitted ω optimization and subsequent evaluation of the longer oligomers (pentamers and hexamers) were carried out with only ωB97. (Also, for the sake of conciseness, **Figure 4.3** and the remaining figures in the main text deal only with the results for PBDTTT-CF and PCDTBT, taken as representative examples; additional results can be found in the Ancillary Material).

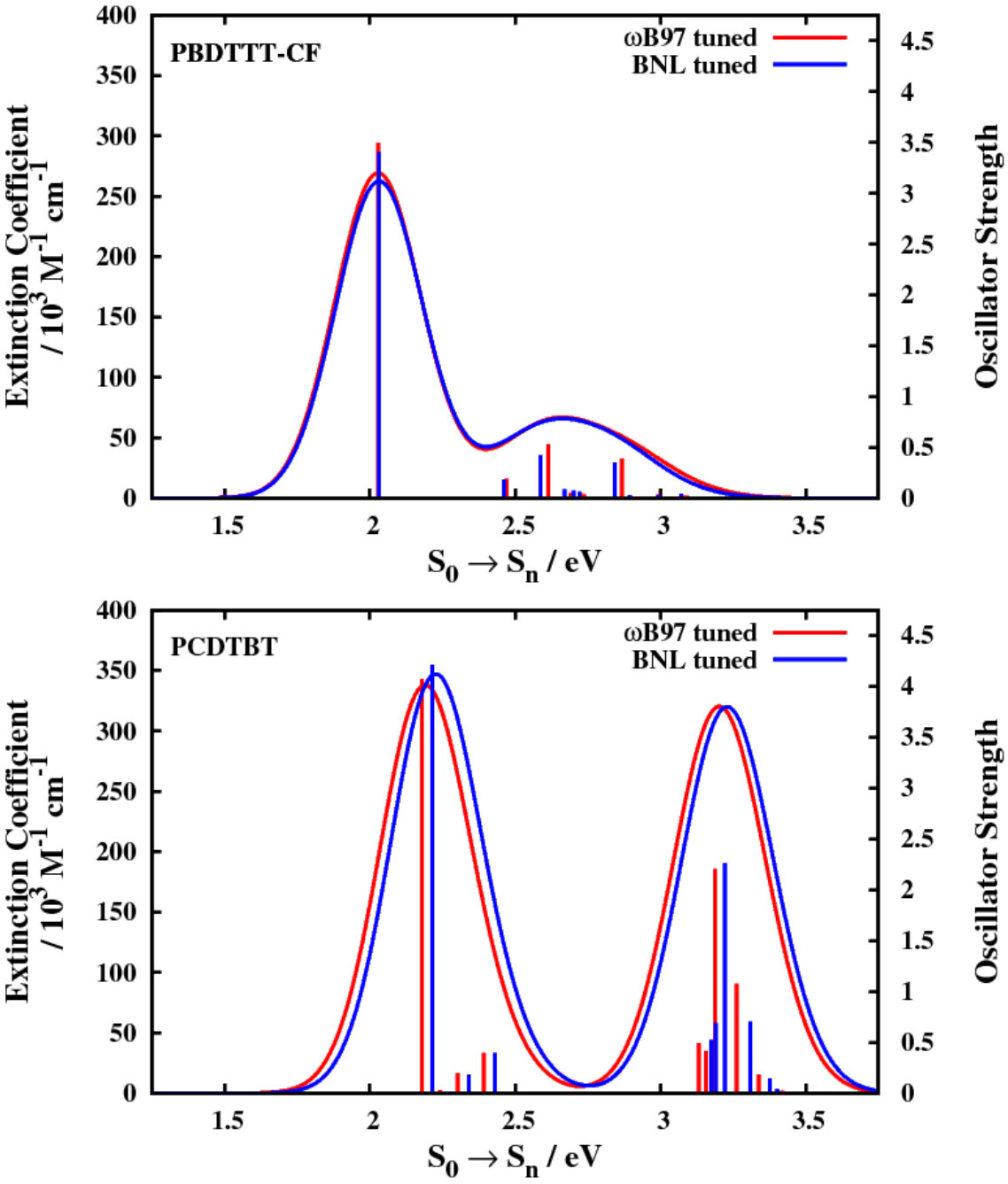

Figure 4.3 Calculated optical absorption spectra from tuned ωB97 and BNL for the tetramers of the representative systems PBDTTT-CF and PCDTBT at the TDDFT level.

4.3.3. Evolution of S_1 energy with oligomer size

Table A.4.2 lists S_1 energies for each DA oligomer with varying oligomer size. The TDDFT first transition energy ($S_0 \rightarrow S_1$) of the oligomers begins leveling off after about 5 repeat units (3 for PCDTBT). This evolution is similar to the saturation of $1/\omega$ with increasing oligomer length. **Figure 4.4** represents the evolution of the oligomer $S_0 \rightarrow S_1$ energy as a function of the inverse number of repeat units (1/n). The B3LYP $S_0 \rightarrow S_1$ energies are consistently 0.15 – 0.50 eV below the tuned ωB97 energies; these energy differences are largest for monomers and progressively reduce with the increase in oligomer size. **Figure 4.4** also includes linear (1/n) and exponential [39] fits of the $S_0 \rightarrow S_1$ energies with respect to the inverse number of repeat units. The exponential fit is based on the equation:

$$E(n) = E_\infty + (E_1 - E_\infty)\exp[-a(n-1)] \qquad (4.4)$$

which gives the $S_0 \rightarrow S_1$ energy, E(n), for a system with n repeat units given the values for E_1 and E_∞ that represent the $S_0 \rightarrow S_1$ energies for the monomer and polymer, respectively. Parameter *a* describes how quickly E(n) saturates from the monomer to the polymer limit, E_∞. The $S_0 \rightarrow S_1$ energies for the oligomer sizes considered here follow very well a linear relationship with 1/n (R^2 values > 0.99) for all functionals considered (B3LYP and the tuned and default ωB97, see **Table A.4.3**). However, saturation of E(n) starts appearing in the exponential fit at about the size of the longest oligomers; these results confirm the substantial conjugation length manifested by these copolymers.

4.3.4. Comparison of simulated optical spectra

We will discuss the performance of the ωB97 (with both tuned and default ω) and B3LYP in comparison with experiment by considering the longest oligomers evaluated here. In

view of the progressions in **Figure 4.4**, computations on even longer oligomers might result in slightly lower excitation energies; however, this effect is not expected to be larger than ~0.1 eV even when based on the linear extrapolations that tend to exaggerate the progression near the polymer limit. We note that the tuned and default ωB97 and B3LYP $S_0 \rightarrow S_1$ energies extrapolated to the polymer limit using the linear fit are 0.15 – 0.30 eV lower than the ones derived through the exponential fit for all copolymers, which is consistent with previous results.[40] The average values for *a* (**Equation 4**) evaluated for tuned ωB97 and B3LYP (when considering the systems for which we went up to the hexamers) are 0.89 and 0.75, respectively; this means a slower saturation of E(n) from B3LYP, in line with the tendency of conventional DFT to provide an overdelocalized description of the wave functions in π-conjugated materials.[41]

We now turn our attention to the performance of ωB97 and B3LYP in comparison to the experimental optical absorption spectra. The experimental data were taken from the works of Zhang *et al.*,[33] Chen *et al.*,[34] Blouin *et al.*,[35] and Muhlbacher *et al.*[36] **Figure 4.5** shows the absorbance spectra of the systems compared with the computed spectra at the TDDFT level with the ωB97 (tuned and default) and B3LYP functionals. In all systems, B3LYP underestimates the energy of the lowest absorption bands, as a result of too large a charge-transfer character of the excited states. Indeed, the mixing of charge-transfer configurations that are too low in energy with local excitations leads to an underestimation of the excited-state energies (and the appearance of a large set of low-lying "dark" states) in the TDDFT spectrum with B3LYP.[42,43] The default ωB97 functional provides for an overly localized description, resulting in an overestimation of the charge-transfer configuration energies and leading to too blue-shifted absorptions. Tuned ωB97 provides for the best comparison with the experimental absorption

spectra, which can be related to an improved balance in the description of the local and CT excitations provided by the optimization of the range-separation parameter.

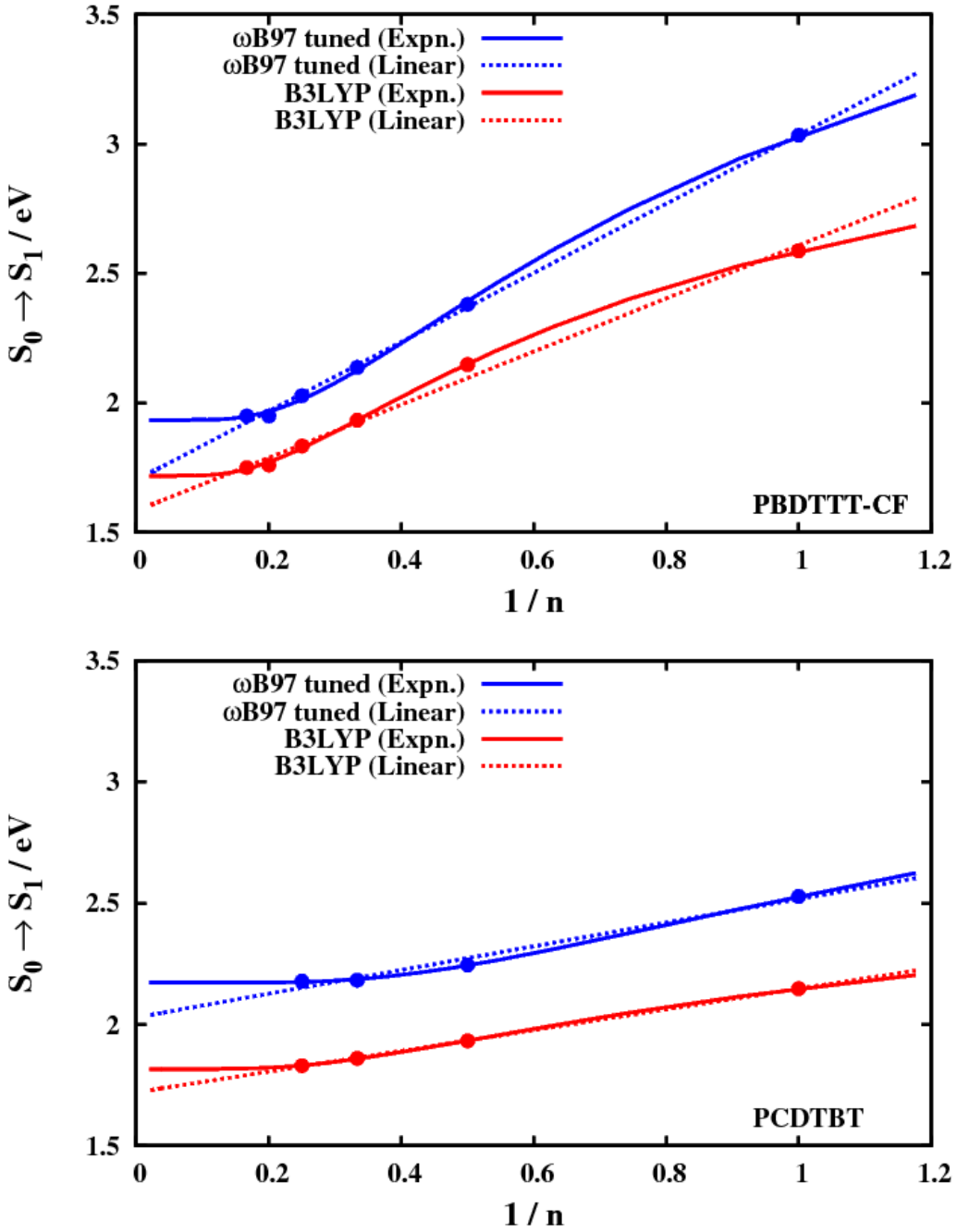

Figure 4.4 Evolution of the first transition energy ($S_0 \rightarrow S_1$) with respect to the inverse number of repeat units (1/n) at the TDDFT level for the B3LYP and tuned ωB97 functionals in the case of the representative systems PBDTTT-CF and PCDTBT.

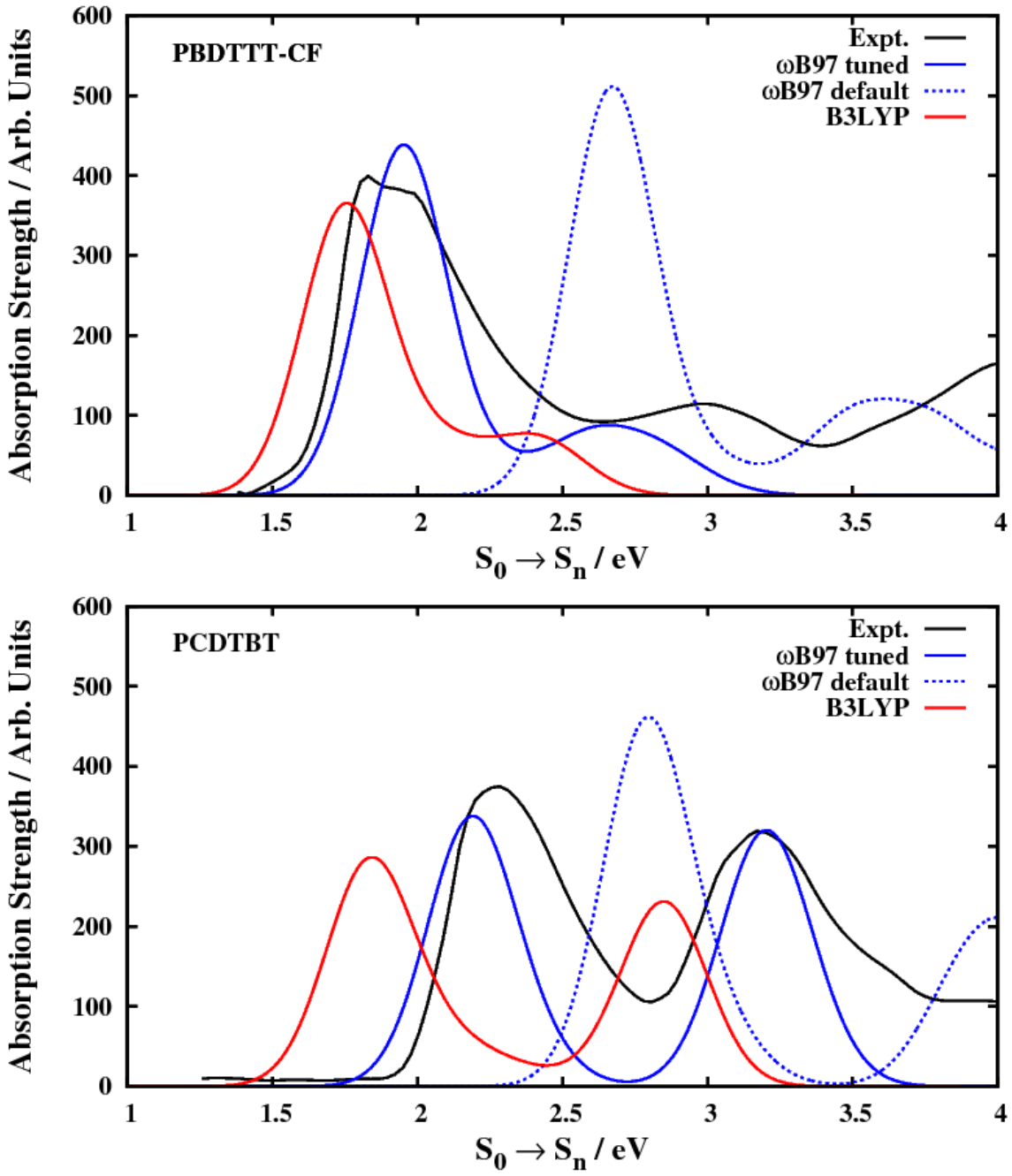

Figure 4.5 Calculated ("gas-phase") optical absorption spectra with the ωB97 (default and tuned ω) and B3LYP functionals for the hexamer of PBDTTT-CF and tetramer of PCDTBT compared to the digitized experimental data.

We note that for the longest oligomers, we have also explored the impact of solvent polarity on the computed optical absorption spectra. Interestingly, the results are found to be very

similar to the "gas-phase" results; only extremely small red shifts are observed as illustrated in **Figure A.4.5**.

4.3.5. Characterization of the lowest excited-state

In order to examine more closely the nature of the lowest electronic transitions, natural transition orbitals (NTOs) [44] for the $S_0 \rightarrow S_1$ excitations were evaluated. **Figure 4.6** illustrates the dominant particle-hole contributions and associated weights for the tetramer of PCDTBT. For B3LYP, the excitation is a contribution of two particle-hole pairs, where in each the hole is largely delocalized and the electron is localized over a benzothiadiazole unit. However, for tuned ωB97, the $S_0 \rightarrow S_1$ excitation is described by three particle-hole pairs, where each hole is localized within a specific thiophene – benzene (belonging to a benzothiadiazole segment) – thiophene segment and the electron localized within the benzothiadiazole unit. Importantly, the description of the $S_0 \rightarrow S_1$ transition as corresponding to excitations essentially localized within such dithienylbenzothiadiazole segments is consistent with the negligible solvatochromism recently reported for these systems.[45] In fact, the decreased absorption energy and increased oscillator strength in PCDTBT with increasing chain length can be seen to arise not from delocalized charge-transfer excitations involving an electron-donating carbazole but from *the coupling of the dithienylbenzothiadiazole-localized excitations along the chain*. Although not always as strong, the $S_0 \rightarrow S_1$ NTO descriptions for the other oligomers exhibit similar differences between B3LYP and tuned ωB97. Thus, the more balanced description from tuned ωB97 yields optical absorption spectra that best match experiment and *provides a more localized picture of the lowest singlet exciton* than anticipated from the donor-acceptor nature of the copolymers.

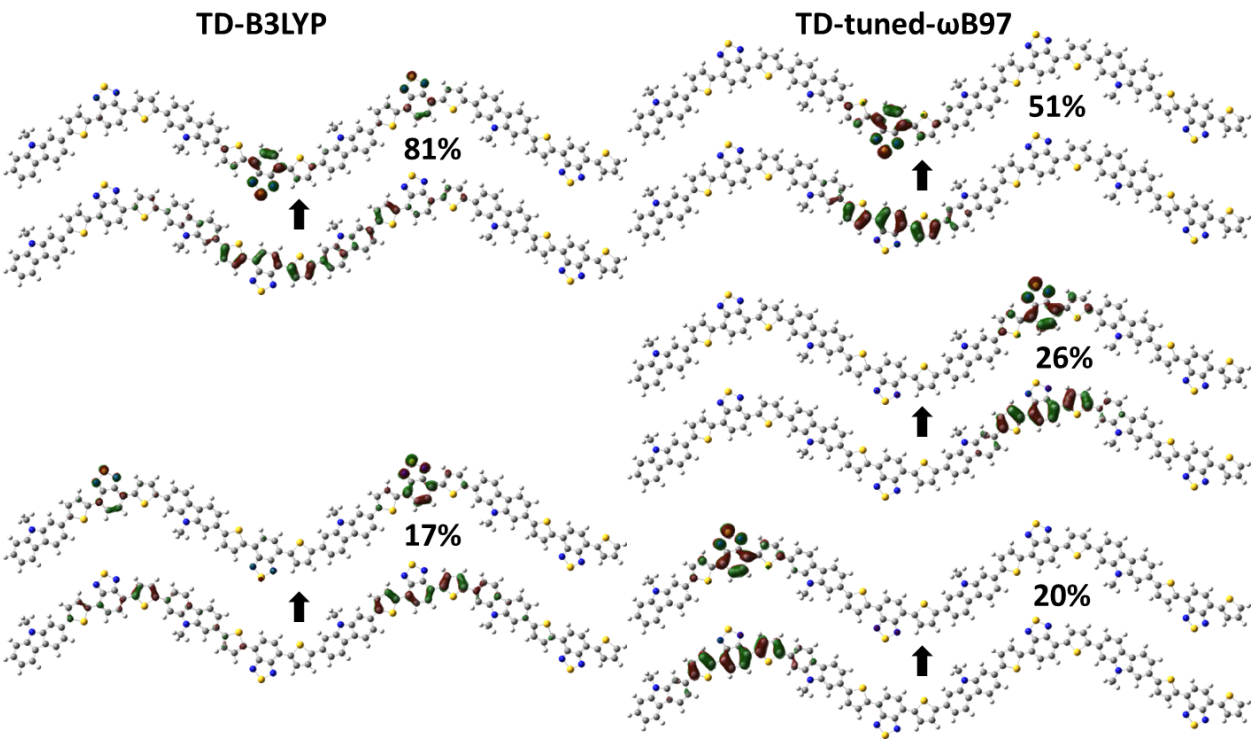

Figure 4.6 TDDFT natural transition orbitals (isovalue surface 0.03 a.u.) for $S_0 \rightarrow S_1$ from B3LYP and tuned ωB97 for the tetramer of PCDTBT. The weight of the hole-particle contribution to the excitation also included.

4.4. Conclusions

The long-range corrected functionals have been previously applied to prototypical π-conjugated systems (polyacetylenes, polythiophenes, and oligoacenes).[18,21] The tuning of the range-separation parameter (ω) was shown to provide a balanced description of the localization / delocalization character of the wavefunctions; the value of the (tuned) ω was noted as an indicator of the conjugation of the system.[18] In this Chapter, we applied this methodology to a series of small-optical gap systems consisting of donor and acceptor moieties to correctly describe the charge-transfer character of the electronic excitations.

Our work in this Chapter confirms the ability of tuned LRC functionals to provide a description of the lowest excited states in these low-optical-gap polymers leading to better agreement with experimental optical absorption spectra than hybrid functionals such as B3LYP (which systematically underestimates the energy of charge-transfer configurations) or standard LRC functionals.

Based on the tuned $1/\omega$ values for the donor-acceptor copolymers and oligothiophenes (that saturate about 8 – 8.5 and 6.75 bohr, respectively), the donor-acceptor copolymers investigated here are found to be effectively somewhat more conjugated than polythiophene (provided these copolymers maintain a (nearly) coplanar backbone in the solid state).

From the computational study of many donor-acceptor copolymers, the HOMO wavefunction in a donor-acceptor copolymer is generally considered to be delocalized over both donor and acceptor units. Here, by using tuned LRC functionals and inspecting the natural transition orbitals (NTOs) that have the largest contributions to the lowest excited state, we obtain a new, very different picture of the lowest singlet exciton: the chromophoric unit is found to be much more localized than initially expected from the donor-acceptor character of the small-gap copolymers but also to be strongly coupled to the nearest similar chromophoric units to its right and its left.

We note that these excitons must dissociate at the HTM:ETM interface for the generation of photocurrent. Reliable descriptions of CT states that occur at or near the HTM:ETM interfaces are therefore important. Chapters 5 and 6 provide our initial studies towards understanding the molecular interfacial interactions of the hole- and electron-transport materials and how these affect CT state energies and other important parameters that impact exciton dissociation.

4.5. References

(1) Hohenberg, P.; Kohn, W. *Phys. Rev.* **1964**, *136*, B864.

(2) Kohn, W.; Sham, L. J. *Phys. Rev.* **1965**, *140*, A1133.

(3) Risko, C.; McGehee, M. D.; Bredas, J.-L. *Chem. Sci.* **2011**, *2*, 1200.

(4) Runge, E.; Gross, E. K. U. *Phys. Rev. Lett.* **1984**, *52*, 997.

(5) Casida, M. E. In *Recent Advances in Density Functional Methods, Part I*; Chong, D. P., Ed.; World Scientific: Singapore, 1995, p 155.

(6) Casida, M. E.; Gutierrez, F.; Guan, J. G.; Gadea, F. X.; Salahub, D.; Daudey, J. P. *J. Chem. Phys.* **2000**, *113*, 7062.

(7) Becke, A. D. *J. Chem. Phys.* **1993**, *98*, 5648.

(8) Lee, C.; Yang, W.; Parr, R. G. *Phys. Rev. B* **1988**, *37*, 785.

(9) Stephens, P. J.; Devlin, F. J.; Chabalowski, C. F.; Frisch, M. J. *J. Phys. Chem.* **1994**, *98*, 11623.

(10) Sobolewski, A. L.; Domcke, W. *Chem. Phys.* **2003**, *294*, 73.

(11) Dreuw, A.; Weisman, J. L.; Head-Gordon, M. *J. Chem. Phys.* **2003**, *119*, 2943.

(12) Dreuw, A.; Head-Gordon, M. *J. Am. Chem. Soc.* **2004**, *126*, 4007.

(13) Dreuw, A.; Head-Gordon, M. *Chem. Rev.* **2005**, *105*, 4009.

(14) Chai, J.-D.; Head-Gordon, M. *J. Chem. Phys.* **2008**, *128*, 084106.

(15) Refaely-Abramson, S.; Baer, R.; Kronik, L. *Phys. Rev. B* **2011**, *84*, 075144.

(16) Polander, L. E.; Pandey, L.; Barlow, S.; Tiwari, S. P.; Risko, C.; Kippelen, B.; Brédas, J.-L.; Marder, S. R. *J. Phys. Chem. C* **2011**, *115*, 23149.

(17) Krukau, A. V.; Scuseria, G. E.; Perdew, J. P.; Savin, A. *J. Chem. Phys.* **2008**, *129*, 124103.

(18) Körzdörfer, T.; Sears, J. S.; Sutton, C.; Bredas, J.-L. *J. Chem. Phys.* **2011**, *135*, 204107.

(19) Savin, A.; Flad, H.-J. *Int. J. Quantum Chem.* **1995**, *56*, 327.

(20) Baer, R.; Livshits, E.; Salzner, U. *Annu. Rev. Phys. Chem.* **2010**, *61*, 85.

(21) Karolewski, A.; Stein, T.; Baer, R.; Kummel, S. *J. Chem. Phys.* **2011**, *134*, 151101.

(22) Stein, T.; Kronik, L.; Baer, R. *J. Chem. Phys.* **2009**, *131*, 244119.

(23) Stein, T.; Kronik, L.; Baer, R. *J. Am. Chem. Soc.* **2009**, *131*, 2818.

(24) Kuritz, N.; Stein, T.; Baer, R.; Kronik, L. *J. Chem. Theory Comput.* **2011**, *7*, 2408.

(25) Stein, T.; Eisenberg, H.; Kronik, L.; Baer, R. *Phys. Rev. Lett.* **2010**, *105*, 266802.

(26) Livshits, E.; Baer, R. *Phys. Chem. Chem. Phys.* **2007**, *9*, 2932.

(27) Monomer to tetramer for PCDTBT (see discussion for details)

(28) Hariharan, P. C.; Pople, J. A. *Theor. Chim. Acta* **1973**, *28*, 213.

(29) Francl, M. M.; Pietro, W. J.; Hehre, W. J.; Binkley, J. S.; Gordon, M. S.; Defrees, D. J.; Pople, J. A. *J. Chem. Phys.* **1982**, *77*, 3654.

(30) Shao, Y.; Molnar, L. F.; Jung, Y.; Kussmann, J.; Ochsenfeld, C.; Brown, S. T.; Gilbert, A. T. B.; Slipchenko, L. V.; Levchenko, S. V.; O'Neill, D. P.; DiStasio Jr, R. A.; Lochan, R. C.; Wang, T.; Beran, G. J. O.; Besley, N. A.; Herbert, J. M.; Yeh Lin, C.; Van Voorhis, T.; Hung Chien, S.; Sodt, A.; Steele, R. P.; Rassolov, V. A.; Maslen, P. E.; Korambath, P. P.; Adamson, R. D.; Austin, B.; Baker, J.; Byrd, E. F. C.; Dachsel, H.; Doerksen, R. J.; Dreuw, A.; Dunietz, B. D.; Dutoi, A. D.; Furlani, T. R.; Gwaltney, S. R.; Heyden, A.; Hirata, S.;

Hsu, C.-P.; Kedziora, G.; Khalliulin, R. Z.; Klunzinger, P.; Lee, A. M.; Lee, M. S.; Liang, W.; Lotan, I.; Nair, N.; Peters, B.; Proynov, E. I.; Pieniazek, P. A.; Min Rhee, Y.; Ritchie, J.; Rosta, E.; David Sherrill, C.; Simmonett, A. C.; Subotnik, J. E.; Lee Woodcock Iii, H.; Zhang, W.; Bell, A. T.; Chakraborty, A. K.; Chipman, D. M.; Keil, F. J.; Warshel, A.; Hehre, W. J.; Schaefer Iii, H. F.; Kong, J.; Krylov, A. I.; Gill, P. M. W.; Head-Gordon, M. *Phys. Chem. Chem. Phys.* **2006**, *8*, 3172.

(31) Miertuš, S.; Scrocco, E.; Tomasi, J. *Chem. Phys.* **1981**, *55*, 117.

(32) Tomasi, J.; Mennucci, B.; Cammi, R. *Chem. Rev.* **2005**, *105*, 2999.

(33) Zhang, Y.; Hau, S. K.; Yip, H.-L.; Sun, Y.; Acton, O.; Jen, A. K.-Y. *Chem. Mater.* **2010**, *22*, 2696.

(34) Chen, H.-Y.; Hou, J.; Zhang, S.; Liang, Y.; Yang, G.; Yang, Y.; Yu, L.; Wu, Y.; Li, G. *Nat. Photonics* **2009**, *3*, 649.

(35) Blouin, N.; Michaud, A.; Leclerc, M. *Adv. Mater.* **2007**, *19*, 2295.

(36) Muhlbacher, D.; Scharber, M.; Morana, M.; Zhu, Z. G.; Waller, D.; Gaudiana, R.; Brabec, C. *Adv. Mater.* **2006**, *18*, 2884.

(37) Frisch, M. J. T., G. W.; Schlegel, H. B.; Scuseria, G. E.; Robb, M. A.; Cheeseman, J. R.; Scalmani, G.; Barone, V.; Mennucci, B.; Petersson, G. A.; Nakatsuji, H.; Caricato, M.; Li, X.; Hratchian, H. P.; Izmaylov, A. F.; Bloino, J.; Zheng, G.; Sonnenberg, J. L.; Hada, M.; Ehara, M.; Toyota, K.; Fukuda, R.; Hasegawa, J.; Ishida, M.; Nakajima, T.; Honda, Y.; Kitao, O.; Nakai, H.; Vreven, T.; Montgomery, Jr., J. A.; Peralta, J. E.; Ogliaro, F.; Bearpark, M.; Heyd, J. J.; Brothers, E.; Kudin, K. N.; Staroverov, V. N.; Kobayashi, R.; Normand, J.; Raghavachari, K.; Rendell, A.; Burant, J. C.; Iyengar, S. S.; Tomasi, J.; Cossi, M.; Rega, N.; Millam, N. J.; Klene, M.; Knox, J. E.; Cross, J. B.; Bakken, V.; Adamo, C.; Jaramillo, J.; Gomperts, R.; Stratmann, R. E.; Yazyev, O.; Austin, A. J.; Cammi, R.; Pomelli, C.; Ochterski, J. W.; Martin, R. L.; Morokuma, K.; Zakrzewski, V. G.; Voth, G. A.; Salvador, P.; Dannenberg, J. J.; Dapprich, S.; Daniels, A. D.; Farkas, Ö.; Foresman, J. B.; Ortiz, J. V.; Cioslowski, J.; Fox, D. J. *Gaussian Inc., Wallingford CT* **2010**.

(38) Becke, A. D. *J. Chem. Phys.* **1997**, *107*, 8554.

(39) Meier, H.; Stalmach, U.; Kolshorn, H. *Acta Polym.* **1997**, *48*, 379.

(40) Gierschner, J.; Cornil, J.; Egelhaaf, H.-J. *Adv. Mater.* **2007**, *19*, 173.

(41) Mori-Sánchez, P.; Cohen, A. J.; Yang, W. *Phys. Rev. Lett.* **2008**, *100*, 146401.

(42) Magyar, R. J.; Tretiak, S. *J. Chem. Theory Comput.* **2007**, *3*, 976.

(43) Lange, A.; Herbert, J. M. *J. Chem. Theory Comput.* **2007**, *3*, 1680.

(44) Martin, R. L. *J. Chem. Phys.* **2003**, *118*, 4775.

(45) Banerji, N.; Gagnon, E.; Morgantini, P.-Y.; Valouch, S.; Mohebbi, A. R.; Seo, J.-H.; Leclerc, M.; Heeger, A. J. *J. Phys. Chem. C* **2012**, *116*, 11456.

CHAPTER 5

EFFECT OF ALKYL SUBSTITUTIONS ON THE STRUCTURAL AND ELECTRONIC PROPERTIES OF POLY(ALKYL)THIOPHENES

5.1. Introduction

As discussed in earlier chapters, the design and use of better photoactive materials have key impact on the performance improvements in photovoltaic cells.[1,2,3] In addition to the use of suitable electron-donating and electron-withdrawing substituents (Chapter 3), attachment of linear, bulky, or conjugated side chains are alternative methods to control material properties.[4] Conjugated side chains can help increase the conjugation path and thereby extend and broaden light absorption.[5,6] However, bulky rings or substituents are likely to negatively impact PCE as excessive twisting in the polymer backbone affects solid-state packing and consequently reduces J_{SC}.

The bulky substituents have the potential to affect not only the packing structures and charge transport properties, but also the device V_{OC}. They can help extend V_{OC} through (i) increased IP and (2) reduced dark current (from reduction in intermolecular electronic coupling between the HTM and ETM at the interface).[7] Acquiring a balance in the tradeoff of V_{OC} and J_{SC} is therefore is the key. The goal of work in this chapter is therefore to understand how such a balance is achieved with the system of materials described below.

Polythiophene derivatives are amongst the most widely used hole-transport materials in OPV and are attractive model systems to investigate the influence on backbone twisting.[8-10]

Herein, we perform a systematic study on the effect of alkyl substitutions (in oligomers of thiophene, see **Figure 5.1** and **A.5.1**) on the geometric structure including backbone twisting. The effects of backbone twisting on oligomer electronic and optical properties are discussed. We also evaluate the impact of backbone twisting on oligomer:fullerene (C_{60}) interactions, electronic couplings, and CT state energies. Calculated values are compared against measured ionization potentials, charge-carrier mobilities, and photovoltaic characteristics of polymer:fullerene blends (The polymers considered include a family of poly(hexyl)thiophenes (regioregular and regiorandom P3HT, PDHTT, and PDHBT, see **Figure 5.1**). We show that 3,4-dialkyl substituents have significant influence on the degree of backbone twisting affecting oligomer IP as well as oligomer:fullerene interactions and CT state energies. Calculated values correspond well with measured properties in both isolated polymer form and devices containing the polymer:fullerene blend (the experimental data were provided by the groups of Professors Bao, McGehee, and Salleo at Stanford University and are detailed elsewhere[11]).

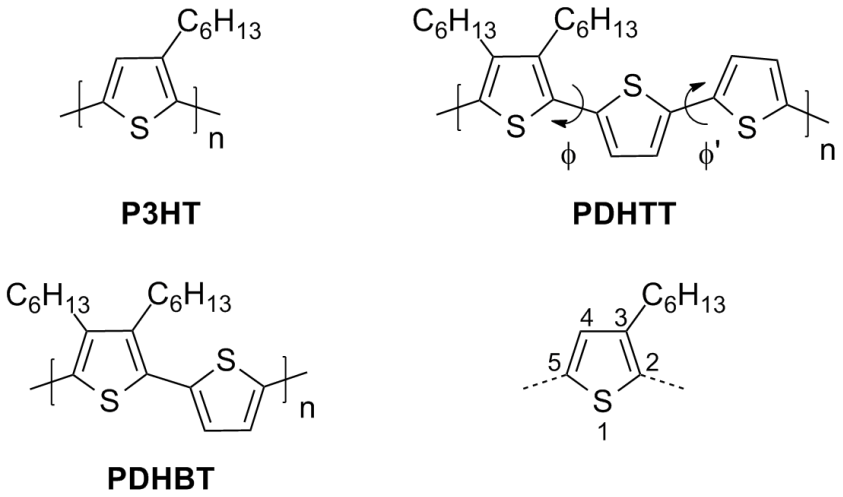

Figure 5.1 Monomer structures of poly(3-hexylthiophene) **P3HT**, poly(3,4-dihexyl-2,2':5',2''-terthiophene) **PDHTT**,[12,13] and poly(3,4-dihexyl-2,2'-bithiophene) **PDHBT**.[14] Chemical structures of the two regio-random P3HT analogs are provided in **Figure A.5.1** (ancillary materials). The atom numbering scheme is shown for reference.

5.2. Computational methodology

Calculations for ("gas-phase") isolated oligomers and C_{60} were carried out at the B3LYP[15-17]/6-31G(d,p)[18,19] level. Vertical excitation of the ground-state geometries was carried using TDDFT at the same level. Oligomer:C_{60} separation distances were determined as a function of the largest binding energy (corresponding to total single-point self-consistent field (SCF) energy differences with respect to infinite separation) using Grimme's dispersion-corrected functional B97D.[20] The pentagonal face of the C_{60} was placed parallel to the plane of the central unsubstituted thiophene unit in PDHTT and PDHBT or hexyl-substituted thiophene unit in P3HT and RRa-P3HT. The separation distance was varied from 2.8 – 4.4 Å. Because the hexyl substituents project away from the plane of the oligomer backbone (in all oligomers except planar P3HT) and considering the possibility that C_{60} can approach the plane of the central unsubstituted (or hexyl substituted) thiophene unit from above or below the plane, two different oligomer-C_{60} conformations were selected; conformations where C_{60} approaches the polymer directly facing the hexyl substituents are referred to as "inverted" (see **Figures A.5.14 – A.5.16**). These calculations were performed using the Gaussian (09 Revision A.02)[21] suite of programs. CT state energies (based on the oligomer:C_{60} dyad geometries with the largest binding energies) were calculated using the constrained DFT formalism[22] at the B3LYP/6-31G(d,p) level using NWChem[23] (version 5.1.1). The continuum solvation "Conductor-like Screening Model"[24] was used to model the solid-state dielectric medium with a dielectric constant (ε) of 3. The effective electronic couplings between the oligomer HOMO and the triply-degenerate C_{60} LUMO were calculated using fragment orbital approach.[25]

5.3. Results and discussion

5.3.1. Molecular geometric properties

Calculations were carried out on a series of oligothiophene structures to investigate the influence of alkyl side-chain number and placement on twisting of the conjugated backbone. The results discussed here are for oligomers with similar conjugation path lengths (12 thiophene rings for each oligomeric structure as shown in **Figure A.5.1**), and the geometric patterns reported are taken from the central portion of the structure so as to mitigate end-group effects. As expected, the differing substitution patterns along the oligothiophene backbone result in rather distinct differences in the (gas phase) degree of twisting. P3HT has a calculated backbone twist of 21°, in agreement with previous results;[26,27] planarizing the system to give the fully planar form (the inferred thin-film structure) results in an energetic destabilization of 3.3 kcal/mol for the 12-ring oligomer (**Figure A.5.2**). The asymmetric nature of the hexyl chain placement on the individual thiophene rings induces slight differences in the carbon-carbon bond lengths (C2-C3 = 1.393 Å, C3-C4 = 1.420 Å, and C4-C5 = 1.383 Å) within the ring, which in turn leads to a slight asymmetry in the bond-length alternation (BLA) pattern within the thiophene ring (0.037 Å and 0.027 Å).

For the two regiorandom P3HT structures considered (**Figure A.5.3**), there is a notable difference in the twist angles, bond lengths, and BLA between the thiophene rings. In particular, the twist angles between the imposed head-to-head defects are larger than 65°, while the other thiophene-thiophene torsions are on the order of 15° - 25°, as in regioregular P3HT. Among the two regio-random P3HT oligomers, RRa2-P3HT is the most energetically stable (by 1.2 kcal/mol).

For PDHTT and PDHBT, two symmetric structural forms of thiophene are present – unsubstituted and di-hexyl substituted. The carbon-carbon bonds in the di-hexyl substituted structure (C2-C3 ≈1.39 Å and C3-C4 ≈1.44 Å) are longer than their unsubstituted counterparts (C2-C3 ≈1.38 Å and C3-C4 ≈1.42 Å), and manifest a slightly larger BLA (≈0.05 Å vs. 0.03 Å). The twists within the PDHTT and PDHBT backbones between the substituted and unsubstituted structures is on the order of 30° − 40° (**Figures A.5.4 and A.5.5**); for PDHTT, the twist between the unsubstituted thiophene rings is 16°. We note that for PDHBT, *syn*- and *anti*- arrangements among the monomer units were investigated – in the case of the *syn*-conformer, the hexyl chains are on opposite sides of the backbone, while in the *anti*-conformer the hexyl chains are on the same side of the backbone; the *syn*-conformation is 1.4 kcal/mol more stable. Overall, calculations suggest that regioregular P3HT has the lowest degree of backbone twisting, while PDHTT, PDHBT, and the regio-random P3HT oligomers are progressively more twisted across the entire length of the oligomer.

To estimate the energy barriers associated with the thiophene-thiophene torsions along the conjugated backbone, torsion energy profiles for four terthiophene derivatives were examined[28] shown in **Figure 5.2**. The thiophene-thiophene twists of the energy-minimized structures for the various terthiophenes are similar to those observed for the full oligomer structures. The energy required to planarize the unsubstituted (3T) and monohexyl-substituted (m-3T) terthiophenes falls well within thermal energy at room temperature (RT, 0.6 kcal/mol); these results are similar to those previously described for bithiophene.[29] Due to the steric interactions induced by the additional alkyl chain, the energetic requirements to planarize the dihexyl-substituted structures are 2.1 - 3.6 kcal/mol. Such energetic differences suggest that the polymers could pack in different manners in the solid state.

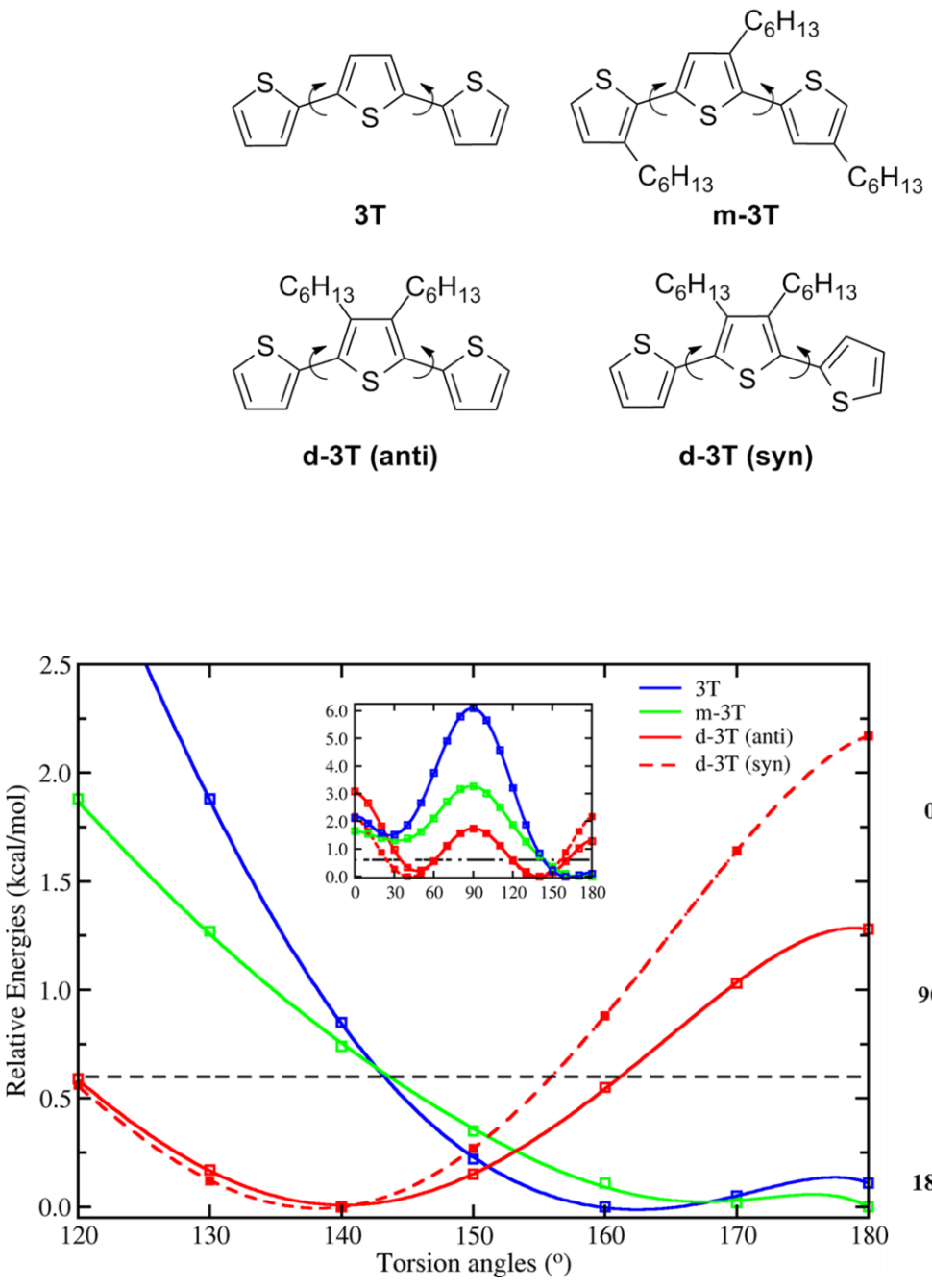

Figure 5.2 (top) Terthiophene chemical structures. (bottom) Thiophene-thiophene torsion potential energy surface for the four terthiophene derivatives as determined at the B3LYP/6-31G(d,p) level of theory. The inset shows the full potential energy surface, while the larger image focuses on the region around the minimum. The figures to the right illustrate the defined torsion angles.

Further, geometrical features of tertbutyl analog of PDHTT (3',4',3"",4"",-tetrabutyl-2,2':5',2":5",2"':5"',2"":5"",2"""-hexathiophene, see **Figures A.5.6 and A.5.7**) was obtained and compared with its crystal structure. Focusing on the central portion of the structure (**Figures A.5.6**), the carbon-carbon bonds in the di-hexyl substituted thiophene (C2-C3 ≈1.39 Å and C3-C4 ≈1.44 Å) are longer than those in the unsubstituted thiophene (C2-C3 ≈1.38 Å and C3-C4 ≈1.41 Å), and manifest a slightly larger BLA (≈0.05 Å vs. 0.03 Å) similar to the crystal structure. In the crystal, the twists between the substituted and unsubstituted thiophenes are on the order of ≈ 20°, while the central twist between the unsubstituted thiophenes is ≈ 0° (as noted above, the energy to planarize unsubstituted thiophenes is smaller than RT). These twist angles, though, are smaller than those calculated for the isolated PDHTT oligomer, but fall in line with expectations of smaller torsions due to intermolecular packing forces in the crystal. The calculated geometric parameters (bond lengths, twist angles) of the butyl-substituted hexamer are (nearly) identical to the hexyl-substituted PDHTT oligomer described above, indicating little-to-no influence imparted by the butyl versus the hexyl side chains. These results provide confidence in the accuracy of the geometric structures predicted by the model oligomers of the full polymer systems. Importantly, the observed twisted backbone demonstrates that the 3,4-dialkyl thiophene unit should induce pronounced twists in the oligomer/polymer chain.

5.3.2. Electronic and optical properties

The frontier molecular orbital energies for the oligomeric structures and solid state IPs are listed in **Table 5.1** (molecular orbital iso-surfaces are present in the ancillary materials). The solid-state IPs were shown to systematically increase with the larger degree of backbone twist from 4.99 eV for P3HT to 5.15 eV, 5.22 eV, and 5.25 eV for PDHTT, PDHBT, and RRa-P3HT, respectively. Calculated HOMO energies vary considerably with the twist angle along the

oligothiophene backbone – ranging from -4.25 eV (P3HT) to -4.81 eV (PDHBT). In general, the polymer CV ionization potentials are consistent with the the HOMO energy trends across the oligomeric series. The π-conjugation is affected with the increase in backbone twisting resulting in stabilized HOMO energies and increased IPs. The LUMOs fall within a narrower energetic range − from -1.81 eV (PDHBT) to -2.11 eV (P3HT); not surprisingly, the HOMO-LUMO gap (Δ_{HL}) increases with increasing twist angle in the P3HT analogs.

Table 5.1 Solid-state IPs, frontier molecular orbital energies and twist angles across the thiophene series determined at the B3LYP/6-31G(d,p) level of theory. Two conformations were examined for all of the polymers except PDHTT. Perspectives of the 3D structure for all of the conformations are shown in Figures A.5.2 – A.5.5.

Polymer	IP (CV) (eV)[a]	HOMO (eV)	LUMO (eV)	Δ_{HL}	Dihedral angle φ(°)
P3HT (twisted)	4.99	-4.43	-1.99	2.44	21
P3HT(planar)		-4.25	-2.11	2.14	0
PDHTT	5.15	-4.71	-2.05	2.66	30, 16
PDHBT (syn)	5.22	-4.81	-1.81	3.00	34
PDHBT (anti)		-4.71	-1.88	2.83	36
RRa-P3HT-1	5.25	-4.75	-1.83	2.92	≈15 − 25, 65
RRa-P3HT-2		-4.59	-1.92	2.67	≈15 − 25, 65

[a] IPs were determined from cyclic voltammetry using the onset of oxidation (E_{ox}^{onset}) of thin films spun from chloroform on platinum electrode in 0.1 M *n*-Bu_4NPF_6−acetonitrile solution and the conversion relationship IP (eV) = e (E_{ox}^{onset} + 4.8).[11]

Introduction of the second hexyl chain and unsubstituted thiophene spacers in PDHTT and PDHBT induces a substantial energetic stabilization of the calculated HOMO energy versus (twisted) P3HT, corresponding with the increased twists within the oligothiopene backbone. However, unlike the P3HT structures, the LUMO energies are only slightly affected by the increased twist within the conjugated backbone, with the direction of the energetic shift differing between the two systems. In PDHBT, the more twisted nature of the oligothiophene backbone causes a slight energetic destabilization (-1.81 eV *syn*, -1.88 eV *anti*), in agreement with the influence of the degree of twisting within the P3HT series. On the other hand, the LUMO of

PDHTT is stabilized (-2.05 eV) versus the twisted P3HT form and is similar to the LUMO energy of the fully planar P3HT (-2.11 eV) structure. This is a consequence of the delocalization of the PDHTT LUMO over the two more planar bithiophene units that neighbor each dialkyl-substituted thiophene.

Table 5.2 provides thin film and solution absorption onsets of the polymers as well as vertical transition energy, transition dipole moment and oscillator strength, and electronic configurations of the lowest-lying excited states of the oligomeric structures determined using TDDFT at B3LYP/6-31G(d,p) level. The $S_0 \rightarrow S_1$ transition energies increase in energy on going from P3HT (twisted 2.10 eV, planar 1.84 eV), to PDHTT (2.28 eV) and PDHBT (2.56 eV *syn*, 2.43 eV *anti*); the $S_0 \rightarrow S_1$ transition energies for the two region-random structures are 2.33 eV (RRa-P3HT-1) and 2.55 eV (RRa-P3HT-2). These results are somewhat different from the solution data, in particular with regard to the slightly larger transition energy of PDHTT *vs.* P3HT and PDHBT *vs.* RRa-P3HT; it is expected that polarization effects and the variety of polymer conformations available in solution, along with the choice of oligomeric structure for the TDDFT calculations (in particular for the region-random P3HT structures), could lead to these modest discrepancies. The $S_0 \rightarrow S_1$ transitions in the oligomers are principally described as being HOMO→LUMO excitations, with very small contributions from a HOMO-1→LUMO+1 excitation. The ordering of the vertical transition energies correspond well with the electronic gap, which are highly influenced by the twisting of the conjugated backbone.

Table 5.2 Thin film and solution absorption onsets and calculated first excited-state vertical transition energies, transition dipole moments, and electronic configurations at the TDDFT B3LYP/6-31G(d,p) level of theory.

	thin film[a]	solution[b]	TDDFT				
Polymer	E_{opt} (eV)	E_{opt} (eV)	Confor-mation	E_{vert} (eV)[e]	μ_{ge} *(D)*	f_{ge}	Electronic configuration
P3HT	1.90	2.23	twisted	2.10	21.35	3.62	HOMO→LUMO (94%); HOMO-1→LUMO+1 (4%)
			planar	1.84	24.00	4.03	HOMO→LUMO (93%); HOMO-1→LUMO+1 (3%)
PDHTT	1.96	2.20		2.28	20.18	3.52	HOMO→LUMO (91%); HOMO-1→LUMO+1 (6%)
PDHBT	2.08	2.22	*syn*	2.56	16.84	2.76	HOMO→LUMO (87%); HOMO-1→LUMO+1 (9%)
			anti	2.43	17.55	2.84	HOMO→LUMO (91%); HOMO-1→LUMO+1 (6%)
RRa-P3HT-1	2.25	2.32		2.33	18.45	3.01	HOMO→LUMO (96%); HOMO-1→LUMO+1 (2%)
RRa-P3HT-2				2.55	17.04	2.81	HOMO→LUMO (92%); HOMO-1→LUMO+1 (4%)

[a] Measured in films spun from chlorobenzene. [b] Measured in solution in chlorobenzene.[11]

5.3.3. Molecular interactions with fullerene

In efforts to get an understanding of the polymer-fullerene interactions, model oligomer:fullerene dyad geometries were investigated. For simplicity, C_{60} was used to represent the fullerene in the hole- and electron-transport material complex. To determine the complex geometry, the pentagonal face of C_{60} was placed parallel to the plane of the central unsubstituted thiophene unit in PDHTT and PDHBT or hexyl-substituted thiophene unit in P3HT. Grimme's dispersion-corrected B97D functional[20] and a 6-31G(d,p) basis set was used to determine the binding energy (with respect to infinite separation distance) of the complex as the oligomer-C_{60} distance was varied from 2.8 Å – 4.4 Å (**Figures A.5.11 – A .5.13**). As presented in **Table 5.4**, the largest binding energy for the complex is calculated to shift to larger oligomer:fullerene

distances with increased twist within the conjugated backbones; across the series, the oligomer:fullerene distances ranged from 3.15 Å to 3.35 Å. Note, for dyad configurations where the fullerene approaches from the side opposite to the alkyl side groups (*inv*),the distances are smaller (3.10 Å).

Packing motifs in the solid state were investigated using grazing incidence X-ray scattering (GIXS) measurements on as-cast and annealed thin films of P3HT, PDHTT, and PDHBT.[11] The polymers that have larger torsional angles along the π-conjugated backbone pack in a more disordered fashion and exhibit a lower degree of crystallinity. This indicates the impact of the alkyl substitutions not only on the polymer molecular properties, but also on the polymer:fullerene interactions at the interfaces.

5.3.4. Effect of configurations on CT state energies, electronic coupling, and correlation to open-circuit voltage

The origin of V_{OC} in organic bulk-heterojunction solar cells has been a subject of interest for some years.[30-33] Sharber *et al*. studied a large number of systems and found a linear dependence of V_{OC} with the polymer IP and thus with the energy difference between IP of the polymer and EA of the fullerene.[32] V_{OC} is also thought to be linearly dependent on the CT state energy.[34-37] CT state at the polymer:fullerene interface is believed to be immediate precursor to free carriers. Further, reduction in dark current and radiative recombination losses have been suggested to bring about improvements in V_{OC}.[7,34,35] The losses through radiative recombination and dark current are thought to be minimal, in a one-electron picture, when the electronic coupling between HOMO of the polymer and the LUMO of fullerene is small.

In order to determine the relation of CT state energy and electronic coupling on open-circuit voltage, oligomer:fullerene CT state energies and effective electronic couplings were

computed based on dyad geometry at largest binding energy. The CT state energies (E_{CT}) were computed using constrained DFT formalism and effective electronic couplings evaluated using fragment orbital approach. The P3HT dyad has the smallest calculated E_{CT}, and it progressively increases for dyads consisting oligomers with larger twist in the conjugated backbone (**Table 5.3**). Considering the dyads with the lowest energy oligomer conformers (P3HT-twisted, PDHTT, PDHBT-syn, and RRa-P3HT-2), there is a strong linear correlation between computed E_{CT} and the device V_{OC} (see **Figure 5.3**).[11]

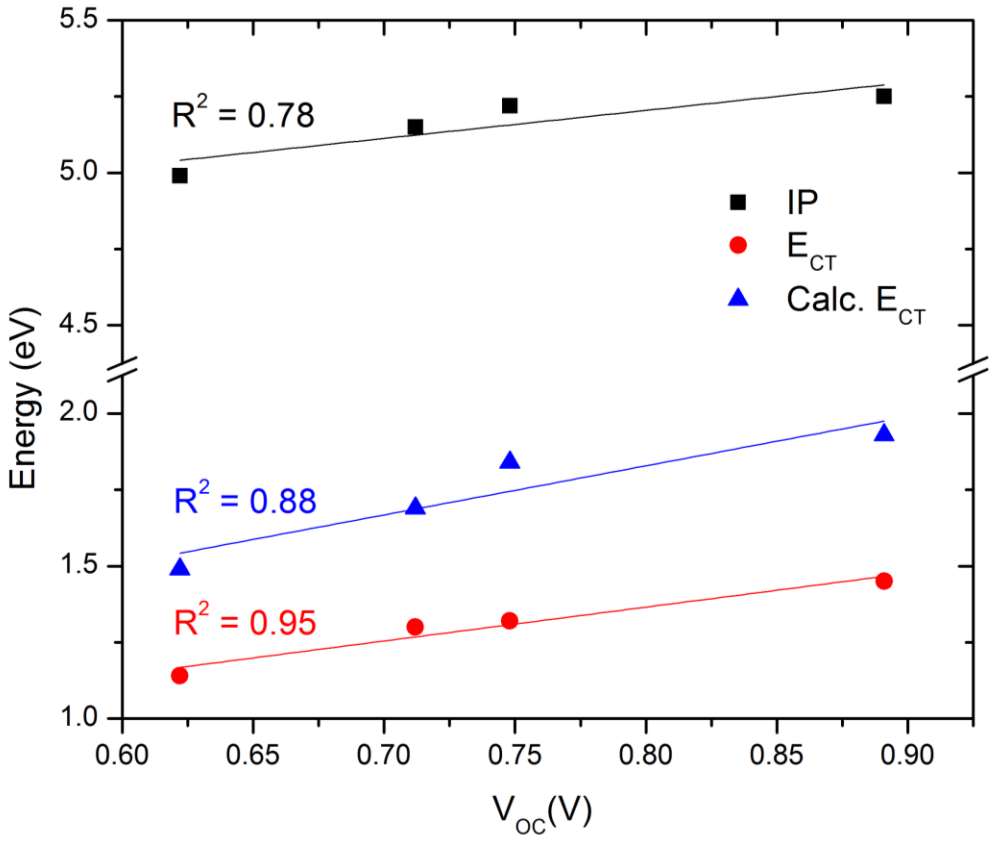

Figure 5.3 Measured ionization potential (IP) and charge-transfer state energy (E_{CT}) and calculated E_{CT} (Calc. E_{CT}) for dyads consisting oligomers with the lowest energy conformation.

Experimentally, the energy of charge-transfer complexes can be determined by measuring the absorption spectra or external quantum efficiency spectra of the polymer:fullerene

blend. Here, the charge-transfer complex energies were measured using photothermal deflection spectroscopy.[11,38,39] The measured E_{CT} show a good correlation with V_{OC} and the polymer IP (**Figure 5.3**) and suggests the improvements in V_{OC} obtained for PDHTT and PDHBT compared to P3HT is mainly a function increase in polymer IP as a result of the increased backbone twist. The V_{OC} is roughly 0.57 eV less than the CT potentials, E_{CT}/q, which is comparable to other polymer:fullerene BHJ devices, whose losses fall in the range of 0.53-0.59 V.[34] The calculated E_{CT} compare well with these measured values and follow a good linear correspondence (R^2 = 0.92) although the calculated values are overestimated by 0.3 – 0.5 eV. The overestimation of the E_{CT} could come from a variety of sources, including differences in the dielectric constants between the HTM and ETM at the interface, the simplicity of taking into account only a two-molecule complex, and the potential for underestimation of the E_{CT} in the EQE measurements.

Table 5.3. Experimental and calculated IPs, E_{CT}, and observed V_{oc} of the solar cell devices.

Polymer	Polymer IP (eV) [a/b]	E_{CT} (eV) [c]	S_1/T_1 E_{CT} (eV) [d]	V_{OC} (V) [e]
P3HT (twisted) *inverted*	4.99/ 4.43	1.14 [f]	1.39/ 1.38	0.622 [f]
P3HT (planar)	4.99/ 4.25	1.14 [f]	1.31/ 1.27	0.622 [f]
P3HT (twisted)	4.99/ 4.43	1.14 [f]	1.49/ 1.44	0.622 [f]
PDHTT	5.15/ 4.71	1.30	1.69/ 1.63	0.712
PDHBT (syn)	5.22/ 4.81	1.32	1.84/ 1.75	0.748
PDHBT (anti)	5.22/ 4.71	1.32	1.80/ 1.70	0.748
RRa-P3HT-1	5.25/ 4.60	1.45	1.65/ 1.59	0.891
RRa-P3HT-1 *inverted*	5.25/ 4.60	1.45	1.52/ 1.52	0.891
RRa-P3HT-2	5.25/ 4.75	1.45	1.93/ 1.75	0.891

IP as determined via [a]cyclic voltammetry or [b]calculated with Koopmans' approximation.[40] [c]E_{CT} measured by fitting the sub-bandgap region of the EQE spectra. [d]E_{CT} calculated using constrained DFT formalism.[22] [e]Average measured V_{OC}. [f]Measured for 225nm thick devices.[11]

To determine if the large V_{OC}'s in the devices made from the more twisted polymers are partly due to a decrease in polymer-fullerene coupling, the effective electronic coupling of the oligomer:fullerene complexes were calculated. As the twist within the oligomer conjugated

backbone increases, the increased distance between the oligomer and C_{60} leads to a reduced electronic coupling between the oligomer and fullerene. Although this correlates well with the increase in V_{OC} with increased twisting in the polymer backbone, the variation in the electronic coupling is quite small and results in an estimated increase in V_{OC} of 16 mV, 28 mV and 19 mV for PDHTT, PDHBT and RRa-P3HT, respectively, compared with P3HT (see **Table 5.4**). These values are roughly one-order of magnitude smaller than the observed increases in V_{OC}. Consequently, the differences in V_{OC} appear primarily attributable to the differences in the polymer IP versus differences in electronic coupling.

Table 5.4 Calculated oligomer-C_{60} distances and the electronic couplings.

Polymer	Donor-acceptor distance (Å)[a]	Electronic coupling *t* (meV)[b]	Δ V_{OC} (meV)[c]
P3HT (twisted)-*inverted*	3.10	66	--
P3HT (twisted)	3.20	54	10
P3HT (planar)	3.15	54	10
PDHTT	3.25	48	16
PDHBT (syn)	3.35	38	28
PDHBT (anti)	3.35	44	21
RRa-P3HT-1	3.20	63	2
RRa-P3HT-1-*inverted*	3.10	80	-10
RRa-P3HT-2	3.70	18	65

[a] Donor (oligomer)-acceptor (C_{60}) separation distance at largest binding energy [b] Effective electronic coupling (*t*)[25] between the oligomer HOMO and the triply-degenerate C_{60} LUMO. [c] Calculated change in open circuit voltage compared to P3HT:PCBM (inverted P3HT conformation) devices due to differences in the effective electronic coupling using Equation 5.1:

$$\Delta V_{OC} = -\frac{2kT}{q}\Delta \ln(t) \tag{5.1}$$

Equation 5.1 results from **Equation 5.2** in particular the second term representing radiative recombination, which was derived by Vandewal et al.[34] Here *h* is Planck's constant, *c* is the speed of light, EQE_{EL} is the electroluminescence quantum efficiency and *f* is proportional to the square of the electronic coupling, *t*.

$$V_{OC} = \frac{E_{CT}}{q} + \frac{kT}{q}\ln\left(\frac{J_{SC}h^3c^2}{fq2\pi(E_{CT}-\lambda)}\right) + \frac{kT}{q}\ln\left(EQE_{EL}\right) \tag{5.2}$$

5.3.5. Solar cell properties and diode hole mobilities.

The photovoltaic properties of P3HT, PDHTT, PDHBT, and RRa-P3HT were investigated in the device structure. The details to the fabrication of devices and experimental measurements can be found elsewhere.[11] The optimized device characteristics are summarized in **Table 5.5**.

Table 5.5 Photovoltaic properties of highest efficiency polymer solar cells blended with $PC_{71}BM$.

Polymer	J_{SC} (mA/cm^2)	V_{OC} (V)	Fill Factor	PCE_{max} (PCE_{avg}) (%)
P3HT	9.57	0.620	0.67	4.00 (3.92)
PDHTT	8.93	0.735	0.64	4.20 (4.01)
PDHBT	5.96	0.745	0.65	2.87 (2.68)
RRa-P3HT	5.99	0.900	0.42	2.27 (2.21)

The PDHTT and PDHBT based solar cells measured V_{OC}'s that are 0.1 V larger than P3HT based solar cells. These improvements in V_{OC} can be primarily attributable to the larger IP of the two polymers, a direct consequence of the increased twist in the conjugated backbone. Compared to P3HT based devices, the PDHTT devices have a slightly smaller J_{SC}. This results from the larger optical gap in PDHTT. Both PDHTT and P3HT devices showed similar fill factors. Based on these parameters, a slight improvement in PCE was observed for PDHTT (4.20% versus 4.00% for P3HT). The more twisted PDHBT and RRa-P3HT devices showed J_{SC}'s that are significantly smaller compared to P3HT and PDHTT based devices. This is a consequence of the larger optical gaps and lower external quantum efficiencies (see **Figure A.5.14**).

To investigate the impact from different geometric structures on the hole mobilities, space-charge-limited current measurements were taken on hole-only diodes of the

polymer:fullerene blends in polymer:fullerene blends.[41] As summarized in **Table A.5.3**, the hole mobility of the PDHTT blend is similar to that of P3HT, while the more twisted backbones of PDHBT and RRa-P3HT result in hole mobilities that are 5 and 10 times smaller, respectively. These results highlight the importance of the complex optimization problem in OPV devices.

5.4. Conclusions

Polythiophene derivatives are extensively used as hole-transport materials in organic photovoltaic applications. In this Chapter, we have provided details on the influence of placement and density of side chains on the geometric and electronic properties of alkyl substituted oligothiophenes and their interactions with fullerene. We have then related the differences in their properties to the performance characteristics of devices where these materials appear in the photoactive layer.

Polymers PDHTT and PDHBT contain dialkyl substitutents on the 3 and 4 positions of the thiophene with bi- and mono-thiophene spacers, respectively. The values of ionization potential measured initially (from photoelectron spectroscopy of films in air) for these systems were found to be very similar to that for P3HT (5.04 – 5.07 eV). The 0.1 V increase in measured V_{OC} for PDHTT and PDHBT-based devices (compared to P3HT-based devices) was therefore initially thought to originate mainly from weaker electronic couplings at the HTM:ETM interface that could lead to reduced dark current.

Our calculations, however, indicated that the PDHTT and PDHBT ionization potentials were substantially larger (0.3 – 0.4 eV) than that for P3HT, as a result of the increased backbone twisting in dialkyl-substituted polymers. Additionally, the changes in V_{OC} that would be estimated to first approximation on the basis of the differences in electronic couplings for charge recombination (see **Equation 5.1**) were an order of magnitude smaller than the changes in

measured V_{OC}. These computational results lead to subsequent remeasurements of the ionization potentials. The results from these new measurements were found to be fully consistent with the trends in the computed values. *Ceteris paribus*, the increase in V_{OC}, therefore, could be primarily correlated with the increase in the polymer ionization potential.

Furthermore, a good linear correlation was found between the computed charge-transfer state energies (E_{CT}) and the measured E_{CT}. This provides confidence in the use of our computational methodology in evaluating E_{CT} for thiophene based π-conjugated systems.

5.5. References

(1) http://www.heliatek.com/newscenter/latest_news/neuer-weltrekord-fur-organische-solarzellen-heliatek-behauptet-sich-mit-12-zelleffizienz-als-technologiefuhrer/?lang=en (accessed January 2013)

(2) He, Z.; Zhong, C.; Su, S.; Xu, M.; Wu, H.; Cao, Y. *Nat. Photonics* **2012**, *6*, 591.

(3) Service, R. F. *Science* **2011**, *332*, 293.

(4) R. Andersson, M.; Thomas, O.; Mammo, W.; Svensson, M.; Theander, M.; Inganas, O. *J. Mater. Chem.* **1999**, *9*, 1933.

(5) Zou, Y.; Sang, G.; Wu, W.; Liu, Y.; Li, Y. *Synth. Met.* **2009**, *159*, 182.

(6) Li, Y.; Xue, L.; Xia, H.; Xu, B.; Wen, S.; Tian, W. *J. Polym. Sci., Part A: Polym. Chem.* **2008**, *46*, 3970.

(7) Perez, M. D.; Borek, C.; Forrest, S. R.; Thompson, M. E. *J. Am. Chem. Soc.* **2009**, *131*, 9281.

(8) Bredas, J. L.; Street, G. B.; Themans, B.; Andre, J. M. *J. Chem. Phys.* **1985**, *83*, 1323.

(9) Bredas, J. L.; Heeger, A. J. *Macromolecules* **1990**, *23*, 1150.

(10) Hernandez, V.; Navarrete, J. T. L. *J. Chem. Phys.* **1994**, *101*, 1369.

(11) Ko, S.; Hoke, E. T.; Pandey, L.; Hong, S.; Mondal, R.; Risko, C.; Yi, Y.; Noriega, R.; McGehee, M. D.; Brédas, J.-L.; Salleo, A.; Bao, Z. *J. Am. Chem. Soc.* **2012**, *134*, 5222.

(12) Ko, S.; Verploegen, E.; Hong, S.; Mondal, R.; Hoke, E. T.; Toney, M. F.; McGehee, M. D.; Bao, Z. *J. Am. Chem. Soc.* **2011**, *133*, 16722.

(13) Belletete, M.; Mazerolle, L.; Desrosiers, N.; Leclerc, M.; Durocher, G. *Macromolecules* **1995**, *28*, 8587.

(14) Kokubo, H.; Sato, T.; Yamamoto, T. *Macromolecules* **2006**, *39*, 3959.

(15) Becke, A. D. *J. Chem. Phys.* **1993**, *98*, 5648.

(16) Lee, C.; Yang, W.; Parr, R. G. *Phys. Rev. B* **1988**, *37*, 785.

(17) Stephens, P. J.; Devlin, F. J.; Chabalowski, C. F.; Frisch, M. J. *J. Phys. Chem.* **1994**, *98*, 11623.

(18) Hariharan, P. C.; Pople, J. A. *Theor. Chim. Acta* **1973**, *28*, 213.

(19) Francl, M. M.; Pietro, W. J.; Hehre, W. J.; Binkley, J. S.; Gordon, M. S.; Defrees, D. J.; Pople, J. A. *J. Chem. Phys.* **1982**, *77*, 3654.

(20) Grimme, S. *J. Comput. Chem.* **2006**, *27*, 1787.

(21) Frisch, M. J. T., G. W.; Schlegel, H. B.; Scuseria, G. E.; Robb, M. A.; Cheeseman, J. R.; Scalmani, G.; Barone, V.; Mennucci, B.; Petersson, G. A.; Nakatsuji, H.; Caricato, M.; Li, X.; Hratchian, H. P.; Izmaylov, A. F.; Bloino, J.; Zheng, G.; Sonnenberg, J. L.; Hada, M.; Ehara, M.; Toyota, K.; Fukuda, R.; Hasegawa, J.; Ishida, M.; Nakajima, T.; Honda, Y.; Kitao, O.; Nakai, H.; Vreven, T.; Montgomery, Jr., J. A.; Peralta, J. E.; Ogliaro, F.; Bearpark, M.; Heyd, J. J.; Brothers, E.; Kudin, K. N.; Staroverov, V. N.; Kobayashi, R.; Normand, J.; Raghavachari, K.; Rendell, A.; Burant, J. C.; Iyengar, S. S.; Tomasi, J.; Cossi, M.; Rega, N.; Millam, N. J.; Klene, M.; Knox, J. E.; Cross, J. B.; Bakken, V.; Adamo, C.; Jaramillo, J.; Gomperts, R.; Stratmann, R. E.; Yazyev, O.; Austin, A. J.; Cammi, R.; Pomelli, C.; Ochterski, J. W.; Martin, R. L.; Morokuma, K.; Zakrzewski, V. G.; Voth, G. A.; Salvador, P.; Dannenberg, J. J.; Dapprich, S.; Daniels, A. D.; Farkas, Ö.; Foresman, J. B.; Ortiz, J. V.; Cioslowski, J.; Fox, D. J. *Gaussian Inc., Wallingford CT* **2009**.

(22) Wu, Q.; Van Voorhis, T. *Phys. Rev. A* **2005**, *72*, 024502.

(23) Bylaska, E. J.; de Jong, W. A.; Govind, N.; Kowalski, K.; Straatsma, T. P.; Valiev, M.; Wang, D.; Apra, E.; Windus, T. L.; Hammond, J.; Autschbach, J.; Nichols, P.; Hirata, S.; Hackler, M. T.; Zhao, Y.; Fan, P.-D.; Harrison, R. J.; Dupuis, M.; Smith, D. M. A.; Nieplocha, J.; Tipparaju, V.; Krishnan, M.; Vazquez-Mayagoitia, A.; Wu, Q.; Van Voorhis, T.; Auer, A. A.; Nooijen, M.; Crosby, L. D.; Brown, E.; Cisneros, G.; Fann, G. I.; Fruchtl, H.; Garza, J.; Hirao, K.; Kendall, R.; Nichols, J. A.; Tsemekhman, K.; Wolinski, K.; Anchell, J.; Bernholdt, D.; Borowski, P.; Clark, T.; Clerc, D.; Dachsel, H.; Deegan, M.; Dyall, K.; Elwood, E.; Glendening, E.; Gutowski, M.; Hess, A.; Jaffe, J.; Johnson, B.; Ju, J.; Kobayashi, R.; Kutteh, R.; Lin, Z.; Littlefield, R.; Long, X.; Meng, B.; Nakajima, T.; Niu, S.; Pollack, L.; Rosing, M.; Sandrone, G.; Stave, M.; Taylor, H.; Thomas, G.; van Lenthe, J.; Wong, A.; Zhang, Z. *Pacific Northwest National Laboratory, Richland, Washington 99352-0999, USA.* **2008**.

(24) Klamt, A.; Schuurmann, G. *J. Chem. Soc., Perkin Trans. 2* **1993**, *2*, 799.

(25) Valeev, E. F.; Coropceanu, V.; da Silva Filho, D. A.; Salman, S.; Brédas, J.-L. *J. Am. Chem. Soc.* **2006**, *128*, 9882.

(26) DeLongchamp, D. M.; Kline, R. J.; Lin, E. K.; Fischer, D. A.; Richter, L. J.; Lucas, L. A.; Heeney, M.; McCulloch, I.; Northrup, J. E. *Adv. Mater.* **2007**, *19*, 833.

(27) Northrup, J. E. *Phys. Rev. B* **2007**, *76*, 245202.

(28) For the m-3T structure, an additional torsional constraint was employed for the dihedral angle between the thiophene ring and side chain to keep the side-chains in a similar position as the P3HT oligomer.

(29) Raos, G.; Famulari, A.; Marcon, V. *Chem. Phys. Lett.* **2003**, *379*, 364.

(30) Brabec, C. J.; Cravino, A.; Meissner, D.; Sariciftci, N. S.; Fromherz, T.; Rispens, M. T.; Sanchez, L.; Hummelen, J. C. *Adv. Funct. Mater.* **2001**, *11*, 374.

(31) Ramsdale, C. M.; Barker, J. A.; Arias, A. C.; MacKenzie, J. D.; Friend, R. H.; Greenham, N. C. *J. Appl. Phys.* **2002**, *92*, 4266.

(32) Scharber, M. C.; Mühlbacher, D.; Koppe, M.; Denk, P.; Waldauf, C.; Heeger, A. J.; Brabec, C. J. *Adv. Mater.* **2006**, *18*, 789.

(33) Rand, B. P.; Burk, D. P.; Forrest, S. R. *Phys. Rev. B* **2007**, *75*, 115327.

(34) Vandewal, K.; Tvingstedt, K.; Gadisa, A.; Inganas, O.; Manca, J. V. *Phys. Rev. B: Condens. Matter* **2010**, *81*, 125204.

(35) Vandewal, K.; Tvingstedt, K.; Gadisa, A.; Inganas, O.; Manca, J. V. *Nat. Mater.* **2009**, *8*, 904.

(36) Deibel, C.; Strobel, T.; Dyakonov, V. *Adv. Mater.* **2010**, *22*, 4097.

(37) Veldman, D.; Meskers, S. C. J.; Janssen, R. A. J. *Adv. Funct. Mater.* **2009**, *19*, 1939.

(38) Goris, L.; Poruba, A.; Hod'akova, L.; Vanecek, M.; Haenen, K.; Nesladek, M.; Wagner, P.; Vanderzande, D.; Schepper, L. D.; Manca, J. V. *Appl. Phys. Lett.* **2006**, *88*, 052113.

(39) Holcombe, T. W.; Norton, J. E.; Rivnay, J.; Woo, C. H.; Goris, L.; Piliego, C.; Griffini, G.; Sellinger, A.; Brédas, J.-L.; Salleo, A.; Fréchet, J. M. J. *J. Am. Chem. Soc.* **2011**, *133*, 12106.

(40) Koopmans, T. *Physica* **1934**, *1*, 104.

(41) Goh, C.; Kline, R. J.; McGehee, M. D.; Kadnikova, E. N.; Frechet, J. M. J. *Appl. Phys. Lett.* **2005**, *86*, 122110.

CHAPTER 6

EXCITON-DISSOCIATION AND CHARGE-RECOMBINATION PROCESSES IN ORGANIC SOLAR CELLS USING DONOR-ACCEPTOR COPOLYMERS: AN OLIGOMER:FULLERENE COMPLEX STUDY ON THE EFFECTS OF CONFIGURATION ORIENTATION AND THE REORGANIZATION ENERGY

Chapters 3 and 4 discussed molecular properties of π-conjugated systems in isolation. Chapter 5 involved discussion of how side-chain placements can affect these molecular properties and also their interactions with fullerenes. This chapter takes the oligomer:fullerene study to the next step and discusses the role of configuration and reorganization energy on exciton-dissociation and charge-recombinations processes.

6.1. Introduction

The mechanism of the exciton-dissociation process in organic solar cells is a widely debated topic with no consensus on its basic physics that potentially varies with materials used and the photoactive layer structure. Some experiments show that the CT state is formed on electron transfer from HTM to ETM following the diffusion of Frenkel excitons (generated in the HTM) to the interface.[1] Others indicate the formation of CT state on hole transfer from ETM to HTM following Föster energy transfer from HTM to ETM (upon exciton generation at the HTM).[2] Under strongly intermixed condition of the photoactive layer – where the HTM and ETM are in close proximity to one another, for instance, from intercalation of fullerene

molecules in between the polymer side-chains – excitons have been shown to readily dissociate within 100 fs.[3] Photocurrent generation can also involve dissociation of excitons created at the ETM; however, dissociation of these excitons is understood to be fairly inefficient.[4,5] The charge-separation (CS) process that results in generation of free charge carriers also involves several pathways. Besides the commonly referred route through the lowest CT state, there have been evidences of the involvement of higher lying "hot" CT states in the CS process.[5-8] The CS process competes with (geminate) charge-recombination (CR) where the CT state relaxes back to the ground state. This latter mechanism is a potential loss mechanism and has to be minimized.

Poly(3-alkylthiophene) and DA based materials are extensively studied HTMs; and in conjunction with C_{60} or C_{70} based ETMs, have been used to fabricate bulk heterojunction devices.[6,9-18] Theoretical studies of exciton-dissociation and charge-recombination processes for model systems comprising phthalocyanine and perylene bisimide,[19] pentacene and C_{60},[20] sexithiophene and C_{60}/perylenetetracarboxydiimide,[21] poly(3-alkylthiophene (P3HT) and [6,6]-phenyl C_{61} butyric acid methyl-ester ($PC_{61}BM$)[22] and several others have been published recently.[23-26] Here we investigate the role of configuration and reorganization energy on the exciton-dissociation and charge-recombination processes for several DA copolymers in combination with substituted fullerenes that have been used in high-performance organic solar cells. We do so through an oligomer:fullerene dyad approach to understand the impact of the configurations on intermolecular interactions and energetics and ultimately the kinetics of the exciton-dissociation and charge-recombination processes.

6.2. Methodology

The HTMs chosen for this study (**Figure 6.1**) are some of the best performing photoactive materials used in organic solar cells.[11-15] The molecular properties of these systems

have been investigated previously using quantum chemical methods.[27,28] To ensure that the molecular and dyad properties are representative of the polymers, the oligomer size considered was four repeat units as done previously.[22] The fullerene chosen is [6,6]-phenyl C_{71} butyric acid methyl-ester ($PC_{71}BM$) that has been used extensively in polymer:fullerene solar cells.

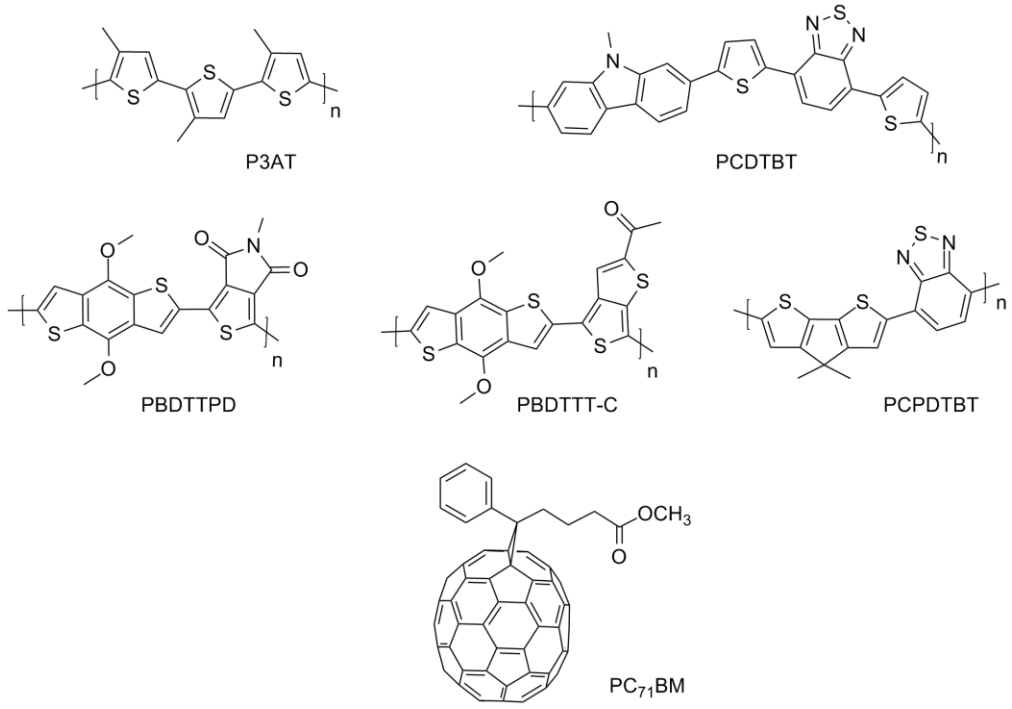

Figure 6.1 Chemical structures of the oligomers and fullerene considered in this work. The abbreviations (that are commonly used in the OPV literature) stand for: P3AT ≡ poly(3-methylthiophene); PCDTBT[12] ≡ poly[N-alkyl-2,7-carbazole-*alt*-5,5-(4′,7′-di-2-thienyl-2′,1′,3′-benzothiadiazole); PBDTTPD[13] ≡ poly[4,8-bis-alkyloxy-benzo[1,2-*b*:4,5-*b′*]dithiophene-2,6-diyl-N-alkylthieno[3,4-*c*]pyrrole-4,6-dione-1,2,diyl]; PBDTTT-C[14] ≡ poly[4,8-bis-alkyloxy-benzo[1,2-*b*:4,5-*b′*]dithiophene-2,6-diyl-*alt*-4-(alkyl-1-one)thieno[3,4-*b*]thiophene-2,6-diyl]; PCPDTBT[15] ≡ poly[2,6-(4,4-bis-alkyl-4*H*-cyclopenta[2,1-*b*;3,4-*b′*]dithiophene)-alt-4,7-(2,1,3-benzothiadiazole)]; and PC71BM ≡ [6,6]-phenyl C_{71} butyric acid methyl-ester.

With a view to model the possible HTM:ETM interfacial configurations in device settings, the starting geometries for the oligomer:fullerene dyads were arranged with the fullerene either on top (*t*, face-on) or on the side (*s*) of the oligomer. Further, the fullerene was

selectively placed next to the electron-donating (don) or electron-accepting (acp) fragment of the oligomer as shown in **Figure 6.2**. The names of the dyads are represented as a way to reveal these configurations and placements. For example, PCDTBT-*s*-acp-td represents $PC_{71}BM$ placed on the side and next to the thiadiazole end of the acceptor fragment benzothiadiazole in the oligomer PCDTBT (Note that for P3AT, the fullerene is placed either directly on top of the thiophene or the midway of the C-C bond connecting two methylthiophene units). To mitigate the end group effects, the fullerene is placed in the central portion of the tetramer.

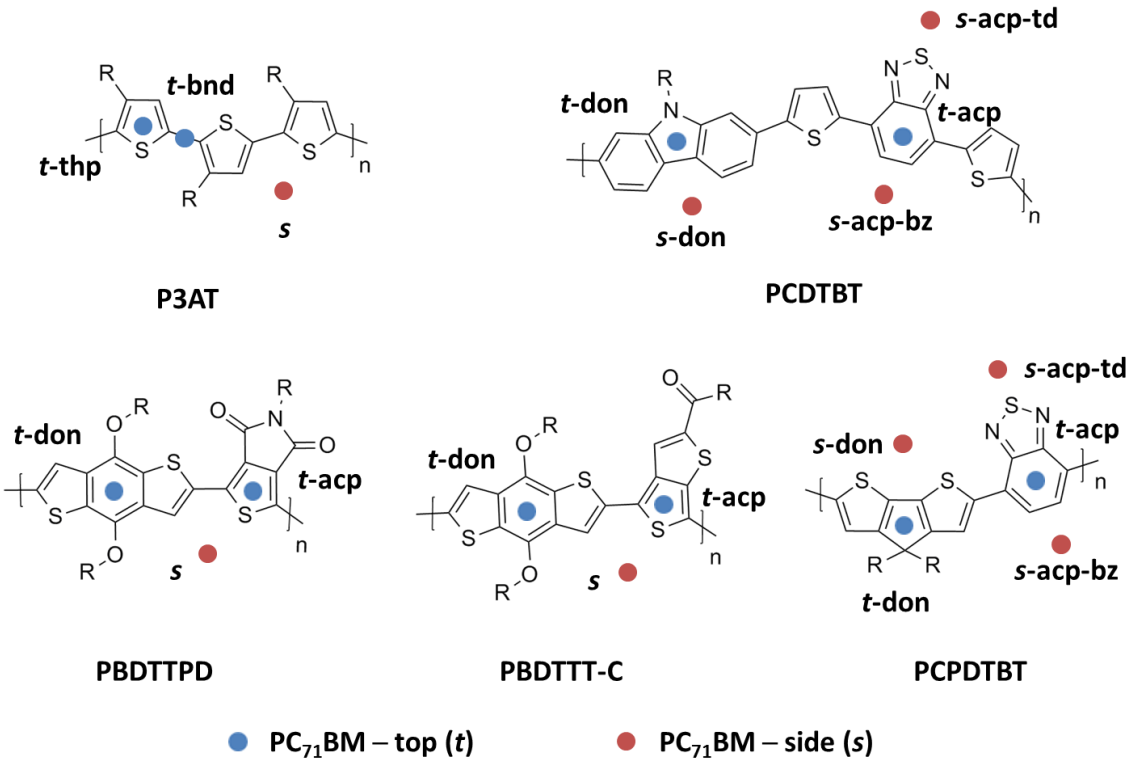

Figure 6.2 Illustration of select configurations of the oligomer:fullerene dyads.

The oligomer:fullerene dyad geometries were obtained through self-consistent charge (SCC)[29] geometry optimization using DFTB+ code[30] with mio-0-1 based Slater-Koster parameters.[29,31] An empirically-corrected van der Waals interaction parameter based on Slater-Kirkwood polarizable atomic model[32] was used for the DFTB based calculations. Based on these

geometries, the CT state energies (E_{CT}) of the dyads were evaluated using the constrained DFT formalism[33] at the B3LYP[34-36]/6-31G(d,p)[37,38] level using NWChem[39] (version 6.1). The continuum solvation "Conductor-like Screening Model"[40] was used to model the solid-state dielectric medium with a dielectric constant (ε) of 3. The evaluation of the dyad E_{CT} was carried out using this method based on the (excellent) correlation with the experimental values (as presented in Chapter 5).[41] Several nonadiabatic-state approaches are available to compute the electronic couplings between the relevant states involved.[20,45-47] However, as a first step, we have undertaken the simple one-electron approximation to compute the couplings relevant to these processes. We computed the effective couplings between the oligomer HOMO (and LUMO) and the nearly degenerate LUMO and LUMO+1 of $PC_{71}BM$ using fragment orbital approach.[42] The local excited state energies (E_{LOC}) were approximated from TDDFT vertical excited state energies of the oligomers at their ground-state dyad geometries. The effective electronic couplings and vertical excitation energies were computed using tuned range-separation parameters at the ωB97[43]/6-31G(d,p) level (ω for P3AT dyads = 0.126 $bohr^{-1}$, ω for DA dyads used as listed in Chapter 4).

Exciton-dissociation and charge-recombination rates were estimated using Marcus semi-classical model[44,45] as previously employed:[20,21,46]

$$k_{if} = J_{if}^2 \sqrt{\frac{\pi}{\lambda k_B T \hbar^2}} \exp\left[\frac{-(\Delta G^0 + \lambda)^2}{4\lambda k_B T}\right] \qquad (6.1)$$

where J_{if} represents electronic coupling between the initial and final states involved in the electron-transfer reaction; ΔG^0 the Gibbs free energy; T is the temperature (set to 300 K); k_B and $\hbar$ the Boltzmann and reduced Planck constants, respectively, and λ the reorganization energy.

The electronic coupling between two states reflects the strength of electronic interaction between the states involved. The J_{if} for CT process involve the local / molecular excited state and CT state and for the CR process, the CT state and ground state (see **Figure 1.2**). Several nonadiabatic-state approaches have been described to compute these electronic couplings.[20,46-48] Here, for simplicity, the J_{if} for the CT and CR processes are estimated using a one-electron picture where the coupling between the LUMOs of the hole- and electron-transport materials, J_{LL} relates to the CT process while the coupling between HOMO and LUMO of hole- and electron-transport materials J_{HL} relates to the CR process.

The λ constitutes both the internal and external contributions. The internal (intramolecular) contribution, λ_i accounts for the changes in geometry of the hole- and electron-transport materials as a result of the charge-transfer whereas the external contribution, λ_e accounts for the electronic and nuclear polarization of the surrounding medium. The λ_i can be computed using adiabatic potential surfaces of the molecular states involved in the electron-transfer reaction. From the adiabatic potential surface approach, for example, λ_i for the charge-transfer reaction can be expressed as the sum of relaxation energies of the charged (HTM^+ or ETM^-) states. Similarly, λ_i for charge recombination can be written as the sum of relaxation energies of the HTM and ETM ionic ground-state geometries to their neutral ground-state geometries. There are only a few methodologies currently available to compute λ_e [49,50] and their applications are rather limited to single organic semiconductor crystals. Because of the lack of straightforward models to compute λ_e, we compute the charge-transfer and charge-recombination rates for a range of reasonable λ (0.25 – 0.75 eV). Given that λ_i for the systems

investigated here range from 0.15 to 0.35 eV, the remaining can be thought of as a contribution from λ_e.

6.3. Results and discussion

The goal of this Chapter is to analyze how the interfacial geometries of the HTM:ETM dyads affect the rates of exciton dissociation and charge recombination relevant to organic solar cells. Note that here we investigate only the first (charge transfer) part of the two step exciton-dissociation process (of which charge-separation is the second). Before we discuss how the parameters that enter the Marcus rate equation (**Equation 6.1**) vary with positions and configurations, we begin with the impact of configurations on the oligomer:fullerene binding energies.

6.3.1. Molecular interactions with fullerene

As noted above the oligomer:fullerene starting geometries were based on select positions and configurations. The select side positions were chosen such that the fullerene avoids head-on steric interactions with methyl side chains in the oligomer. The dyad geometries were then optimized using the DFTB scheme described above. The binding energies with respect to infinite separation of the fullerene and oligomers (at these geometries) for various positions and configurations are presented in **Table 6.1**. The binding energies are based on Grimme's B97D functional[51] coupled to a 6-31G(d,p) basis. This methodology has been shown to perform reasonably well for binding energies.[52,53] The oligomer fullerene binding energies range from -2.8 to -18.4 kcal/mole. As can be expected intuitively, the *t* configurations generally have stronger binding compared to *s* configurations. This can be attributed to the π-π interactions and larger number of sites available for van der Waals interaction between the oligomer and fullerene

in the face-on *t* configuration. Similar observations with stronger binding for pentacene and C_{60} when the pentacene face is parallel to the C_{60} have been reported.[54] Within the *t* or *s* configurations, the binding energies for varying positional arrangements vary substantially for *s* (1.8 – 8.9 kcal/mol) and moderately (0.2 – 1.5 kcal/mol) for *t* configurations

6.3.2. Effect of configurations on electronic couplings

As expressed in **Equation 6.1**, the CT and CR rates have square dependence on the electronic coupling between the involved states. For instance, the CT rate is dependent on the electronic coupling between the (intramolecular) excited state of the oligomer and the CT state. For CR, the two states involved are the CT state and the oligomer ground state. For simplicity, we have approximated the two reaction pathways using the one-electron picture as mentioned above.

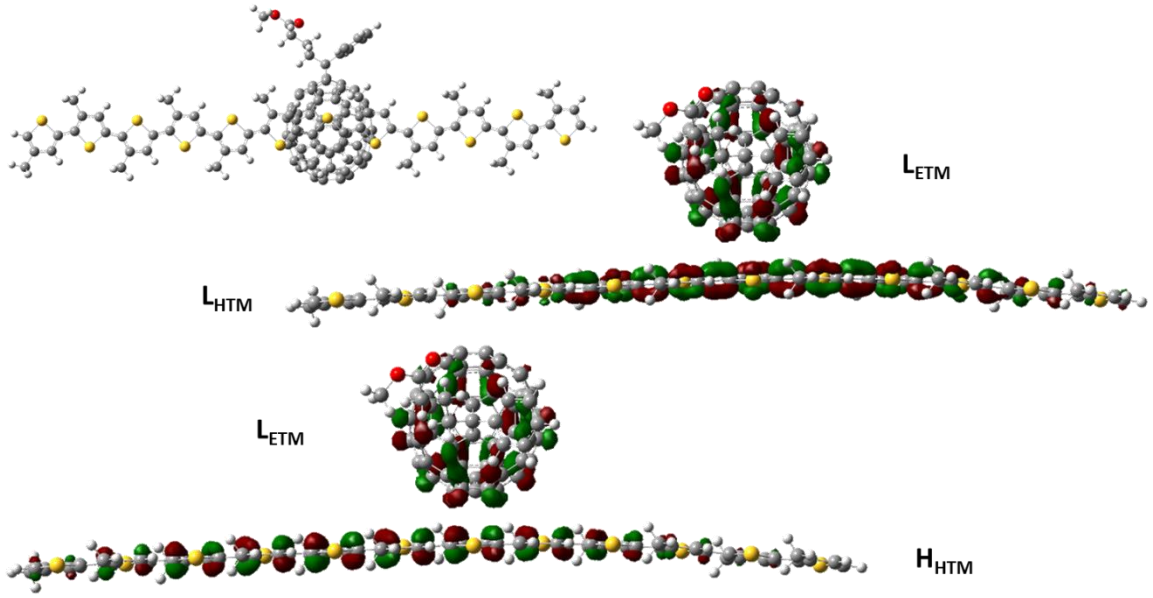

Figure 6.3 Pictorial representation that qualitatively illustrates larger possibility of H_{HTM}:L_{ETM} electronic coupling compared to L_{HTM}:L_{ETM} for P3AT-*t*-thp. Note alignment of like phases for H_{HTM}:L_{ETM} interaction. Calculations performed at the ωB97/6-31G(d,p) level; see methodology above for ω value used.

The calculated electronic couplings for the two electron-transfer reactions are presented in **Table 6.1**. The magnitude of the electronic couplings is understood to be affected by molecular orientations, intermolecular distances and the symmetry of the relevant molecular orbitals.[19-21,55] Here, the effective electronic couplings for the two processes largely vary with positions, configurations, and systems. Consistent with smaller electronic couplings calculated for perpendicular (vs. parallel) configurations for Pentacene:C_{60} complexes,[20] the *s* configurations have minimal electronic couplings, a result of the reduced spatial overlap between molecular orbitals in this configuration (see **Figure 6.4**). The absolute values for J_{HL} are generally larger than J_{LL} for *t* configurations (see **Figure 6.3** as an example) and are affected by the distribution and phase of the relevant molecular orbitals. These results are consistent with the couplings reported for sexithiophene:C_{60} complexes in that, based on the dyad configurations, the coupling of the CT state to the ground state can be stronger than one to the lowest excited state.[21] The absolute J_{HL} values vary by some 10 – 100 meV with respect to positional variation (fullerene next to donor or acceptor fragment in the oligomer) for the *t* configurations. It is difficult to comment on the J_{LL} and J_{HL} values for the *s* and J_{LL} values for the *t* configurations as they are all very small.

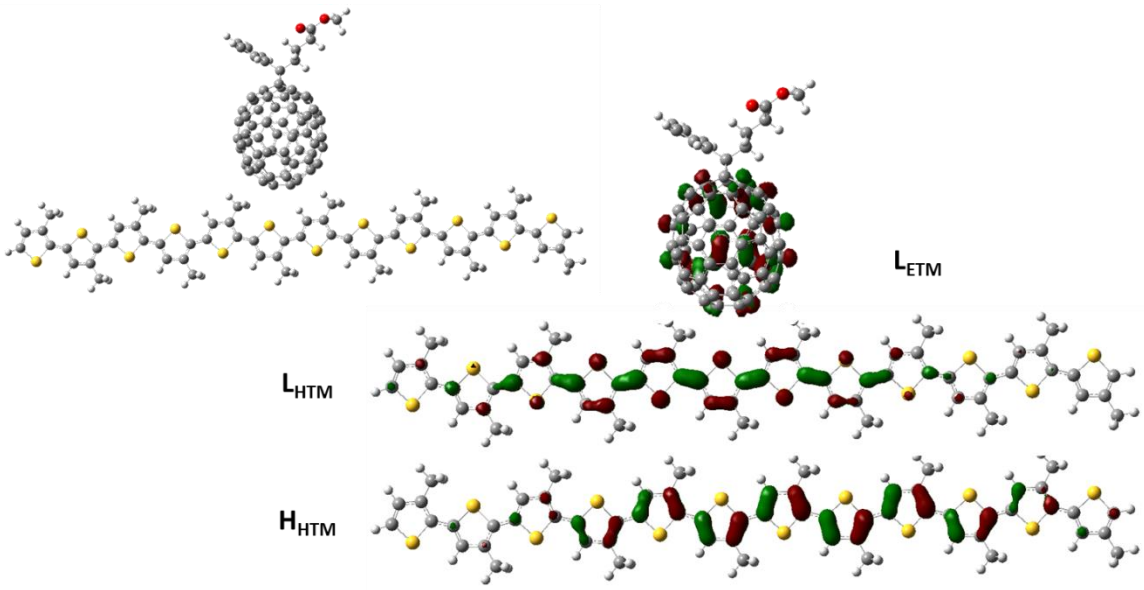

Figure 6.4 Pictorial representation that qualitatively illustrates minimal H_{HTM}:L_{ETM} or L_{HTM}:L_{ETM} electronic coupling (from minimal spatial overlap due to the configuration) for P3AT-*s*. Calculations performed at the ωB97/6-31G(d,p) level; see methodology above for ω value used.

6.3.3. Effect of configurations on charge-transfer energies and enthalpy of reaction

ΔG^0 plays crucial role in the CT and CR rates and as expressed in **Equation 6.1**, it goes (along with λ) into the exponential part of the rate equation. Considering these two processes are spontaneous (negative ΔG^0) for a working solar cell, the square dependence of the exponential term ($\Delta G^0 + \lambda$) implies that the rate reaches a peak (maximum value) when $|\Delta G^0|$ equals λ (since λ is positive). As a function of λ, the rate decreases on either side of the peak when $|\Delta G^0| < \lambda$ or $|\Delta G^0| > \lambda$, also referred as the Marcus normal and inverted regions, respectively.

If the entropy contributions are ignored, ΔG^0 is equal to the reaction enthalpy. In the simplest terms, the CT process can be thought of as the transition from the lowest excited state of

the oligomer (local excited state) to the charge-transfer state. Similarly, the charge-recombination process is the transition between the charge-transfer state and the molecular ground states. The reaction enthalpy for CT process is therefore the difference between E_{CT} and E_{LOC}. For CR, the reaction enthalpy is simply $-E_{CT}$.

The E_{LOC} and E_{CT} for the oligomers and dyads are listed in **Table 6.1**. The E_{LOC} were approximated from the lowest vertical excited states of the isolated oligomers at the dyad geometry at the TDDFT level. E_{CT} can be computed from the sum of ionization potential of the HTM, electron affinity of the ETM, and the attractive Coulomb interaction energy between the charged states (HTM^+ and ETM^-).[19-21] For our purposes, the E_{CT} were computed using the constrained DFT formalism on the dyad geometries with a net positive charge on the oligomer and a negative charge on the fullerene. For the systems considered, the effect of positions and configurations on E_{LOC} is minimal. However, the effect is significant for E_{CT}, with the absolute change in E_{CT} ranging 0.03 – 0.35 eV and 0.07 – 0.37 eV with respect to changes in positions along the backbone and *t* or *s* configurations, respectively.

As reaction rates are sensitive to the magnitude of the driving force ΔG^0 (reaction enthalpy, ΔE for our purposes), we have adjusted the E_{CT} to (adjusted E_{CT} = E_{CT} – 0.44 eV) correct for the overestimation of E_{CT} from CDFT. The adjustment figure of 0.44 eV was based on average overestimation of CDFT E_{CT} compared to experimental E_{CT} measured for four different systems using photothermal deflection spectroscopy (see **Figure 5.3**).[41] The adjusted E_{CT} values are listed in **Table 6.1** and are used for calculating reaction enthalpies and subsequently reaction rates.

The reaction enthalpies ΔE_{CT} and ΔE_{CR} for charge-transfer and charge-recombination processes vary significantly with respect to positions and configurations and between systems

(consequence of changing E_{CT}). The ΔE_{CT} for most systems and configurations are negative (exothermic reaction) and range from -0.06 to -0.82 eV with P3AT having the largest reaction enthalpies. Note that there are a few systems where the values for ΔE_{CT} is zero or positive. As expected, the ΔE_{CR} values are exothermic and range from -1.03 to -1.93 eV, with dyads that include the oligomer PDBTTPD having the most negative charge-recombination enthalpies.

6.3.4. Effect of configurations on charge-transfer and charge-recombination rates

Based on the electronic couplings, driving forces, and reorganization energies discussed above, the CT and CR rates were calculated using **Equation 6.1** and are presented in **Table 6.1** and **Figure 6.5** and **A.6.1**. It has to be noted that the accuracy of the rates that are calculated are inherently limited by the approximations made in determining these parameters.

Considering the reorganization to be 0.25 eV, the rates vary by up to three orders of magnitude (ignoring rates < 1 s^{-1}) with respect to varying configurations and positions. The CT rates k_{CT} are at least five orders of magnitude larger than charge-recombination rates k_{CR} indicating that the charge-transfer process is a much faster process. The CT rates are the slowest and CR rates the fastest for dyads constituting oligomer P3AT. This is a consequence of ΔE_{CT} being the farthest away and ΔE_{CR} being the closest to the reorganization energy when compared to these values for other oligomers. The CT rates for the other dyads range over 10^8 to 10^{13} s^{-1} while the CR rates, in general, are practically insignificant (< 10^{-4} s^{-1}). It is interesting to note that although there are a few systems (PBDTTPD-*t*-don and PCPDTBT-*s*-don, for instance) that have endothermic ΔE_{CT}, the CT rates reach 10^9 to 10^{11} s^{-1}. With $|\Delta E_{CT}|$ not too far away from λ, the CT rate is dominated by the pre-factor in the Marcus rate equation (see **Table A.6.1**). With

$|\Delta E_{CR}|$ much larger than λ, however, the CR rate is dominated by the exponential part and the CR rate falls deep into the Marcus inverted region. Within the limitations of the approximations taken, the ultrafast CT rates despite endothermic ΔE_{CT} indicates that although thermodynamically not favorable, the CT reactions can be kinetically feasible.

Table 6.1 also lists the CT and CR rates for P3HT and PBDTTPD that include experimentally measured E_{LOC} and E_{CT} for evaluating ΔE_{CT} and ΔE_{CR}. The J_{if} value included in the rate expression for each system is the average J_{if} from all configurations considered for each of the P3HT and PBDTTPD dyads. The calculated and experimentally parameterized CT and CR rates are generally coherent in that the CT rates are much faster than the CR rates. Calculated rates for P3AT based dyads are in good agreement with the experimentally parameterized rates while the calculated rates for PBDTTPD dyads are underestimated by roughly two orders of magnitude.

6.3.5. Effect of reorganization energy on charge-transfer and charge-recombination rates

The evolution of the CT and CR rates as a function of reorganization energies are shown in **Figure 6.5**.and **A.6.1**. For the considered range of λ, the CT and CR rates continually increase for P3AT with the increasing λ (CR rates increasing at a much faster rate). The CT and CR rates for the *t* configurations and experiment reach crossover points at the λ range of 0.45 – 055 eV. There is extremely good correlation in the evolution of the calculated and experimentally parameterized CT and CR rates for these configurations throughout the range of λ considered. For PBDTTPD, the CT rates are already past the peak and in the Marcus normal region. However, the crossover points are not yet reached and CT is still the dominant process.

From the calculated rates for all systems and configurations considered, it is difficult to choose configurations that have more favorable CT or CR rates. All systems and configurations have dominant CT rates for small λ, however, when λ approaches 0.5 eV or higher, the CR rates start to compete.

The results presented herein are roughly consistent with the ultrafast exciton dissociation rates at the thiophene:fullerene interface reported by Tamura *et al*.[48] They attribute these fast rates mainly to the strong coupling between the molecular excited state and CT state. Our results indicate that the CT rates are fast even when the couplings are weak. We find that along with the electronic coupling parameter, the pre-factor in the Marcus rate expression mainly dictates the CT rate while the exponential part dominates the CR rate.

Table 6.1 Calculated binding energies, electronic couplings, oligomer lowest excited state energies, oligomer:fullerene dyad charge-transfer energies, and charge-transfer and charge-recombination rates.

	BindE (kcal/ mol)	J_{LL} (meV)	J_{HL} (meV)	E_{LOC} (eV)	E_{CT} (eV)	Adj. E_{CT} (eV)[a]	ΔE_{CT} (eV)	ΔE_{CR} (eV)	λ = 0.25 eV		λ = 0.50 eV	
									k_{CT} (s^{-1})	k_{CR} (s^{-1})	k_{CT} (s^{-1})	k_{CR} (s^{-1})
P3AT-t-thp	-15.7	4	117	1.85	1.54	1.10	-0.75	-1.10	2.98E+07	3.33E+02	1.01E+11	3.06E+11
P3AT-t-bnd	-15.5	14	105	1.85	1.51	1.07	-0.78	-1.07	1.26E+08	1.88E+03	9.79E+11	4.90E+11
PBDTTPD-t-acp	-17.0	15	69	1.81	2.25	1.81	0.00	-1.81	6.82E+11	2.10E-27	4.30E+10	4.36E-01
PBDTTPD-t-don	-18.5	52	27	1.84	2.37	1.93	0.09	-1.93	9.14E+11	9.67E-35	6.86E+10	1.18E-04
PCDTBT-t-acp	-15.4	1	88	1.82	1.91	1.47	-0.35	-1.47	1.29E+10	2.56E-11	8.19E+09	2.29E+06
PCDTBT-t-don	-16.5	1	58	1.82	1.86	1.42	-0.40	-1.42	2.76E+09	1.15E-09	3.76E+09	6.29E+06
PCPDTBT-t-acp	-16.7	5	115	1.33	1.55	1.11	-0.22	-1.11	7.83E+11	1.67E+02	1.30E+11	2.35E+11
PCPDTBT-t-don	-7.2	1	13	1.34	1.72	1.28	-0.06	-1.28	4.45E+08	8.42E-06	2.98E+07	3.07E+07
PBDTTT-C-t-acp	-17.3	30	16	1.56	1.67	1.23	-0.33	-1.23	2.37E+13	6.40E-04	1.23E+13	2.06E+08
PBDTTT-C-t-don	-18.4	19	71	1.57	1.59	1.15	-0.42	-1.15	3.76E+12	4.13E+00	7.48E+12	3.34E+10
P3AT-s	-9.2	5	3	1.85	1.47	1.03	-0.82	-1.03	3.05E+06	2.25E+01	8.44E+10	1.15E+09
PBDTTPD-s	-6.1	1	5	1.81	2.00	1.56	-0.25	-1.56	4.83E+09	1.22E-17	1.05E+09	2.13E+02
PCDTBT-s-acp-td	-2.8	2	1	1.95	1.98	1.54	-0.41	-1.54	4.39E+10	3.57E-19	6.97E+10	1.87E+00
PCDTBT-s-acp-bz	-11.7	1	9	1.95	1.78	1.34	-0.61	-1.34	1.68E+08	2.77E-08	1.36E+10	2.11E+06
PCDTBT-s-don	-4.6	1	8	1.95	1.87	1.43	-0.52	-1.43	2.91E+08	7.65E-12	3.39E+09	7.24E+04
PCPDTBT-s-acp-td	-3.1	2	1	1.41	1.66	1.22	-0.19	-1.22	8.69E+10	1.06E-06	1.07E+10	2.12E+05
PCPDTBT-s-acp-bz	-8.7	1	7	1.34	1.49	1.05	-0.29	-1.05	6.47E+10	3.15E+01	2.14E+10	3.62E+09
PCPDTBT-s-don	-9.6	2	1	1.34	1.84	1.40	0.06	-1.40	2.74E+09	7.07E-13	1.84E+08	1.30E+03
PBDTTT-C-s	-6.8	1	4	1.56	1.77	1.33	-0.23	-1.33	2.11E+10	1.52E-08	3.65E+09	6.90E+05
P3HT-expt.	-	7	75	1.90	1.14[b]	-	-0.76	-1.14	8.03E+07	9.33E+00	3.59E+11	4.85E+10
PBDTTPD-expt.	-	22	34	1.75	1.52[c]	-	-0.23	-1.52	1.66E+13	3.07E-14	2.90E+12	4.94E+04

[a] E_{CT} adjustment by shifting of calculated values to measured values reported by Ko *et al.*[41] (see **Figure 5.3** and discussion above); [b] and [c] experimental values as reported by Ko *et al.*[41] and Hoke *et al.*[56]

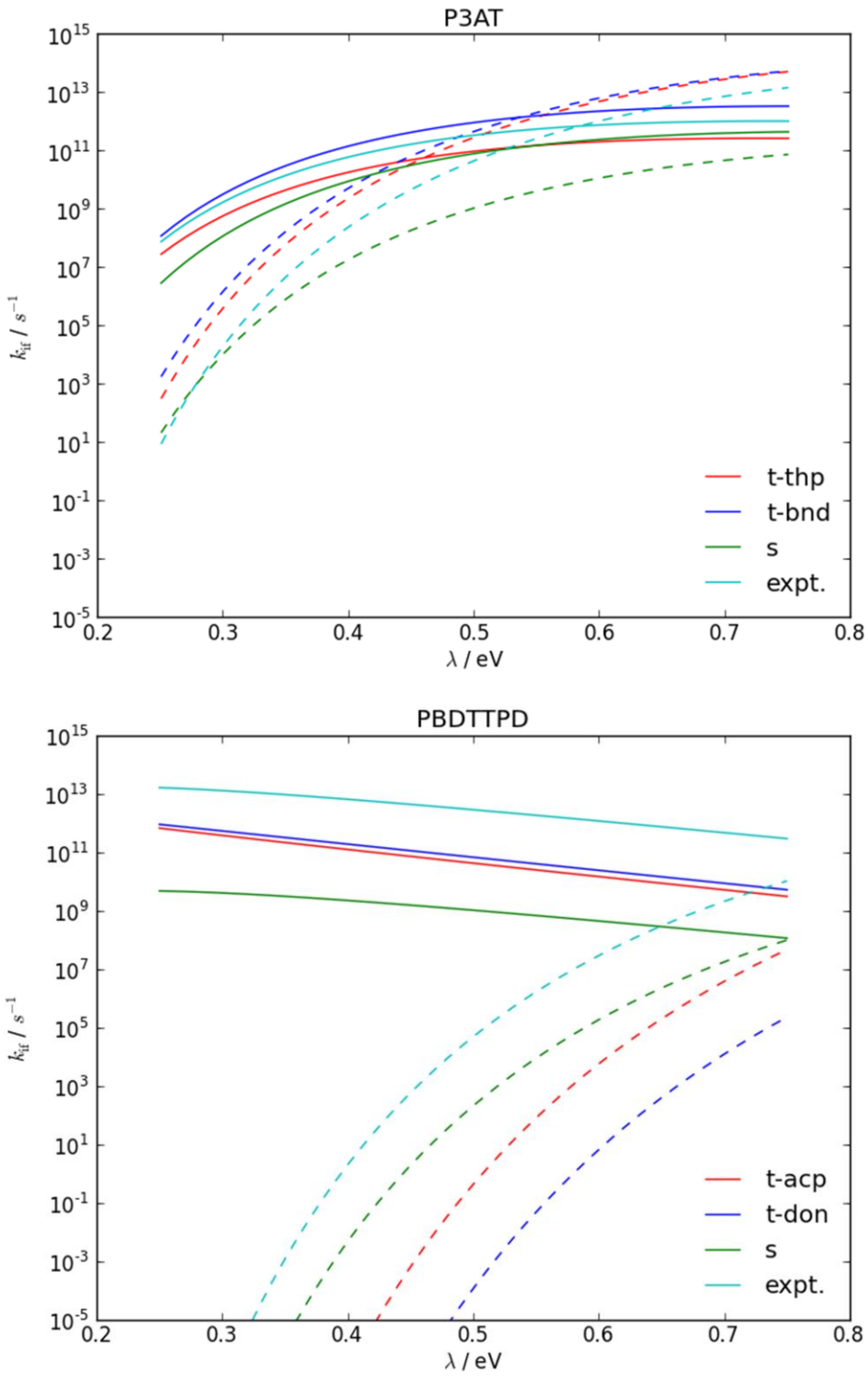

Figure 6.5 Charge-transfer (solid lines) and charge-recombination (dashed lines) rates as a function of reorganization energy for dyads including oligomers P3AT (top) and PBDTTPD (bottom). Rates based on experimental E_{CT} and E_{LOC} are included for reference.

6.4. Conclusions

The Marcus semiclassical model has been applied to calculate the rates for exciton-dissociation and charge-recombination processes in prototypical hole- and electron-transport materials including pentacene, sexithiophene, phthalocyanine, C_{60}, perylene bisimide, and perylene-tetracarboxylic diimide.[19-22] In this Chapter, we have investigated the impact of oligomer:fullerene molecular configurations and reorganization energy on the charge-transfer (CT) processes and the competing charge-recombination (CR) processes, for systems representing some of the best performing polymer:fullerene based solar cells.

Our results indicate that several key parameters that govern the CT and CR rates are affected by the oligomer:fullerene configurations. For the *t* (face-on) configurations, the effective electronic couplings relevant to CR were generally stronger than for CT; the couplings were weak (< 10 meV) for all *s* (edge-on) configurations. However, an important finding is that, despite the differences in the strengths of the electronic couplings, the CT rates were calculated to be fast and dominant (for small reorganization energies) for all oligomer:fullerene dyads irrespective of their configurations. This brings a key message: Excitons in these systems are prone to dissociate easily without significant competition from the CR process at the small reorganization energy limit. This is consistent with the fact that these systems constitute some of most efficient organic solar cells.

Upon increasing reorganization energy, the impact on CR rates is far more important than the CT process. Evaluation of accurate internal and external contributions to the reorganization energy is therefore critical in the calculation of the CR rates.

6.5. References

(1) Barbour, L. W.; Pensack, R. D.; Hegadorn, M.; Arzhantsev, S.; Asbury, J. B. *J. Phys. Chem. C* **2008**, *112*, 3926.

(2) Lloyd, M. T.; Lim, Y.-F.; Malliaras, G. G. *Appl. Phys. Lett.* **2008**, *92*, 143308.

(3) Banerji, N.; Cowan, S.; Leclerc, M.; Vauthey, E.; Heeger, A. J. *J. Am. Chem. Soc.* **2010**, *132*, 17459.

(4) Burkhard, G. F.; Hoke, E. T.; Scully, S. R.; McGehee, M. D. *Nano Lett.* **2009**, *9*, 4037.

(5) Grancini, G.; Maiuri, M.; Fazzi, D.; Petrozza, A.; Egelhaaf, H. J.; Brida, D.; Cerullo, G.; Lanzani, G. *Nat. Mater.* **2013**, *12*, 29.

(6) Bakulin, A. A.; Rao, A.; Pavelyev, V. G.; van Loosdrecht, P. H. M.; Pshenichnikov, M. S.; Niedzialek, D.; Cornil, J.; Beljonne, D.; Friend, R. H. *Science* **2012**, *335*, 1340.

(7) Jailaubekov, A. E.; Willard, A. P.; Tritsch, J. R.; Chan, W.-L.; Sai, N.; Gearba, R.; Kaake, L. G.; Williams, K. J.; Leung, K.; Rossky, P. J.; Zhu, X. Y. *Nat. Mater.* **2013**, *12*, 66.

(8) Cowan, S. R.; Banerji, N.; Leong, W. L.; Heeger, A. J. *Adv. Funct. Mater.* **2012**, *22*, 1116.

(9) Ma, W.; Yang, C.; Gong, X.; Lee, K.; Heeger, A. J. *Adv. Funct. Mater.* **2005**, *15*, 1617.

(10) Scharber, M. C.; Mühlbacher, D.; Koppe, M.; Denk, P.; Waldauf, C.; Heeger, A. J.; Brabec, C. J. *Adv. Mater.* **2006**, *18*, 789.

(11) Zhao, G.; He, Y.; Li, Y. *Adv. Mater.* **2010**, *22*, 4355.

(12) Blouin, N.; Michaud, A.; Leclerc, M. *Adv. Mater.* **2007**, *19*, 2295.

(13) Zhang, Y.; Hau, S. K.; Yip, H.-L.; Sun, Y.; Acton, O.; Jen, A. K.-Y. *Chem. Mater.* **2010**, *22*, 2696.

(14) Chen, H.-Y.; Hou, J.; Zhang, S.; Liang, Y.; Yang, G.; Yang, Y.; Yu, L.; Wu, Y.; Li, G. *Nat. Photonics* **2009**, *3*, 649.

(15) Muhlbacher, D.; Scharber, M.; Morana, M.; Zhu, Z. G.; Waller, D.; Gaudiana, R.; Brabec, C. *Adv. Mater.* **2006**, *18*, 2884.

(16) Liang, Y.; Feng, D.; Wu, Y.; Tsai, S.-T.; Li, G.; Ray, C.; Yu, L. *J. Am. Chem. Soc.* **2009**, *131*, 7792.

(17) Hou, J.; Chen, H.-Y.; Zhang, S.; Chen, R. I.; Yang, Y.; Wu, Y.; Li, G. *J. Am. Chem. Soc.* **2009**, *131*, 15586.

(18) Zou, Y.; Najari, A.; Berrouard, P.; Beaupre, S.; Reda Aich, B.; Tao, Y.; Leclerc, M. *J. Am. Chem. Soc.* **2010**, *132*, 5330.

(19) Lemaur, V.; Steel, M.; Beljonne, D.; Brédas, J.-L.; Cornil, J. *J. Am. Chem. Soc.* **2005**, *127*, 6077.

(20) Yi, Y.; Coropceanu, V.; Brédas, J.-L. *J. Am. Chem. Soc.* **2009**, *131*, 15777.

(21) Yi, Y.; Coropceanu, V.; Bredas, J.-L. *J. Mater. Chem.* **2011**, *21*, 1479.

(22) Caruso, D.; Troisi, A. *Proc. Natl. Acad. Sci.* **2012**, *109*, 13498.

(23) Isaacs, E. B.; Sharifzadeh, S.; Ma, B.; Neaton, J. B. *J. Phys. Chem. Lett.* **2011**, *2*, 2531.

(24) Ojala, A.; Petersen, A.; Fuchs, A.; Lovrincic, R.; Pölking, C.; Trollmann, J.; Hwang, J.; Lennartz, C.; Reichelt, H.; Höffken, H. W.; Pucci, A.; Erk, P.; Kirchartz, T.; Würthner, F. *Adv. Funct. Mater.* **2012**, *22*, 86.

(25) McMahon, D. P.; Cheung, D. L.; Troisi, A. *J. Phys. Chem. Lett.* **2011**, *2*, 2737.
(26) Cooling, N.; Burke, K. B.; Zhou, X.; Lind, S. J.; Gordon, K. C.; Jones, T. W.; Dastoor, P. C.; Belcher, W. J. *Sol. Energy Mater. Sol. Cells* **2011**, *95*, 1767.
(27) Risko, C.; McGehee, M. D.; Bredas, J.-L. *Chem. Sci.* **2011**, *2*, 1200.
(28) Pandey, L.; Doiron, C.; Sears, J. S.; Bredas, J. L. *Phys. Chem. Chem. Phys.* **2012**, *14*, 14243.
(29) Elstner, M.; Porezag, D.; Jungnickel, G.; Elsner, J.; Haugk, M.; Frauenheim, T.; Suhai, S.; Seifert, G. *Phys. Rev. B* **1998**, *58*, 7260.
(30) Aradi, B.; Hourahine, B.; Frauenheim, T. *J. Phys. Chem. A* **2007**, *111*, 5678.
(31) Niehaus, T. A.; Elstner, M.; Frauenheim, T.; Suhai, S. *J. Mol. Struct. THEOCHEM* **2001**, *541*, 185.
(32) Elstner, M.; Hobza, P.; Frauenheim, T.; Suhai, S.; Kaxiras, E. *J. Chem. Phys.* **2001**, *114*, 5149.
(33) Jung, G. Y.; Li, Z. Y.; Wu, W.; Chen, Y.; Olynick, D. L.; Wang, S. Y.; Tong, W. M.; Williams, R. S. *Langmuir* **2005**, *21*, 1158.
(34) Becke, A. D. *J. Chem. Phys.* **1993**, *98*, 5648.
(35) Lee, C.; Yang, W.; Parr, R. G. *Phys. Rev. B* **1988**, *37*, 785.
(36) Stephens, P. J.; Devlin, F. J.; Chabalowski, C. F.; Frisch, M. J. *J. Phys. Chem.* **1994**, *98*, 11623.
(37) Hariharan, P. C.; Pople, J. A. *Theor. Chim. Acta* **1973**, *28*, 213.
(38) Francl, M. M.; Pietro, W. J.; Hehre, W. J.; Binkley, J. S.; Gordon, M. S.; Defrees, D. J.; Pople, J. A. *J. Chem. Phys.* **1982**, *77*, 3654.
(39) Valiev, M.; Bylaska, E. J.; Govind, N.; Kowalski, K.; Straatsma, T. P.; Van Dam, H. J. J.; Wang, D.; Nieplocha, J.; Apra, E.; Windus, T. L.; de Jong, W. A. *Comput. Phys. Commun.* **2010**, *181*, 1477.
(40) Klamt, A.; Schuurmann, G. *J. Chem. Soc., Perkin Trans. 2* **1993**, *2*, 799.
(41) Ko, S.; Hoke, E. T.; Pandey, L.; Hong, S.; Mondal, R.; Risko, C.; Yi, Y.; Noriega, R.; McGehee, M. D.; Brédas, J.-L.; Salleo, A.; Bao, Z. *J. Am. Chem. Soc.* **2012**, *134*, 5222.
(42) Valeev, E. F.; Coropceanu, V.; da Silva Filho, D. A.; Salman, S.; Brédas, J.-L. *J. Am. Chem. Soc.* **2006**, *128*, 9882.
(43) Chai, J.-D.; Head-Gordon, M. *J. Chem. Phys.* **2008**, *128*, 084106.
(44) Marcus, R. A. *Rev. Mod. Phys.* **1993**, *65*, 599.
(45) Barbara, P. F.; Meyer, T. J.; Ratner, M. A. *J. Phys. Chem.* **1996**, *100*, 13148.
(46) Kawatsu, T.; Coropceanu, V.; Ye, A.; Bredas, J.-L. *J. Phys. Chem. C* **2008**, *112*, 3429.
(47) Subotnik, J. E.; Cave, R. J.; Steele, R. P.; Shenvi, N. *J. Chem. Phys.* **2009**, *130*, 234102.
(48) Tamura, H.; Burghardt, I.; Tsukada, M. *J. Phys. Chem. C* **2011**, *115*, 10205.
(49) Norton, J. E.; Brédas, J.-L. *J. Am. Chem. Soc.* **2008**, *130*, 12377.
(50) McMahon, D. P.; Troisi, A. *J. Phys. Chem. Lett.* **2010**, *1*, 941.
(51) Grimme, S. *J. Comput. Chem.* **2006**, *27*, 1787.
(52) Burns, L. A.; Mayagoitia, A. V.-.; Sumpter, B. G.; Sherrill, C. D. *J. Chem. Phys.* **2011**, *134*, 084107.
(53) Vázquez-Mayagoitia, A. l.; Sherrill, C. D.; Aprà, E.; Sumpter, B. G. *J. Chem. Theory Comput.* **2010**, *6*, 727.
(54) Fu, Y.-T.; Risko, C.; Brédas, J.-L. *Adv. Mater.* **2012**, *25*, 878.

(55) Verhoeven, J. W. In *Adv. Chem. Phys.*; John Wiley & Sons, Inc.: 2007, p 603.
(56) Hoke, E. T.; Vandewal, K.; Bartelt, J. A.; Mateker, W. R.; Douglas, J. D.; Noriega, R.; Graham, K. R.; Fréchet, J. M. J.; Salleo, A.; McGehee, M. D. *Adv. Energy Mater.* **2013**, *3*, 220.

CHAPTER 7

CONCLUSIONS AND OUTLOOK

7.1. Conclusions

Due to the potential in offering sustainable and cost-effective energy resources, the field of organic photovoltaics offers valuable prospect and is growing. Improvements in performance of the organic photovoltaic devices (along with their stability) have been recognized as important steps towards making them economically viable. Tremendous efforts are thus carried out to understand the mechanisms and key processes involved in photocurrent generation. A critical requirement in the optimization of a device is the comprehension of the bulk and interface properties of the materials that constitute the photoactive layer. As a first step towards understanding two key processes – absorption and exciton dissociation – we studied the intrinsic properties of the hole- and electron-transport materials at the molecular level using density functional theory-based methods. Our objectives were to i) investigate structure-property relationships of donor-acceptor materials, particularly to quantify how the geometric, electronic, and optical properties vary as a function of the chemical composition, ii) characterize the nature of their lowest excitons, and iii) depict the role of configurational variations at the interfaces between hole- and electron-transport materials and reorganization energy on exciton-dissociation and charge-recombination processes.

Donor-acceptor copolymers and small molecules are an important class of hole-transport materials. Due to the potential to harness a large portion of the solar energy spectrum, especially

in the near-infrared region, they have received a lot of interest from the organic photovoltaics community. Using a large set of donor and acceptor moieties to construct donor-acceptor repeat units, in Chapter 3, we discussed and quantified the role of specific donor/ acceptor combinations and thiophene spacers on the copolymer geometric, electronic, and optical properties. We found that the thiophene spacers help planarize the copolymer backbone (by 10 – 25°), destabilize the HOMO energies (by 0.1 – 0.4 eV) and increase the oscillator strengths (by 55 – 120 %) in tetramers of X/CPDP-T-Y-T compared to those for X/CPDP-Y. Additionally, as a result of the strong electron affinity of the benzobisthiadiazole acceptor, the C/CPDT-B2T LUMO is unusual as it displays contributions from the C/CPDT HOMO, in addition to the B2T LUMO, and provides a clear illustration of the role of energetic alignment in the mixing of donor and acceptor wavefunctions in donor-acceptor copolymers.

Chapter 4 focused on the use of long-range corrected density functionals in characterizing the lowest excited states and optical absorption spectra of a series of donor-acceptor small-optical gap systems. The tuned LRC functionals were shown to provide a description of the lowest excited states leading to better agreement with experimental optical absorption spectra compared to B3LYP or the standard LRC functionals. Based on the tuned ω values, the donor-acceptor copolymers can be considered to be more conjugated than polythiophenes. Importantly, the tuned LRC functionals provide a more localized description of the lowest singlet exciton than initially anticipated for donor-acceptor copolymers.

In addition to the use of suitable donor or acceptor moiety, the placement of side chains along the conjugated backbone can influence π-conjugated material properties. Chapter 5 provided details on the influence of alkyl side chains on the geometric and electronic properties of oligothiophenes and their interactions with fullerenes. Based on the trends in computed and

measured ionization potentials and the values of the electronic couplings at the HTM:ETM interface, the increase in V_{OC} for devices based on PDHTT and PDHBT (compared to P3HT) could be mainly correlated with the increase in ionization potential (a result of increased twist along the conjugated backbones). Also, the good correlation between the computed and measured E_{CT} values provides confidence in the use of constrained DFT in evaluating E_{CT} for thiophene-based π-conjugated systems.

Building on the work from earlier chapters, in Chapter 6 we investigated the impact of oligomer:fullerene packing configurations and reorganization energy on charge-transfer and charge-recombination processes. Within the approximations that were made, the CT rates were calculated, in the small reorganization energy limit, to be fast and dominant for all oligomer:fullerene dyads irrespective of the configurations, indicating that the excitons are prone to dissociate without substantial competing CR process. Also, it was found that the impact from the changes in reorganization energy in these oligomer:fullerene complexes is far more important for the CR rates. Accurate evaluation of reorganization energy, both from intramolecular and intermolecular contributions, is therefore critical for the calculation of CR rates.

7.2. Further considerations

The discussions presented in this dissertation provide steps towards understanding structure-property relationships of isolated molecular systems that aid in the design of improved materials and in the comprehension of the kinetics of exciton-dissociation and charge-recombination processes. While the studies of the intrinsic (individual) properties are a first necessary step, it is important to note that extrinsic factors such as the architecture of the photoactive layer, interactions of the photoactive layer components with each other and their environment, and the conditions of processing play critical roles in determining OPV

performance. To understand the complexities of the structures – on how they pack at the bulk and the interfaces – requires studying these materials at the molecular dynamics level. This allows the account of the steric effects from side-chains and their influences on intra- and inter-molecular geometries that are generally discarded when purely quantum-chemical methods are used. Further, such simulations can address the problem of conformation variability due to packing that cannot be grasped from geometry optimizations of molecular systems under isolated conditions.

Additionally, it is also important to get reliable descriptions of the local and charge-transfer states not only at the single molecule or dyad level, but on a scale that allows inclusion of a number of hole- and electron-transfer molecules. This will enable to account for charge-transfer states that could be delocalized over several molecules. Understanding how localized or delocalized the charge-transfer states is important as it can provide information on the size of the Coulombic barrier that has to be overcome to generate charge-separated carriers and avoid recombinative losses at the interfaces. This can be critical to understanding the mechanisms responsible for the efficient dissociation of excitons into separated charges at organic-organic interfaces, a problem that is not yet adequately understood.

Application of Marcus electron transfer theory is valid only in the case of very weak electronic couplings and under the assumption that the system is in thermal equilibrium. This means in practice that in order to use the Marcus formalism fully reliably, the electron transfer that takes place after optical excitation should be slower than nuclear relaxations. The rates we have calculated for the CT processes can reach up to 10^{13} Hz for some systems. Thus, such time scales are on the order of those for the fast bond-stretching nuclear relaxations. As a result, a

major advance in our computational methodology will be required to obtain a realistic description of such fast electron-transfer rates, by solving for the coupled electron-ion dynamics.

APPENDIX

ANCILLARY MATERIAL

Table A.3.1 HOMO and LUMO energies for isolated X/CPDP and X/CPDT donors determined at the B3LYP/6-31G(d,p) level. HOMO and LUMO energy differences between the dibenzo- and dithiophene-based donors as a function of the X-substituent are included. All energies are expressed in eV.

Donors	HOMO	LUMO		X-substituent			CPDP - CPDT		
C/CPDP	-5.74	-0.76		N-C	N-Si	C-Si	N	C	S
C/CPDT	-5.19	-1.02		ΔHOMO			ΔHOMO		
N/CPDP	-5.33	-0.64	CPDP	0.41	0.46	0.05	-0.23	-0.55	-0.49
N/CPDT	-5.10	-0.56	CPDT	0.09	0.20	0.11			
Si/CPDP	-5.79	-0.93		ΔLUMO			ΔLUMO		
Si/CPDT	-5.30	-1.29	CPDP	0.12	0.29	0.17	-0.08	0.26	0.36
			CPDT	0.46	0.73	0.28			

Table A.3.2 HOMO and LUMO energies of the acceptors (isolated (Y) and bis-thiophene substituted (T-Y-T)) as determined at the B3LYP/6-31G(d,p) level. HOMO and LUMO energy differences between the two series are also included. All energies are expressed in eV. The HOMO and LUMO energies of thiophene and $PC_{61}BM$ are given as reference.

	Y		**T-Y-T**		**ΔE([T-Y-T] – Y)**	
Acceptor	**HOMO**	**LUMO**	**HOMO**	**LUMO**	**HOMO**	**LUMO**
BX	-6.87	-2.45	-5.53	-2.71	1.33	-0.25
BT	-6.62	-2.35	-5.36	-2.63	1.26	-0.27
BSe	-6.48	-2.44	-5.30	-2.69	1.18	-0.25
B2T	-6.20	-3.56	-5.10	-3.53	1.11	0.03
TQ	-5.36	-2.52	-4.98	-2.66	0.38	-0.14
QX	-6.71	-1.94	-5.26	-2.33	1.44	-0.40
PP	-6.98	-2.38	-5.42	-2.60	1.56	-0.21
PX	-7.41	-2.98	-5.72	-3.02	1.68	-0.04
PT	-7.09	-2.83	-5.53	-2.93	1.56	-0.10
PSe	-6.93	-2.91	-5.47	-3.00	1.47	-0.09
TP	-6.24	-2.27	-5.01	-2.63	1.23	-0.36
TPPh	-5.96	-2.21	-4.89	-2.55	1.07	-0.34
Thiophene	-6.35	-0.23				
$PC_{61}BM$	-5.66	-3.09				

Table A.3.3 HOMO and LUMO energies, fundamental (HOMO-LUMO) gap (E_G), optical gap (E_{OP}, $S_0 \rightarrow S_1$ transition energy), transition dipole moment (μ), and oscillator strength (f) determined at the B3LYP/6-31G(d,p) level for the N/CPDP- and N/CPDT-based DA tetramers. All energies are expressed in eV and transition dipole moments in Debye.

	HOMO	LUMO	E_G	E_{OP}	μ	f
N/CPDP-BX	-5.31	-2.65	2.66	2.29	18.01	2.82
N/CPDP-BT	-5.16	-2.46	2.69	2.30	15.07	1.98
N/CPDP-BSe	-5.09	-2.52	2.57	2.18	14.06	1.63
N/CPDP-B2T	-4.95	-3.47	1.48	1.23	19.26	1.73
N/CPDP-TQ	-4.83	-2.50	2.33	1.99	12.95	1.27
N/CPDP-QX	-5.14	-2.04	3.11	2.67	13.30	1.79
N/CPDP-PP	-5.23	-2.43	2.80	2.39	15.05	2.05
N/CPDP-PX	-5.44	-3.08	2.36	2.03	18.79	2.72
N/CPDP-PT	-5.25	-2.90	2.35	2.00	16.67	2.10
N/CPDP-PSe	-5.19	-2.95	2.23	1.87	16.00	1.82
N/CPDP-TP	-4.72	-2.61	2.11	1.78	18.52	2.31
N/CPDP-TPPh	-4.62	-2.53	2.08	1.75	17.34	1.99
N/CPDP-T-BX-T	-4.95	-2.78	2.18	1.87	26.33	4.93
N/CPDP-T-BT-T	-4.82	-2.68	2.13	1.82	23.89	3.93
N/CPDP-T-BSe-T	-4.76	-2.74	2.01	1.70	22.77	3.34
N/CPDP-T-B2T-T	-4.60	-3.52	1.08	0.91	27.85	2.69
N/CPDP-T-TQ-T	-4.70	-2.69	2.01	1.70	19.7	2.50
N/CPDP-T-QX-T	-4.77	-2.40	2.37	2.02	23.84	4.35
N/CPDP-T-PP-T	-4.86	-2.64	2.21	1.88	23.42	3.91
N/CPDP-T-PX-T	-5.06	-3.05	2.02	1.74	26.26	4.56
N/CPDP-T-PT-T	-4.92	-2.95	1.97	1.68	23.81	3.62
N/CPDP-T-PSe-T	-4.87	-3.01	1.85	1.57	22.81	3.09
N/CPDP-T-TP-T	-4.58	-2.73	1.85	1.57	24.78	3.65
N/CPDP-T-TPPh-T	-4.51	-2.66	1.84	1.56	23.75	3.34
N/CPDT-BX	-4.62	-3.01	1.61	1.41	27.43	4.01
N/CPDT-BT	-4.42	-2.83	1.59	1.35	25.7	3.38
N/CPDT-BSe	-4.35	-2.87	1.47	1.24	25.43	3.05
N/CPDT-B2T	-4.17	-3.81	0.35	0.56	31.83	2.15
N/CPDT-TQ	-4.22	-2.86	1.36	1.14	24.8	2.65
N/CPDT-QX	-4.34	-2.52	1.82	1.54	24.06	3.38
N/CPDT-PP	-4.47	-2.81	1.66	1.41	24.24	3.15
N/CPDT-PX	-4.77	-3.37	1.40	1.25	24.42	2.82
N/CPDT-PT	-4.56	-3.16	1.40	1.22	24.2	2.70
N/CPDT-PSe	-4.49	-3.21	1.27	1.10	23.56	2.32
N/CPDT-TP	-4.12	-2.89	1.23	1.08	27.98	3.22
N/CPDT-TPPh	-4.02	-2.80	1.22	1.06	27.48	3.03

N/CPDT-T-BX-T	-4.58	-2.95	1.63	1.36	34.05	5.98
N/CPDT-T-BT-T	-4.45	-2.84	1.62	1.34	31.69	5.10
N/CPDT-T-BSe-T	-4.41	-2.88	1.53	1.25	30.98	4.55
N/CPDT-T-B2T-T	-4.27	-3.61	0.66	0.59	46.19	4.79
N/CPDT-T-TQ-T	-4.42	-2.76	1.66	1.37	24.69	3.16
N/CPDT-T-QX-T	-4.41	-2.58	1.83	1.52	30.26	5.30
N/CPDT-T-PP-T	-4.48	-2.80	1.68	1.39	30.65	4.96
N/CPDT-T-PX-T	-4.67	-3.20	1.47	1.25	34.15	5.51
N/CPDT-T-PT-T	-4.54	-3.08	1.46	1.22	31.96	4.73
N/CPDT-T-PSe-T	-4.49	-3.13	1.36	1.13	31.27	4.19
N/CPDT-T-TP-T	-4.27	-2.88	1.38	1.14	34.46	5.13
N/CPDT-T-TPPh-T	-4.22	-2.81	1.41	1.16	32.76	4.70

Table A.3.4 First vertical transition ($S_0 \rightarrow S_1$) properties including E_{OP} (eV), transition dipole moment (μ), *f*, and the corresponding electronic configurations determined at the TD-B3LYP/6-31G(d,p) level for N/CPDP- and N/CPDT-based DA tetramers.

	E_{OP} (eV)	μ (Debye)	*f*	Electronic configuration (%)
N/CPDP-BX	2.29	18.01	2.82	HOMO-1→LUMO (2)
				HOMO-1→LUMO+1 (7)
				HOMO→LUMO (85)
				HOMO→LUMO+1 (3)
N/CPDP-BT	2.30	15.07	1.98	HOMO-1→LUMO+1 (9)
				HOMO→LUMO (82)
				HOMO→LUMO+1 (3)
N/CPDP-BSe	2.18	14.06	1.63	HOMO-1→LUMO+1 (9)
				HOMO→LUMO (81)
				HOMO→LUMO+1 (2)
N/CPDP-B2T	1.23	19.26	1.73	HOMO-1→LUMO (3)
				HOMO→LUMO (75)
				HOMO→LUMO+1 (17)
N/CPDP-TQ	1.99	12.95	1.27	HOMO-2→LUMO+3 (2)
				HOMO-1→LUMO (4)
				HOMO-1→LUMO+1 (3)
				HOMO-1→LUMO+2 (6)
				HOMO→LUMO (55)
				HOMO→LUMO+1 (25)
N/CPDP-QX	2.67	13.30	1.79	HOMO-1→LUMO+1 (8)
				HOMO→LUMO (76)
				HOMO→LUMO+1 (4)
				HOMO→LUMO+2 (2)
N/CPDP-PP	2.39	15.05	2.05	HOMO-5→LUMO+1 (3)
				HOMO-4→LUMO+1 (6)
				HOMO→LUMO (82)
				HOMO→LUMO+2 (2)
N/CPDP-PX	2.03	18.79	2.72	HOMO-2→LUMO (6)
				HOMO-2→LUMO+1 (2)
				HOMO→LUMO (76)
				HOMO→LUMO+1 (11)
N/CPDP-PT	2.00	16.67	2.10	HOMO-1→LUMO (3)
				HOMO-1→LUMO+1 (5)
				HOMO→LUMO (81)
				HOMO→LUMO+1 (7)
N/CPDP-PSe	1.87	16.00	1.82	HOMO-1→LUMO (3)
				HOMO-1→LUMO+1 (5)
				HOMO→LUMO (78)
				HOMO→LUMO+1 (9)
N/CPDP-TP	1.78	18.52	2.31	HOMO-1→LUMO+1 (6)
				HOMO→LUMO (91)
N/CPDP-TPPh	1.75	17.34	1.99	HOMO-1→LUMO+1 (6)

				HOMO→LUMO (91)
N/CPDP-T-BX-T	1.87	26.33	4.93	HOMO-2→LUMO+2 (2) HOMO-1→LUMO+1 (12)
				HOMO→LUMO (75)
				HOMO→LUMO+1 (3)
N/CPDP-T-BT-T	1.82	23.89	3.93	HOMO-2→LUMO+2 (4) HOMO-1→LUMO+1 (14)
				HOMO→LUMO (74)
N/CPDP-T-BSe-T	1.70	22.77	3.34	HOMO-2→LUMO+2 (4) HOMO-1→LUMO+1 (14)
				HOMO→LUMO (73)
N/CPDP-T-B2T-T	0.91	27.85	2.69	HOMO-1→LUMO (5) HOMO-1→LUMO+2 (2)
				HOMO→LUMO (74)
				HOMO→LUMO+1 (17)
N/CPDP-T-TQ-T	1.70	19.70	2.50	HOMO-2→LUMO+2 (6) HOMO-1→LUMO+1 (17)
				HOMO→LUMO (71)
N/CPDP-T-QX-T	2.02	23.84	4.35	HOMO-2→LUMO+2 (5) HOMO-1→LUMO+1 (16)
				HOMO→LUMO (73)
N/CPDP-T-PP-T	1.88	23.42	3.91	HOMO-2→LUMO+3 (2) HOMO-1→LUMO (3) HOMO-1→LUMO+1 (10) HOMO-1→LUMO+2 (3)
				HOMO→LUMO (67)
				HOMO→LUMO+1 (7)
N/CPDP-T-PX-T	1.74	26.26	4.56	HOMO-2→LUMO+1 (3) HOMO-1→LUMO (13) HOMO-1→LUMO+2 (5)
				HOMO→LUMO (50)
				HOMO→LUMO+1 (23)
N/CPDP-T-PT-T	1.68	23.81	3.62	HOMO-2→LUMO+1 (3) HOMO-2→LUMO+3 (3) HOMO-1→LUMO (9) HOMO-1→LUMO+2 (6)
				HOMO→LUMO (50)
				HOMO→LUMO+1 (24)
N/CPDP-T-PSe-T	1.57	22.81	3.09	HOMO-2→LUMO+1 (3) HOMO-2→LUMO+3 (3) HOMO-1→LUMO (9) HOMO-1→LUMO+2 (7)
				HOMO→LUMO (38)
				HOMO→LUMO+1 (34)
				HOMO→LUMO+2 (2)
N/CPDP-T-TP-T	1.57	24.78	3.65	HOMO-2→LUMO+2 (3) HOMO-1→LUMO+1 (13)
				HOMO→LUMO (78)
N/CPDP-T-TPPh-T	1.56	23.75	3.34	HOMO-2→LUMO+2 (3) HOMO-1→LUMO+1 (13)

				HOMO→LUMO (79)
N/CPDT-BX	1.41	27.43	4.01	HOMO-1→LUMO+1 (3)
				HOMO→LUMO (96)
N/CPDT-BT	1.35	25.70	3.38	HOMO-1→LUMO+1 (4)
				HOMO→LUMO (95)
N/CPDT-BSe	1.24	25.43	3.05	HOMO-1→LUMO+1 (4)
				HOMO→LUMO (95)
N/CPDT-B2T	0.56	31.83	2.15	HOMO-1→LUMO+1 (4)
				HOMO→LUMO (88)
				HOMO→LUMO+1 (4)
N/CPDT-TQ	1.14	24.80	2.65	HOMO-1→LUMO+1 (4)
				HOMO→LUMO (96)
N/CPDT-QX	1.54	24.06	3.38	HOMO-1→LUMO+1 (4)
				HOMO→LUMO (95)
N/CPDT-PP	1.41	24.24	3.15	HOMO-1→LUMO+1 (3)
				HOMO→LUMO (93)
N/CPDT-PX	1.25	24.42	2.82	HOMO→LUMO (96)
N/CPDT-PT	1.22	24.20	2.70	HOMO→LUMO (93)
				HOMO→LUMO+1 (3)
N/CPDT-PSe	1.10	23.56	2.32	HOMO→LUMO (93)
				HOMO→LUMO+1 (3)
N/CPDT-TP	1.08	27.98	3.22	HOMO-1→LUMO+1 (3)
				HOMO→LUMO (98)
N/CPDT-TPPh	1.06	27.48	3.03	HOMO-1→LUMO+1 (3)
				HOMO→LUMO (98)
N/CPDT-T-BX-T	1.36	34.05	5.98	HOMO-1→LUMO+1 (9)
				HOMO→LUMO (87)
N/CPDT-T-BT-T	1.34	31.69	5.10	HOMO-1→LUMO+1 (10)
				HOMO→LUMO (86)
N/CPDT-T-BSe-T	1.25	30.98	4.55	HOMO-1→LUMO+1 (10)
				HOMO→LUMO (86)
N/CPDT-T-B2T-T	0.59	46.19	4.79	HOMO-1→LUMO+1 (2)
				HOMO→LUMO (96)
N/CPDT-T-TQ-T	1.37	24.69	3.16	HOMO-1→LUMO (3)
				HOMO-1→LUMO+1 (9)
				HOMO→LUMO (74)
				HOMO→LUMO+1 (6)
N/CPDT-T-QX-T	1.52	30.26	5.30	HOMO-2→LUMO+2 (2)
				HOMO-1→LUMO+1 (11)
				HOMO→LUMO (84)
N/CPDT-T-PP-T	1.39	30.65	4.96	HOMO-1→LUMO (3)
				HOMO-1→LUMO+1 (8)
				HOMO→LUMO (80)
				HOMO→LUMO+1 (5)
N/CPDT-T-PX-T	1.25	34.15	5.51	HOMO-1→LUMO (10)
				HOMO→LUMO (71)
				HOMO→LUMO+1 (12)
N/CPDT-T-PT-T	1.22	31.96	4.73	HOMO-1→LUMO (8)
				HOMO-1→LUMO+1 (3)

				HOMO→LUMO (73)
				HOMO→LUMO+1 (12)
N/CPDT-T-PSe-T	1.13	31.27	4.19	HOMO-1→LUMO (9)
				HOMO-1→LUMO+2 (2)
				HOMO→LUMO (68)
				HOMO→LUMO+1 (16)
N/CPDT-T-TP-T	1.14	34.46	5.13	HOMO-1→LUMO+1 (8)
				HOMO→LUMO (87)
N/CPDT-T-TPPh-T	1.16	32.76	4.70	HOMO-1→LUMO+1 (9)
				HOMO→LUMO (87)

Table A.4.1 Tuned omega values ($bohr^{-1}$) for the ωB97 and BNL functionals from monomer to hexamer.

n	1	2	3	4	5	6
ωB97						
PBDTTPD	0.188	0.144	0.129	0.124	0.122	0.124
PBDTTT-C	0.190	0.141	0.124	0.117	0.114	0.115
PBDTTT-CF	0.188	0.142	0.125	0.118	0.115	0.116
PBDTTT-E	0.185	0.139	0.123	0.115	0.119	0.116
PCDTBT	0.186	0.156	0.151	0.152		
PCPDTBT	0.197	0.152	0.125	0.113	0.107	0.104
BNL						
PBDTTPD	0.196	0.150	0.134	0.129		
PBDTTT-C	0.197	0.147	0.129	0.121		
PBDTTT-CF	0.196	0.148	0.130	0.123		
PBDTTT-E	0.193	0.144	0.127	0.120		
PCDTBT	0.194	0.162	0.158	0.158		
PCPDTBT	0.211	0.160	0.132	0119		

Table A.4.2 TD-DFT $S_0 \rightarrow S_1$ transition energies (in eV) for the oligomers using the ωB97 (tuned and default ω) and B3LYP functionals.

n	1	2	3	4	5	6
B3LYP						
PBDTTPD	2.76	2.31	2.13	2.04	1.99	1.96
PBDTTT-C	2.61	2.11	1.89	1.78	1.72	1.68
PBDTTT-CF	2.59	2.15	1.93	1.83	1.76	1.75
PBDTTT-E	2.70	2.14	1.92	1.81	1.74	1.71
PCDTBT	2.15	1.93	1.86	1.83	-	-
PCPDTBT	2.31	1.73	1.49	1.36	1.29	1.24
Default ωB97						
PBDTTPD	3.72	3.16	2.99	2.93	2.87	2.85
PBDTTT-C	3.50	2.94	2.76	2.67	2.62	2.59
PBDTTT-CF	3.54	2.99	2.82	2.74	2.68	2.67
PBDTTT-E	3.54	2.93	2.77	2.68	2.63	2.60
PCDTBT	3.01	2.85	2.79	2.79	-	-
PCPDTBT	3.24	2.54	2.34	2.24	2.19	2.16
Tuned ωB97						
PBDTTPD	3.16	2.56	2.34	2.25	2.19	2.18
PBDTTT-C	3.01	2.33	2.08	1.97	1.90	1.88
PBDTTT-CF	3.03	2.38	2.14	2.03	1.95	1.95
PBDTTT-E	3.07	2.35	2.11	1.99	1.96	1.91
PCDTBT	2.53	2.24	2.18	2.18	-	-
PCPDTBT	2.81	2.00	1.68	1.53	1.44	1.39

Table A.4.3 TD-DFT $S_0 \rightarrow S_1$ energies (in eV) at the polymer limit using linear (1/n) and exponential extrapolation fits from the oligomer calculated data. The linear regression (Rsq) and parameter *a* (that describes how fast En saturates towards E_∞) are also included.

	Linear Fit (vs. 1/n)		Exponential Fit	
	E_∞	Rsq.	E_∞	*a*
B3LYP				
PBDTTPD	1.81	0.998	1.95	0.78
PBDTTT-C	1.51	0.996	1.67	0.73
PBDTTT-CF	1.58	0.992	1.72	0.70
PBDTTT-E	1.51	0.999	1.70	0.79
PCDTBT	1.72	1.000	1.82	1.04
PCPDTBT	1.05	0.996	1.23	0.73
Default ωB97				
PBDTTPD	2.66	0.998	2.86	0.99
PBDTTT-C	2.40	1.000	2.60	0.91
PBDTTT-CF	2.48	0.999	2.67	0.94
PBDTTT-E	2.40	0.998	2.62	0.99
PCDTBT	2.70	0.990	2.77	1.22
PCPDTBT	1.92	0.998	2.17	1.00
Tuned ωB97				
PBDTTPD	1.95	0.999	2.17	0.93
PBDTTT-C	1.63	0.999	1.87	0.88
PBDTTT-CF	1.70	0.999	1.93	0.87
PBDTTT-E	1.66	0.999	1.92	0.94
PCDTBT	2.03	0.979	2.17	1.61
PCPDTBT	1.11	0.999	1.38	0.81

Table A.5.1 Hole mobility, optimized thickness, and internal quantum efficiency of polymer:$PC_{71}BM$ solar cells.

Polymer	μ_h (cm^2/Vs) [a]	*Thickness (nm)*	Fill Factor [c]	*IQE (%)* [b]	J_{sc} (mA/cm^2) [c]
P3HT	3×10^{-4}	225	0.66	67	9.56
PDHTT	3×10^{-4}	165	0.66	67	8.54
PDHBT	7×10^{-5}	105	0.61	55	5.87
RRa-P3HT	2×10^{-5}	65	0.41	57	5.97

[a] Space charge limited hole mobility measured for hole only diodes. [b] Wavelength averaged internal quantum efficiency accounting for optical interference effects and parasitic absorptions in the electrodes. [c] Average values.

Table A.6.1 Charge-transfer and charge-recombination reaction enthalpies, rates, and contribution to the rate from the exponential and pre-factor parts of the Marcus rate equation (λ and T considered to be 0.25 eV and 300 K, respectively). PBDTTPD and PCPDTBT included as representative examples.

$$k_{if} = J_{if}^2 \sqrt{\frac{\pi}{\lambda k_B T \hbar^2}} \exp\left[\frac{-(\Delta G^0 + \lambda)^2}{4\lambda k_B T}\right]$$

	ΔE_{CT} / eV	ΔE_{CR} / eV	$\mathbf{k_{CT}}$ / s^{-1}	$\mathbf{k_{CR}}$ / s^{-1}	**CT**	**CR**	**CT**	**CR**
					Pre-factor	Pre-factor	Expon.	Expon.
PBDTTPD-t-acp	0.00	-1.81	6.82E+11	2.10E-27	7.31E+12	1.60E+14	9.33E-02	1.31E-41
PBDTTPD-t-don	0.09	-1.93	9.14E+11	9.67E-35	9.09E+13	2.51E+13	1.01E-02	3.85E-48
PBDTTPD-s	-0.25	-1.56	4.83E+09	1.22E-17	4.84E+09	8.24E+11	1.00E+00	1.48E-29
PBDTTPD-expt	-0.23	-1.52	1.66E+13	3.07E-14	1.68E+13	3.83E+13	9.85E-01	8.03E-28
PCPDTBT-t-acp	-0.22	-1.11	7.83E+11	1.67E+02	8.04E+11	4.44E+14	9.74E-01	3.76E-13
PCPDTBT-t-don	-0.06	-1.28	4.45E+08	8.42E-06	1.93E+09	5.59E+12	2.31E-01	1.51E-18
PCPDTBT-s-acp-td	-0.19	-1.22	8.69E+10	1.06E-06	1.01E+11	6.78E+09	8.56E-01	1.56E-16
PCPDTBT-s-acp-bz	-0.29	-1.05	6.47E+10	3.15E+01	6.95E+10	1.78E+12	9.32E-01	1.77E-11
PCPDTBT-s-don	0.06	-1.40	2.74E+09	7.07E-13	1.05E+11	1.17E+10	2.61E-02	6.07E-23

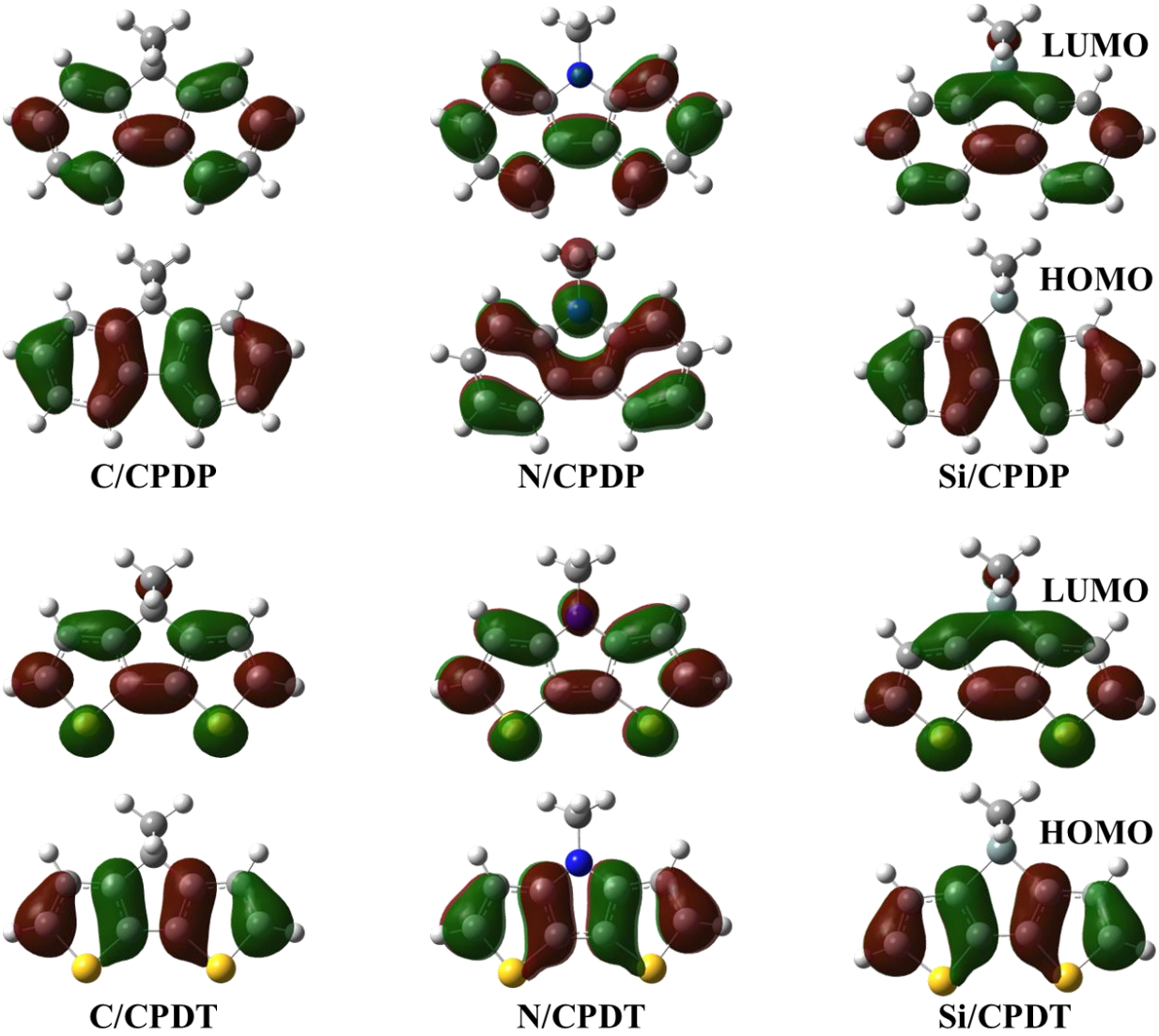

Figure A.3.1 Illustration of HOMO and LUMO wave functions (isovalue surface 0.02 a.u.) of the isolated donor molecules evaluated at the B3LYP/6-31G(d,p) level.

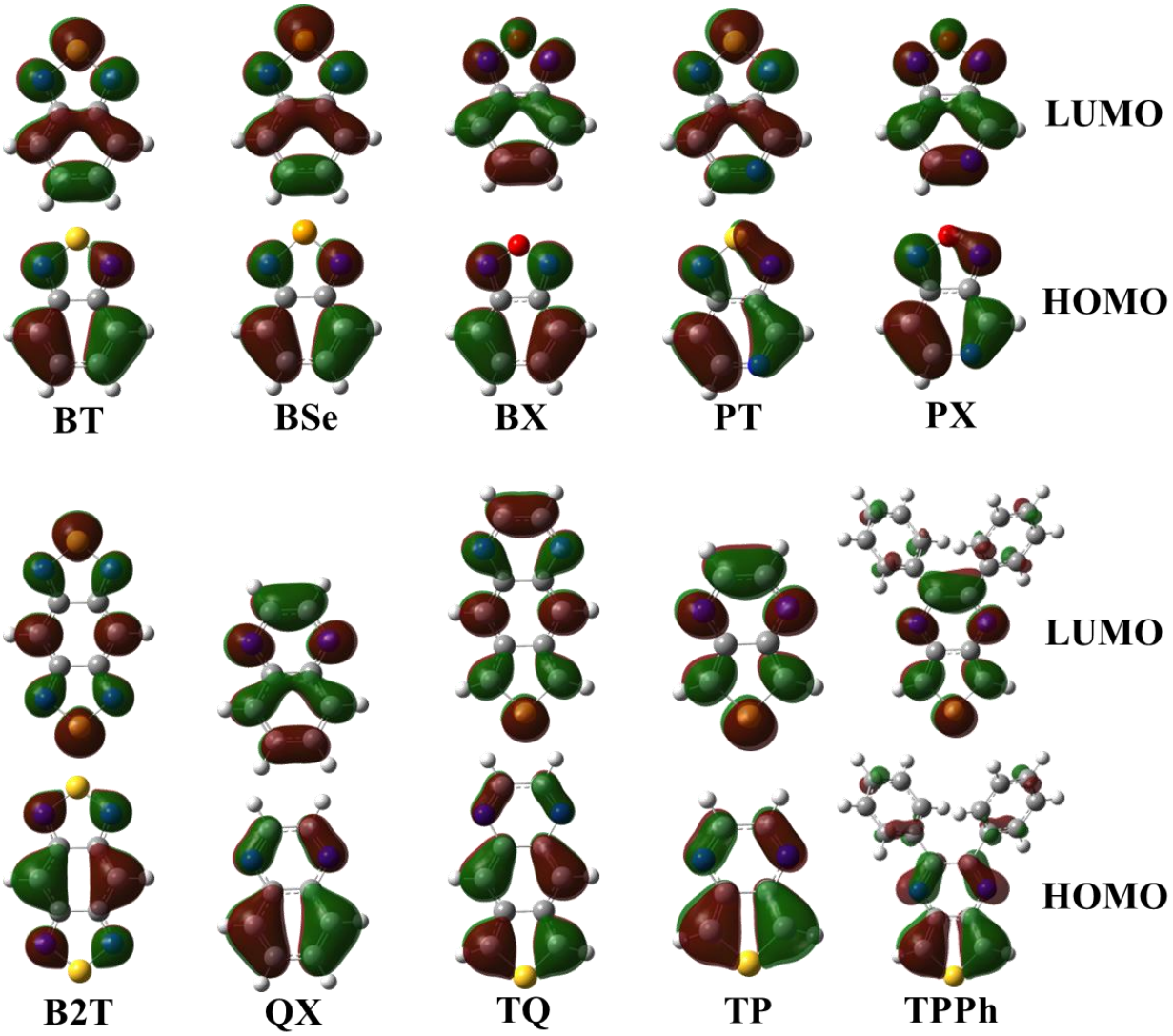

Figure A.3.2 Illustration of HOMO and LUMO wave functions (isovalue surface 0.02 a.u.) of select acceptors (Y) calculated at the B3LYP/6-31G(d,p) level.

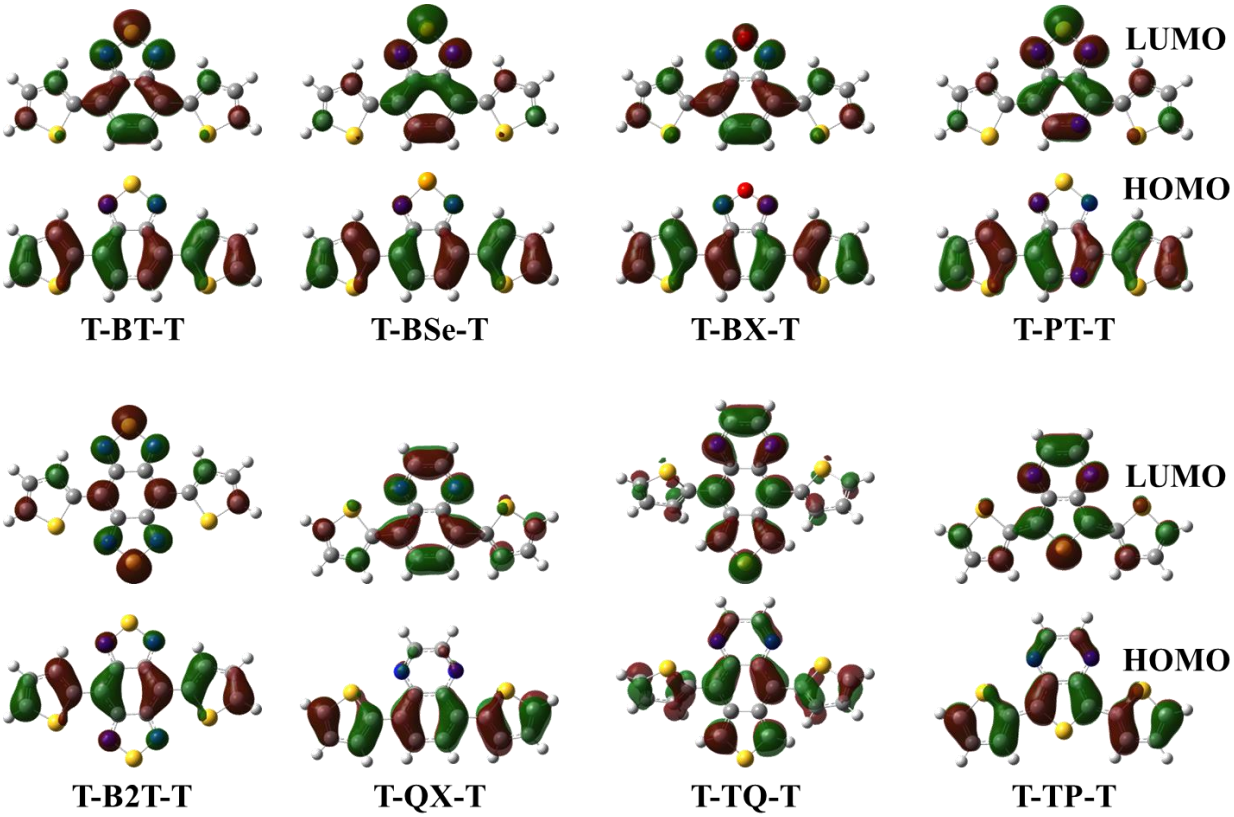

Figure A.3.3 Illustration of the HOMO and LUMO wave functions (isovalue surface 0.02 a.u.) for select bis-thiophene substituted (T-Y-T) acceptors calculated at the B3LYP/6-31G(d,p) level.

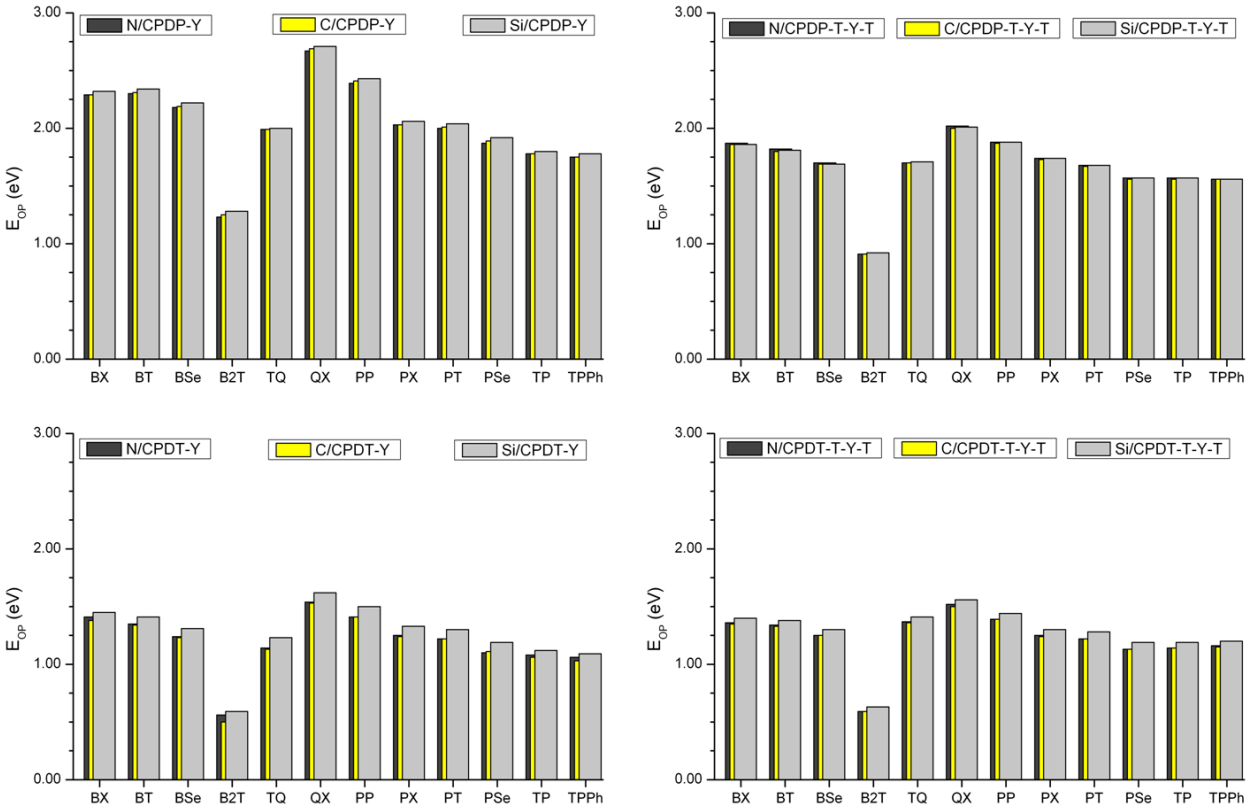

Figure A.3.4 D-A oligomer (tetramer) first vertical transition ($S_0 \rightarrow S_1$) energies determined at the TD-B3LYP/6-31G(d,p) level.

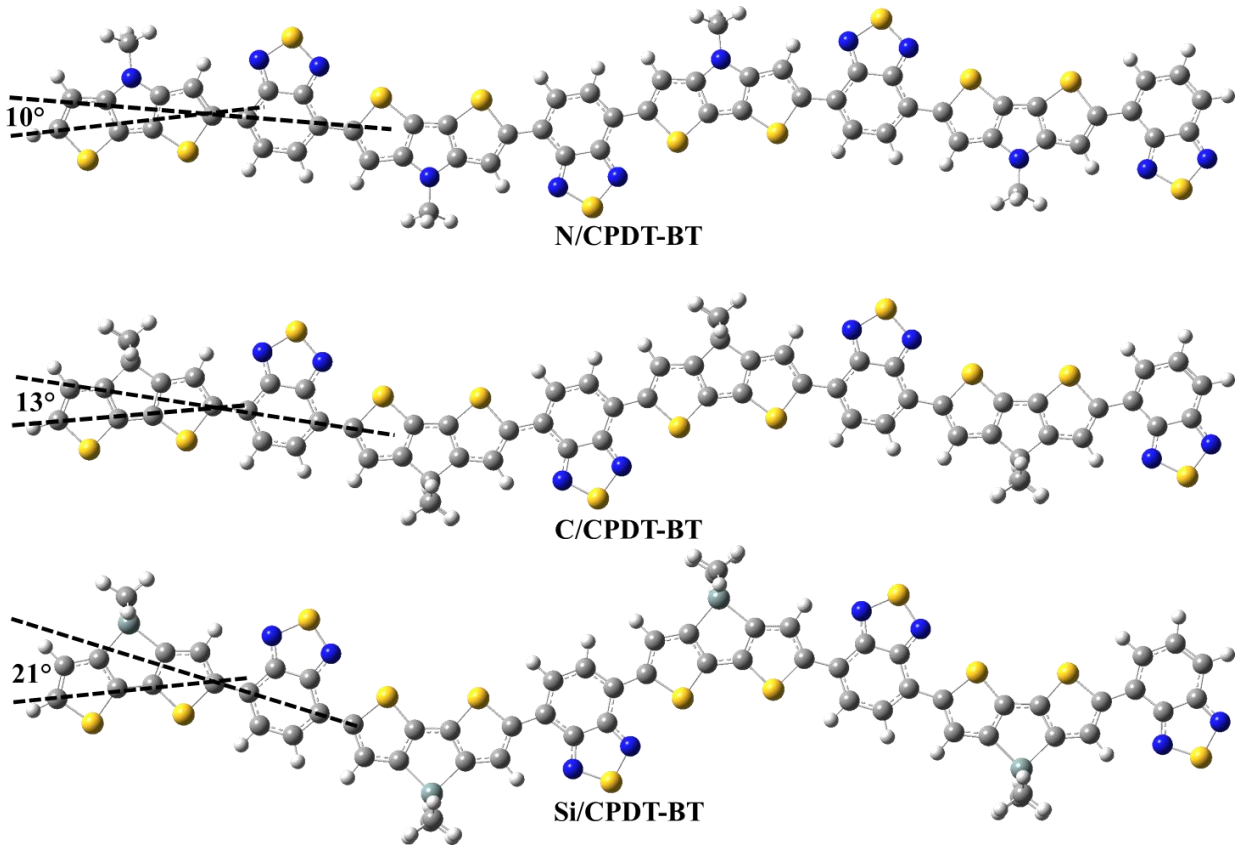

Figure A.3.5 Illustration of increased curvature (decreased linearity) in the conjugated backbone in X/CPDP-BT as a function of the X-substituent [NH_3, $CH_2(CH_3)_2$, and $SiH_2(CH_3)_2$] group.

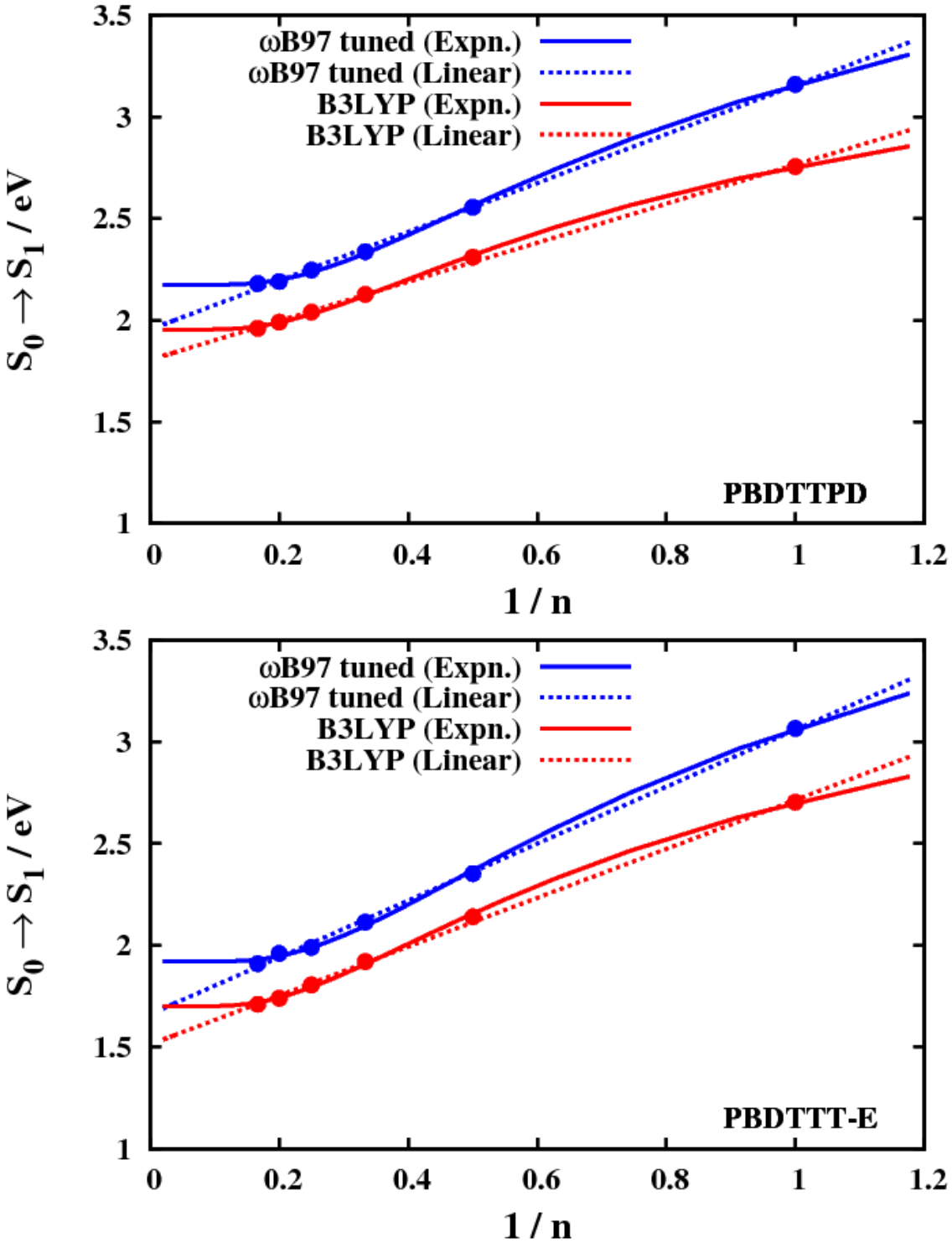

Figure A.4.1 Evolution of the first transition energy ($S_0 \rightarrow S_1$) with respect to inverse number of repeat units (1/n) for PBDTTPD and PBDTTT-E at the TD-DFT level for the B3LYP and tuned ωB97 functionals. Extrapolations of the $S_0 \rightarrow S_1$ energy using linear and exponential fits are also included.

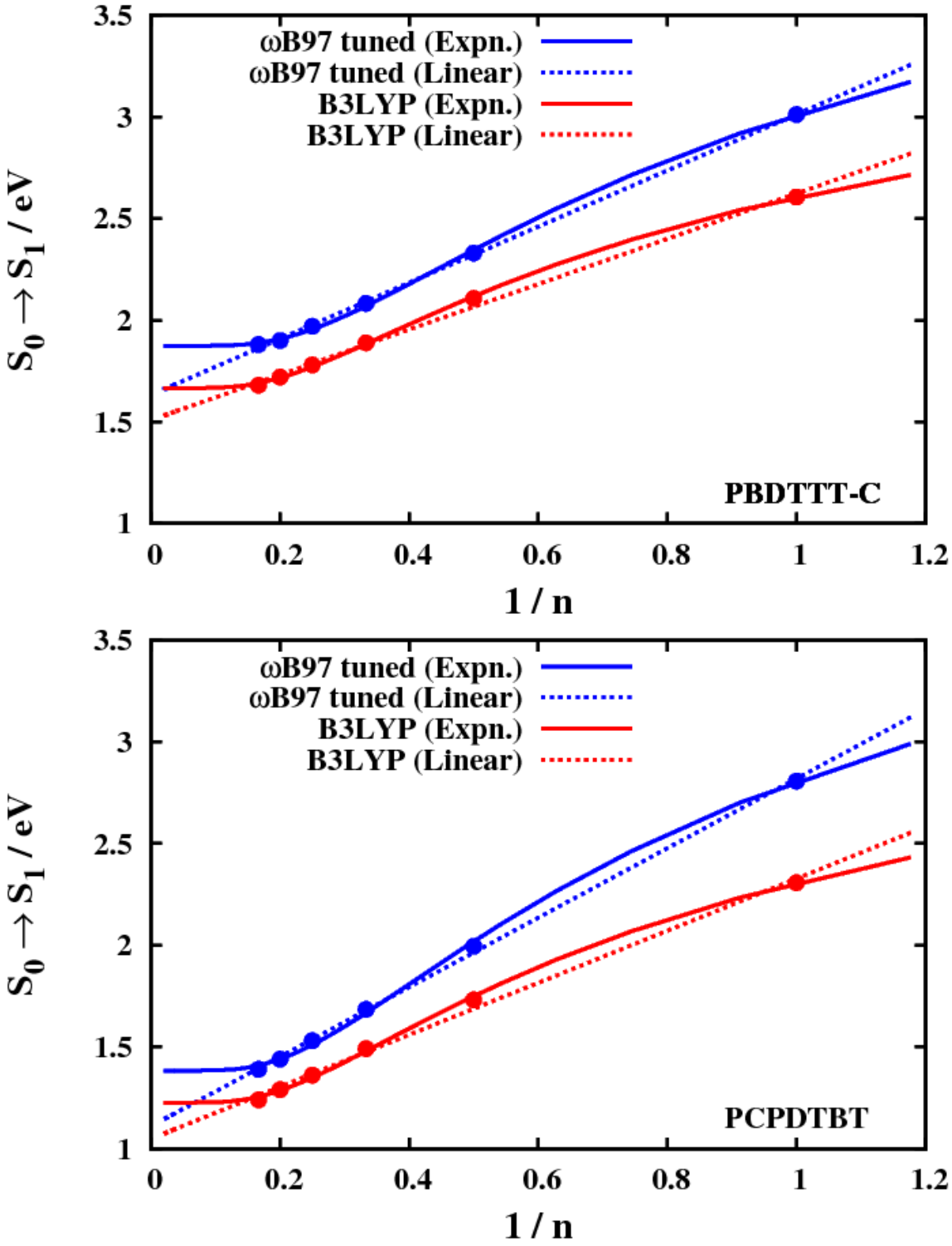

Figure A.4.2 Evolution of the first transition energy ($S_0 \rightarrow S_1$) with respect to inverse number of repeat units (1/n) for PBDTTT-C and PCPDTBT at the TD-DFT level for the B3LYP and tuned ωB97 functionals. Extrapolations of the $S_0 \rightarrow S_1$ energy using linear and exponential fits are also included.

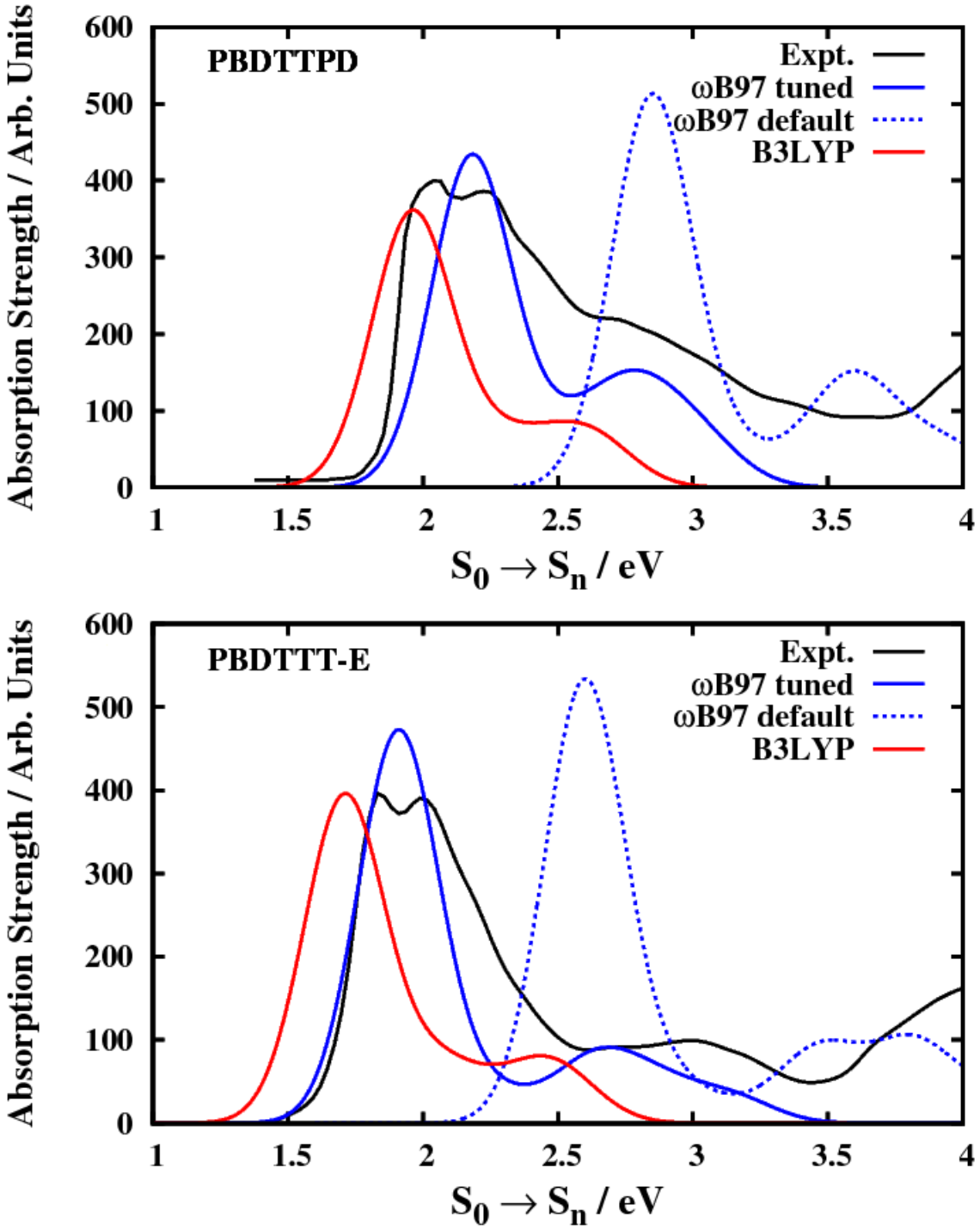

Figure A.4.3 Calculated optical absorption spectra from ωB97 (default and tuned ω) and B3LYP for the isolated hexamers of PBDTTPD and PBDTTT-E compared to the digitized experimental data.

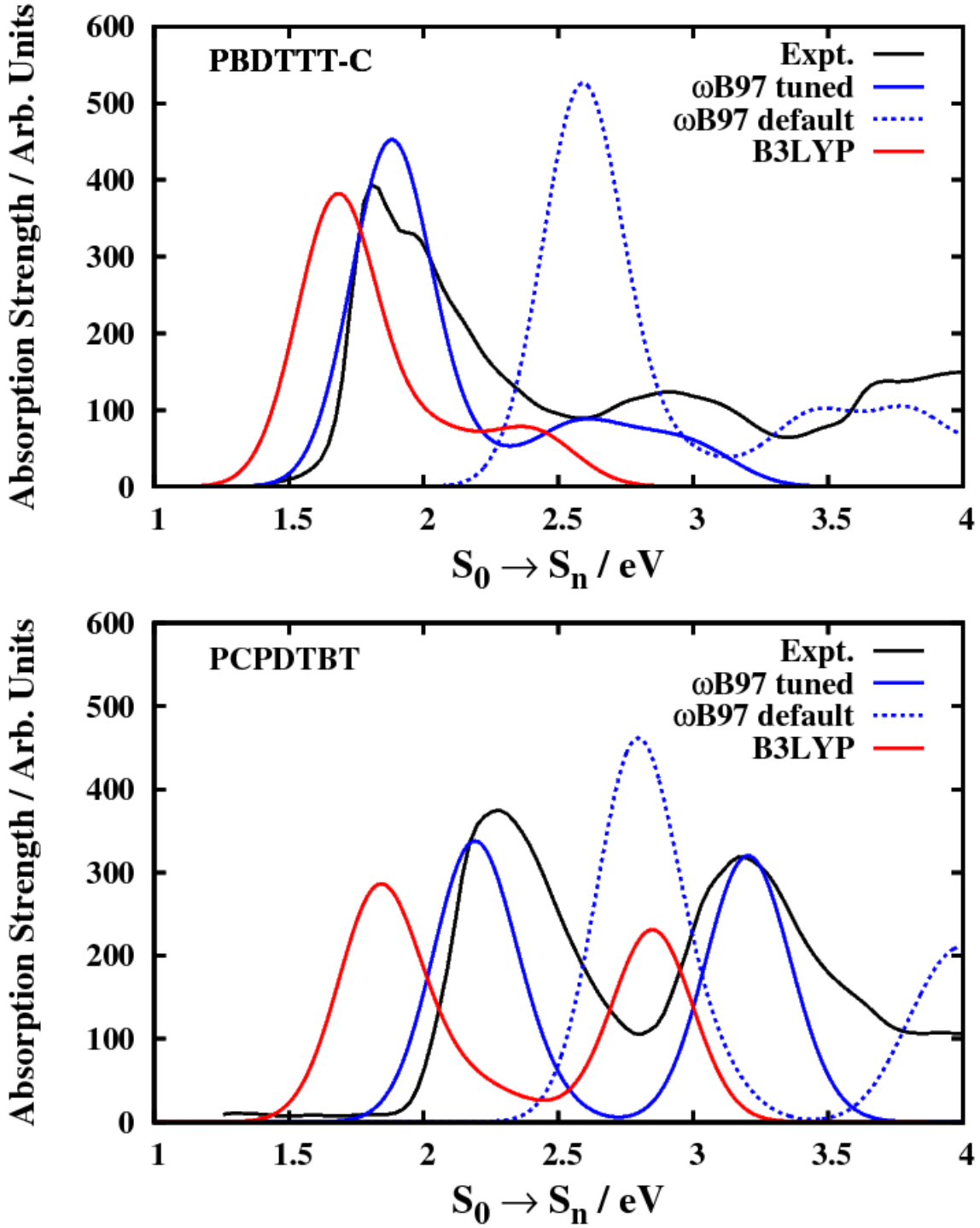

Figure A.4.4 Calculated optical absorption spectra from ωB97 (default and tuned ω) and B3LYP for the isolated hexamers of PBDTTT-C and PCPDTBT compared to the digitized experimental data.

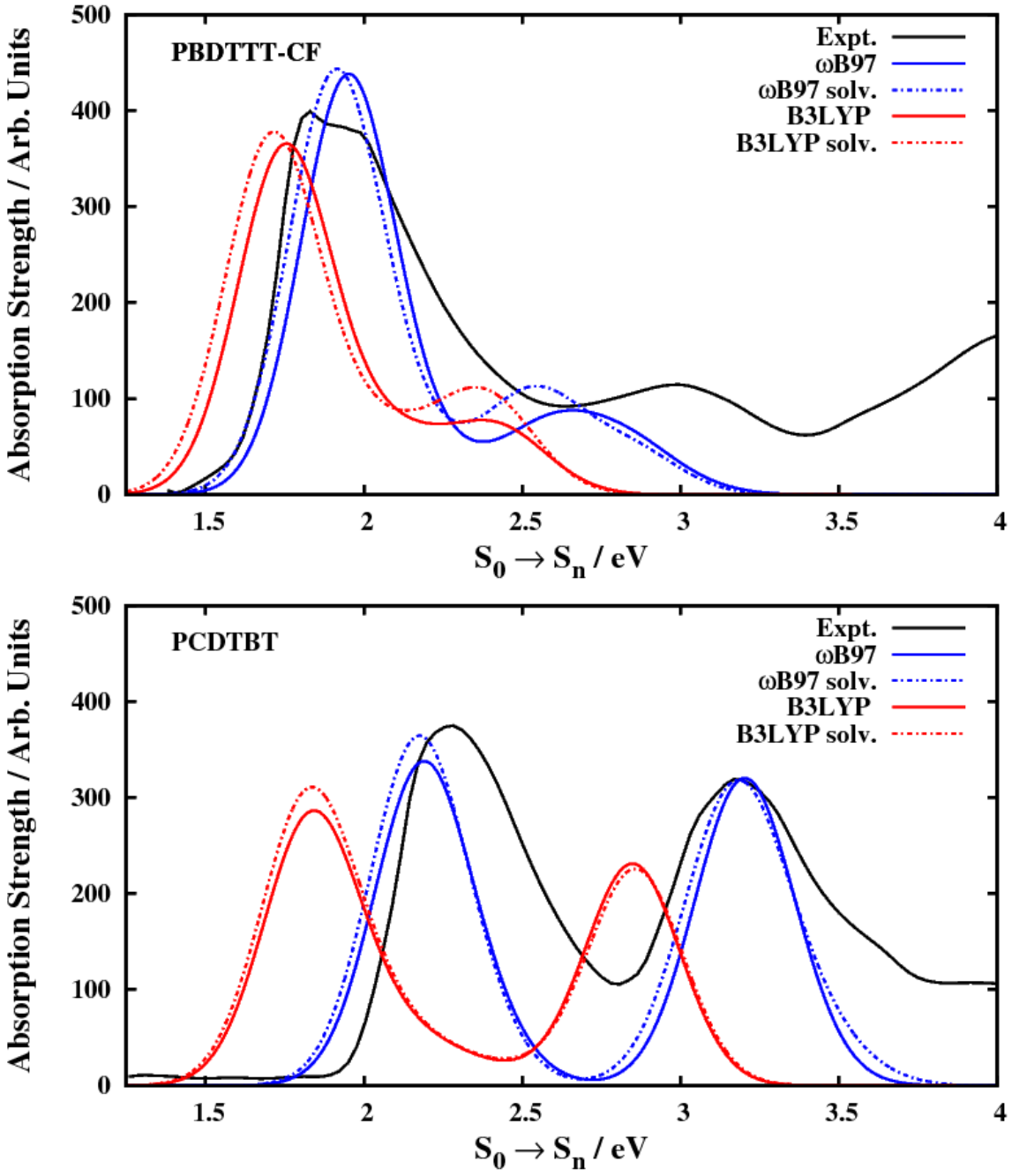

Figure A.4.5 Calculated gas-phase and solvent environment optical absorption spectra from tuned ωB97 and from B3LYP for the hexamer of PBDTTT-CF and tetramer of PCDTBT, compared to the digitized experimental data.

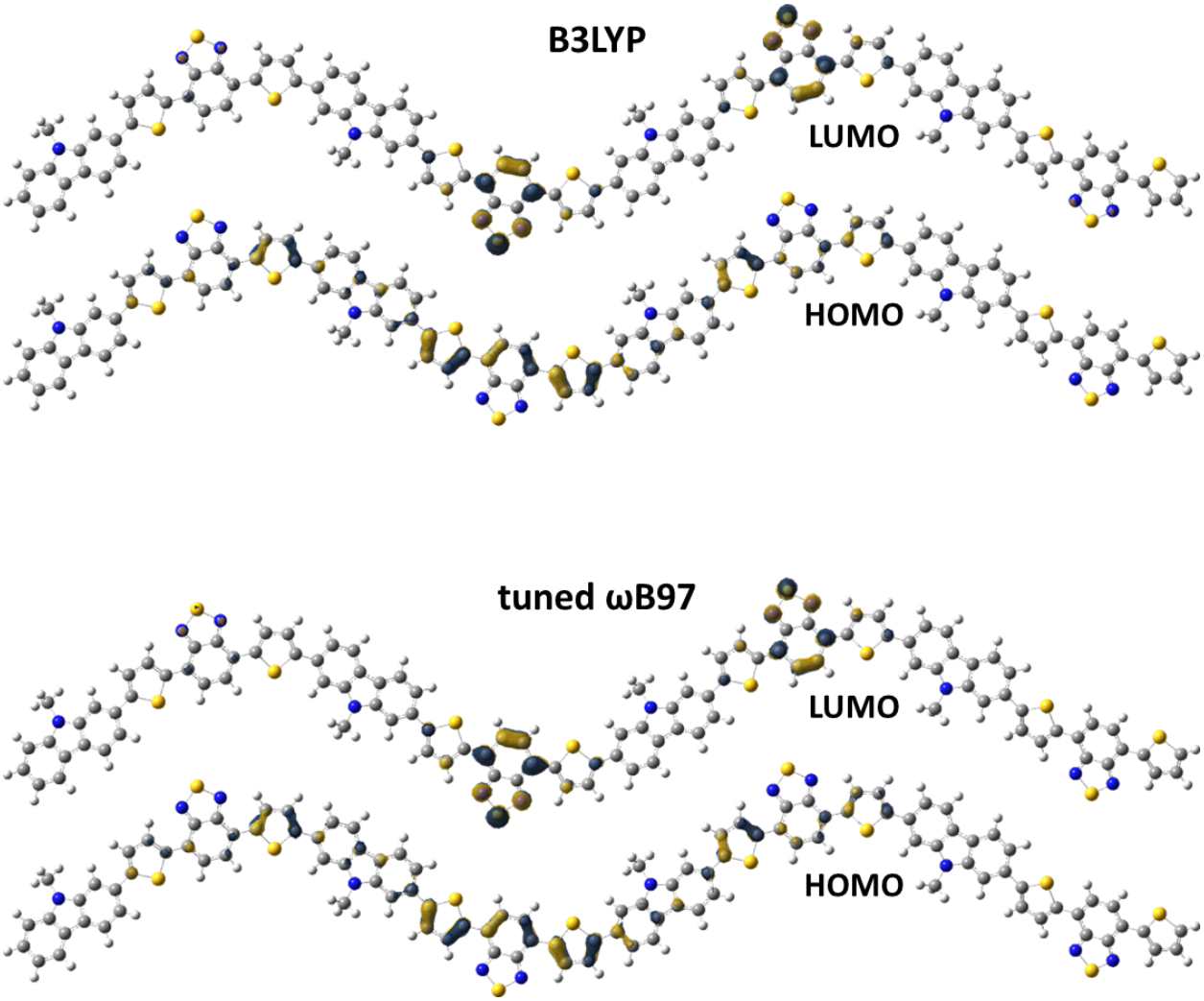

Figure A.4.6 Illustration of the qualitatively similar HOMO and LUMO wave functions (isovalue surface 0.03 a.u.) in the tetramer of PCDTBT for B3LYP and tuned ωB97.

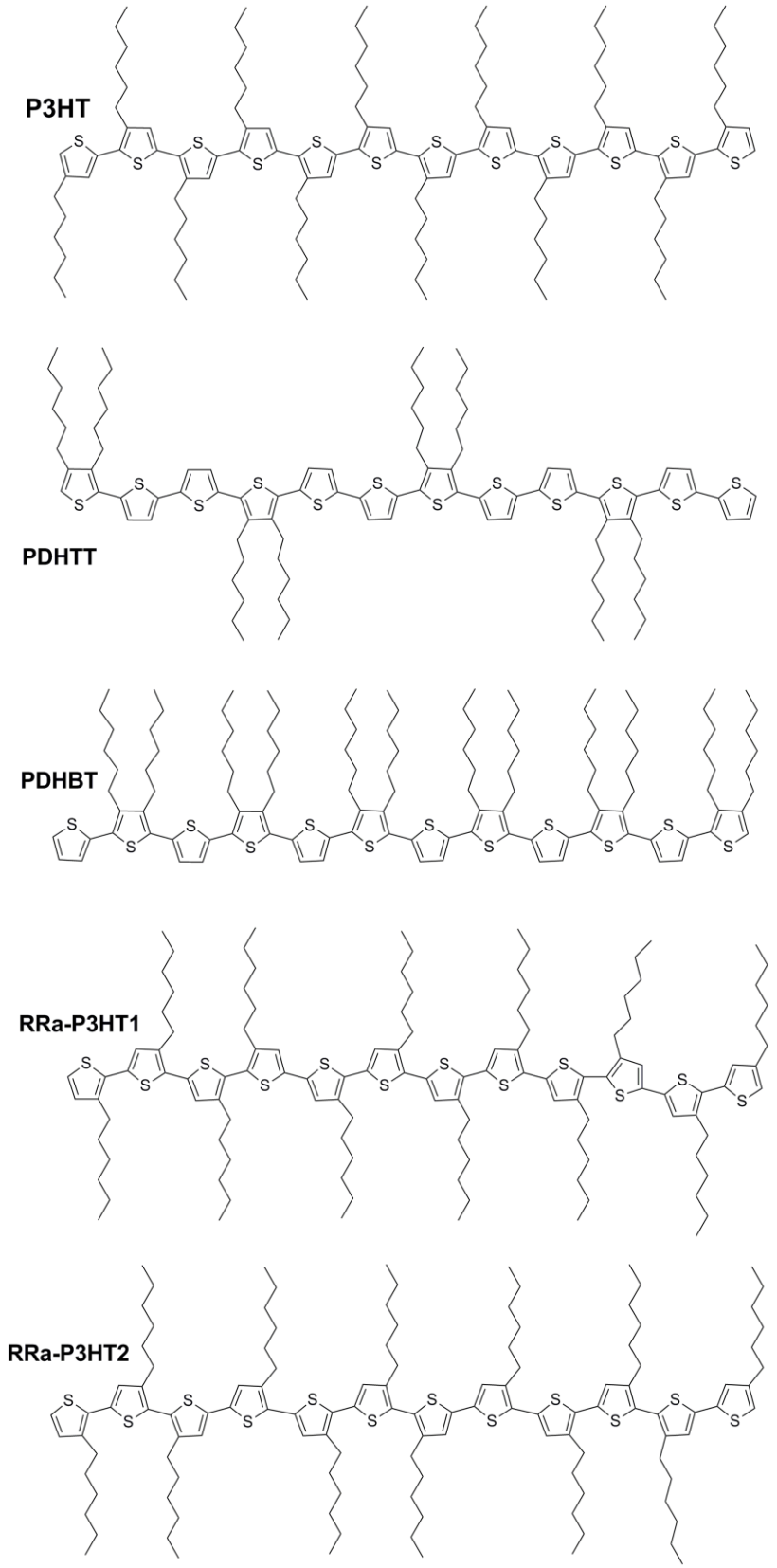

Figure A.5.1 Chemical structures of the systems considered in the DFT calculations.

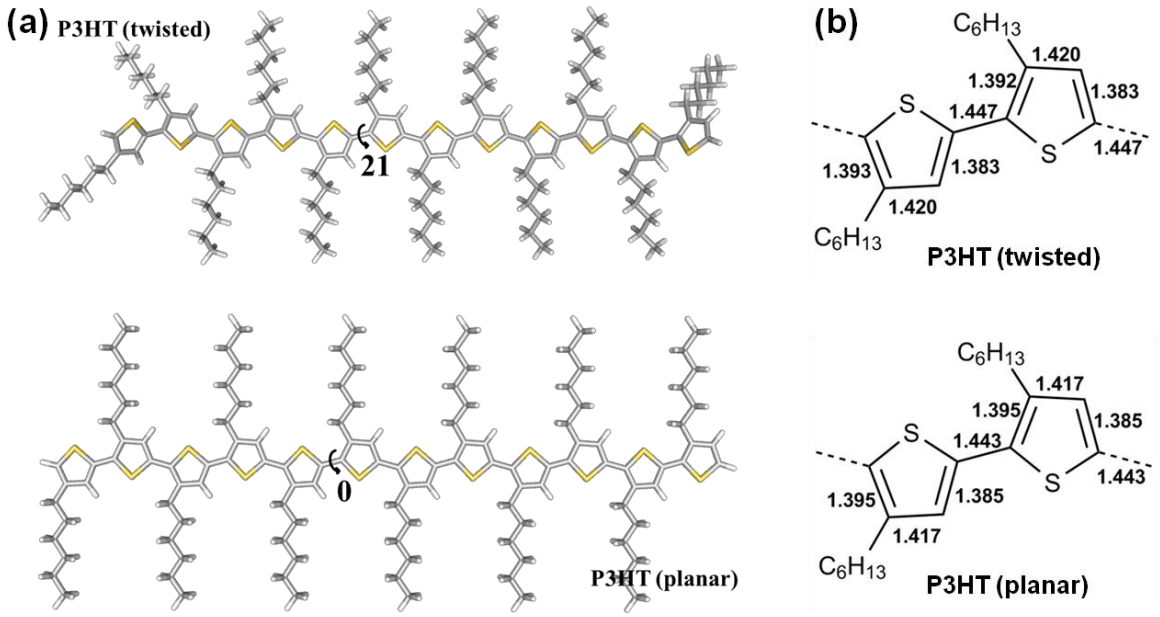

Figure A.5.2 (a) Illustrations of the optimized geometries and dihedral angles for regio-regular **P3H**T calculated at the B3LYP/6-31G(d,p) level of theory. The **P3HT**-twisted oligomer is 3.31 kcal/mol more stable than P3HT-planar. (b) Carbon-carbon bond lengths in the central portion of the structures as determined at the B3LYP/6-31G(d,p) level.

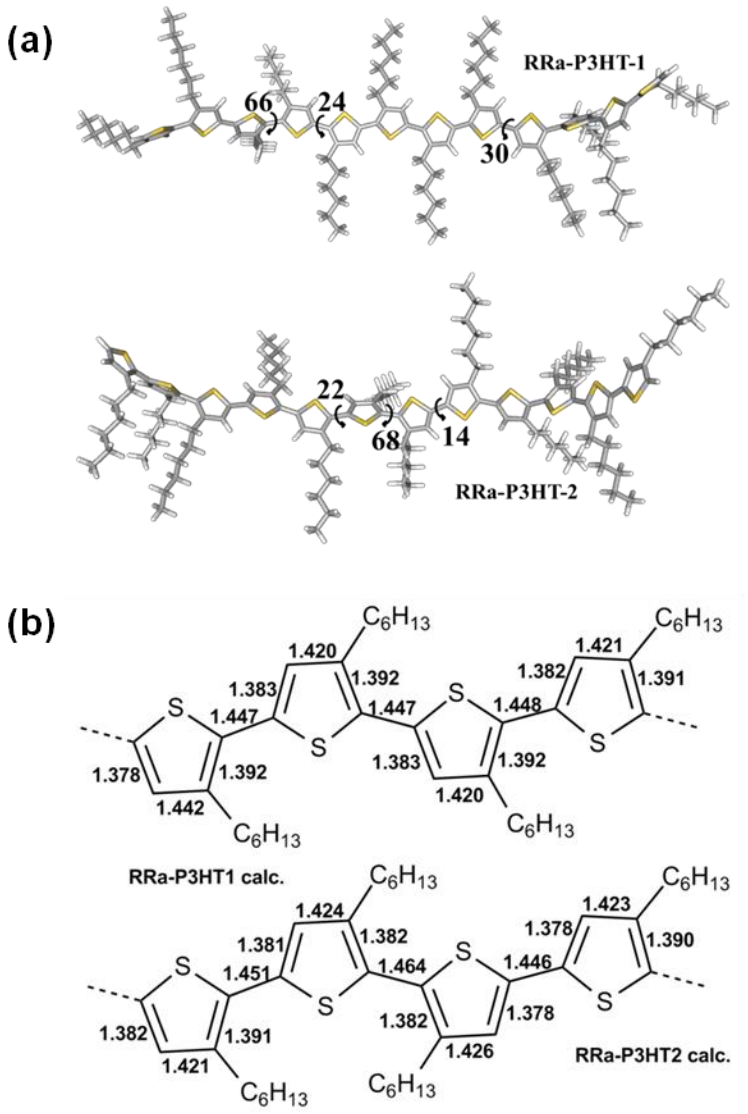

Figure A.5.3 (a) Illustrations of the optimized geometries and dihedral angles for regio-random **P3HT** calculated at the B3LYP/6-31G(d,p) level of theory. The **RRa-P3HT-2** oligomer is 1.22 kcal/mol more stable than **RRa1-P3HT-1**. (b) Carbon-carbon bond lengths in the central portion of the structures as determined at the B3LYP/6-31G(d,p) level.

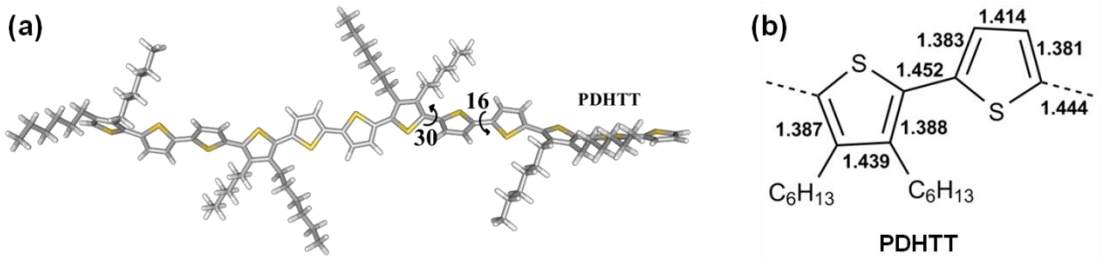

Figure A.5.4 (a) Illustrations of the optimized geometries and dihedral angles for the **PDHTT** oligomer calculated at the B3LYP/6-31G(d,p) level of theory. (b) Carbon-carbon bond lengths in the central portion of the structures as determined at the B3LYP/6-31G(d,p) level.

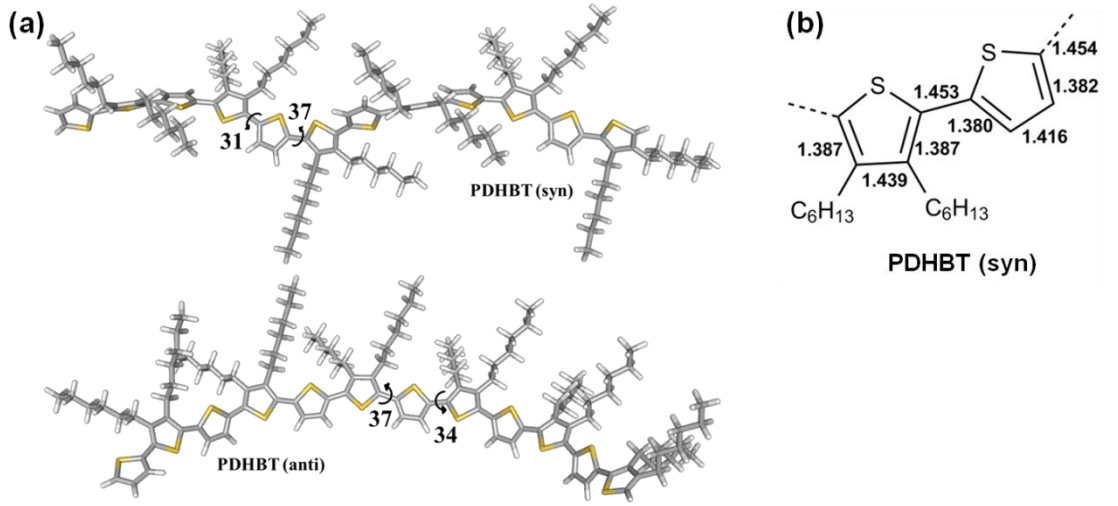

Figure A.5.5 (a) Illustrations of the optimized geometries and dihedral angles for isomers of **PDHBT** calculated at the B3LYP/6-31G(d,p) level of theory. The **PDHBT**-*syn* oligomer is 1.43 kcal/mol more stable than **PDHBT**-*anti*. (b) Carbon-carbon bond lengths in the central portion of the structures as determined at the B3LYP/6-31G(d,p) level.

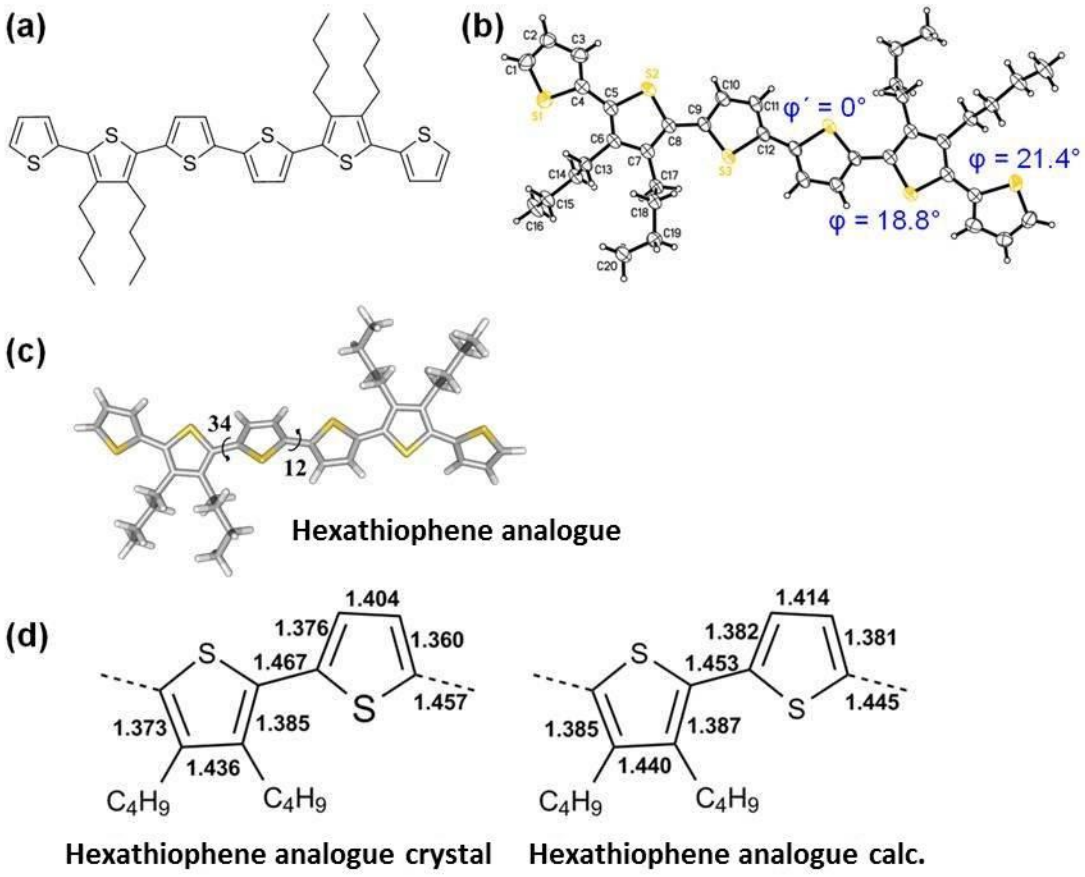

Figure A.5.6 (a) Chemical structure and (b) X-ray crystal structure of hexamer analog of PDHTT φ and φ′ are dihedral angles. (c) Illustrations of the optimized geometries and dihedral angles of hexathiophene analogue calculated at the B3LYP/6-31G(d,p) level of theory. (d) Carbon-carbon bond lengths in the central portion of the structures for the hexathiophene analogues.

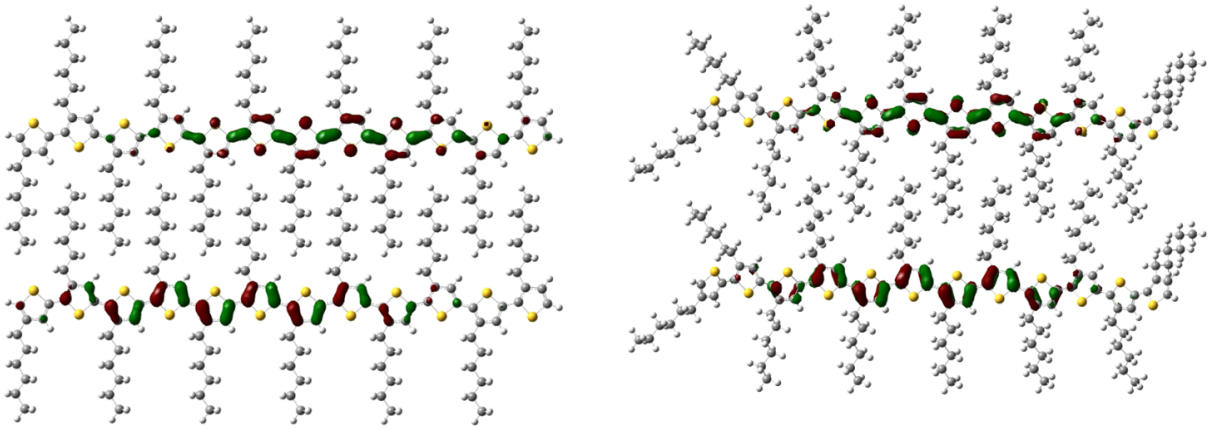

Figure A.5.7 Illustration of the HOMO (bottom) and LUMO (top) wavefunctions of P3HT (planar) [left] and P3HT (twisted) [right] calculated at B3LYP/6-31G(d,p) level.

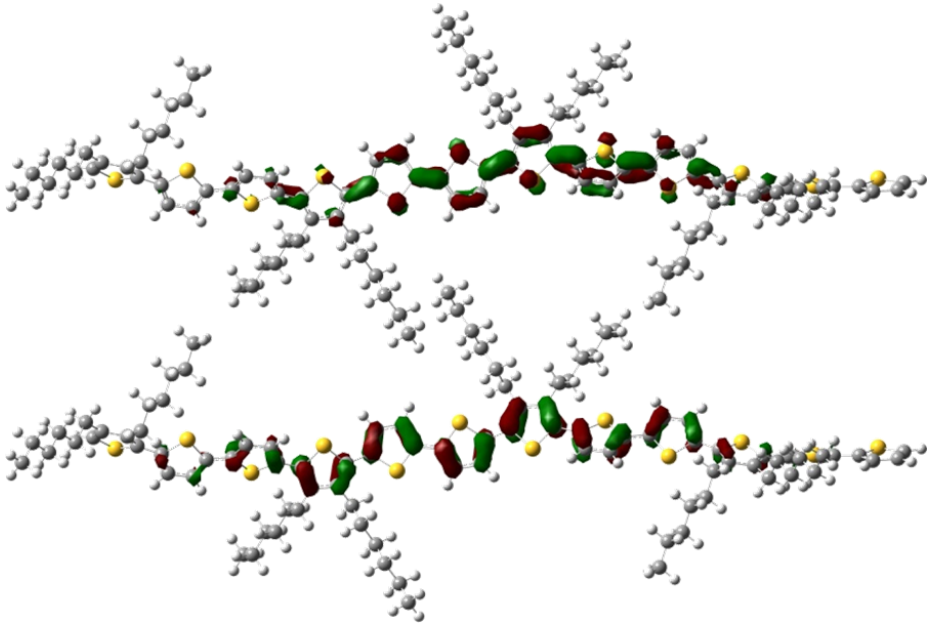

Figure A.5.8 Illustration of the HOMO (bottom) and LUMO (top) wavefunctions of PDHTT calculated at B3LYP/6-31G(d,p) level.

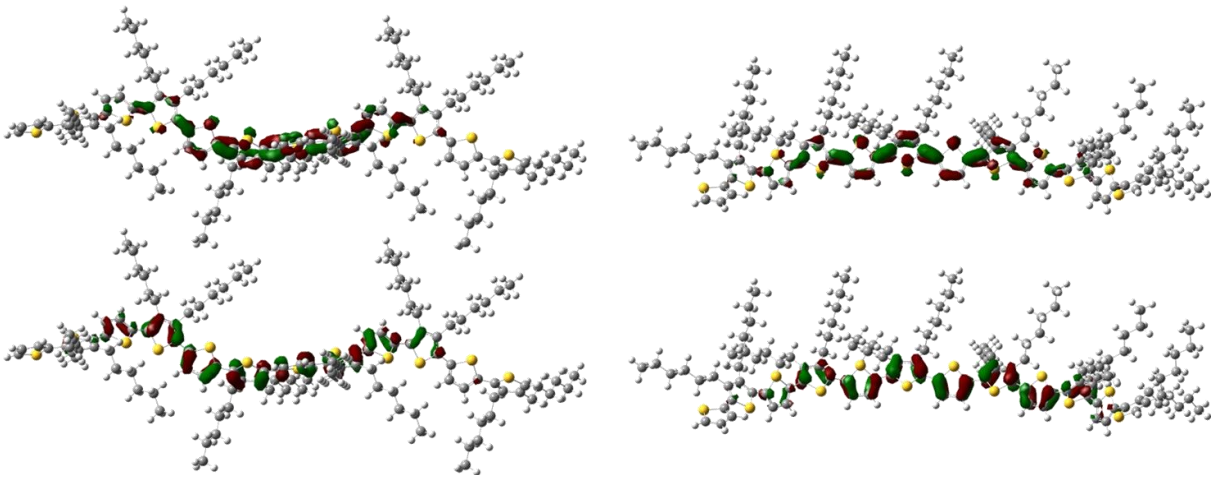

Figure A.5.9 Illustration of the HOMO (bottom) and LUMO (top) wavefunctions for two confirmations of PDHBT calculated at B3LYP/6-31G(d,p) level: *syn*-confirmation (left) and *anti*-confirmation (right).

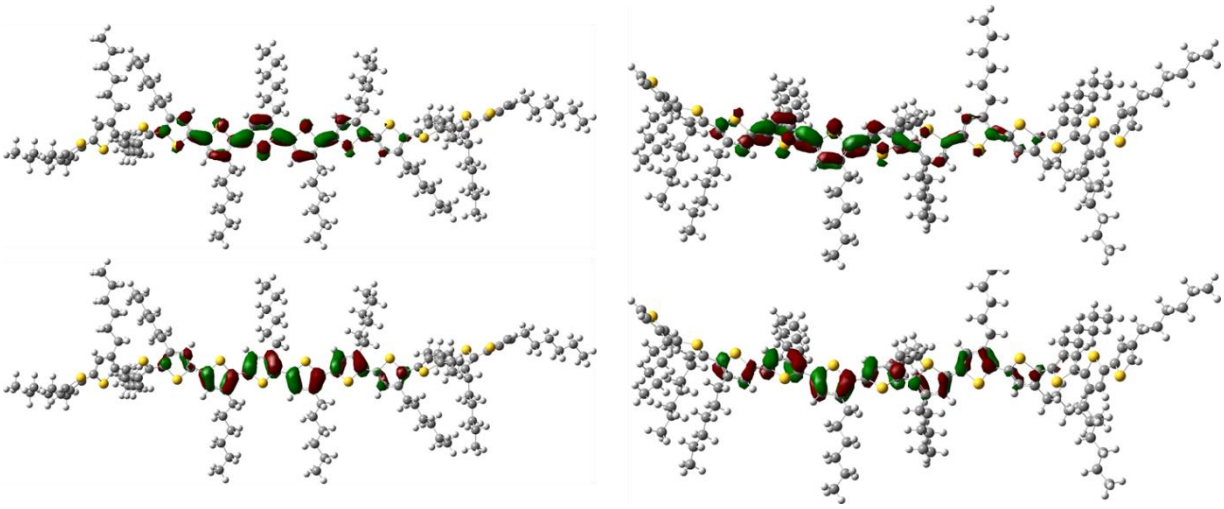

Figure A.5.10 Illustration of the HOMO (bottom) and LUMO (top) wavefunctions of regio-random P3HT calculated at B3LYP/6-31G(d,p) level, RRa-P3HT-1 (left) and RRa-P3HT-2 (right).

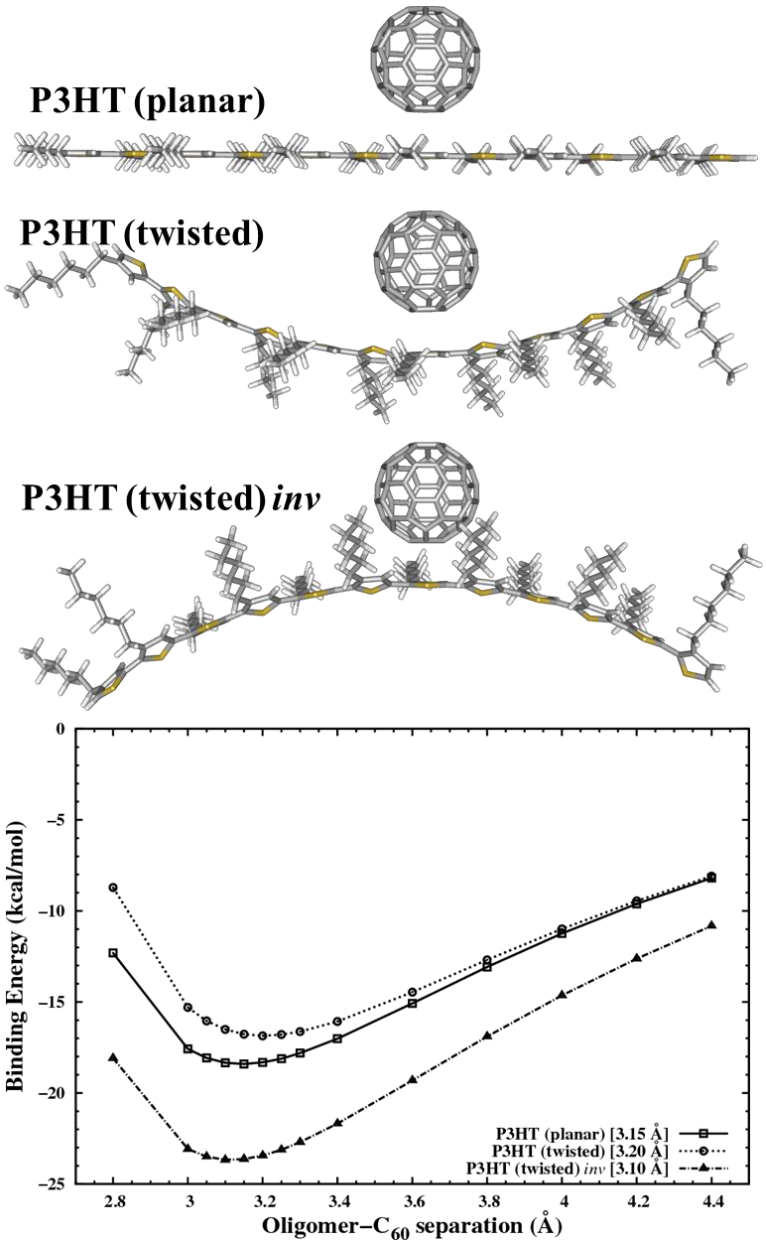

Figure A.5.11 P3HT−C_{60} interactions: Geometry and binding energy with respect to infinite separation distance. The separation distance at the largest binding energy is included in the legend.

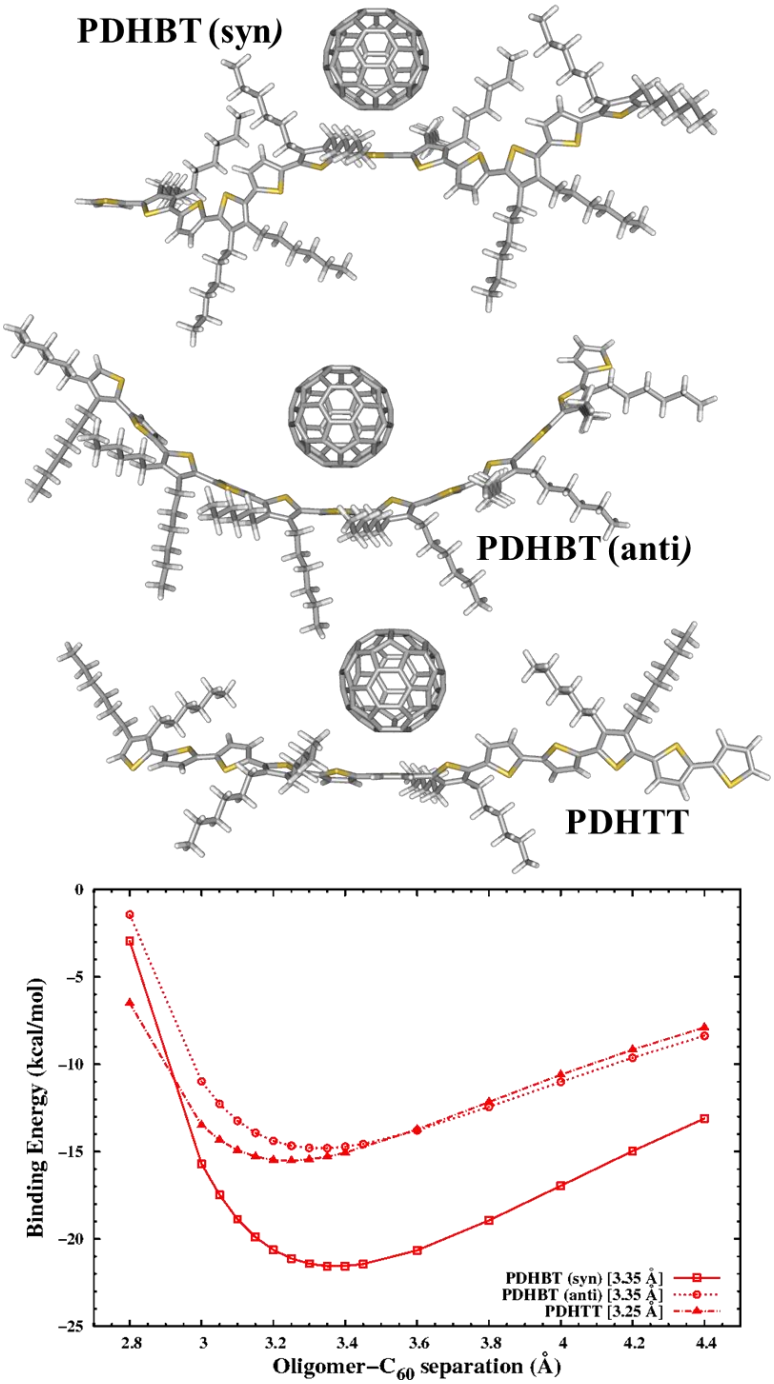

Figure A.5.12 PDHBT−C_{60} and PDHTT−C_{60} interactions: Geometry and binding energy with respect to infinite separation distance. The separation distance at the largest binding energy is included in the legend.

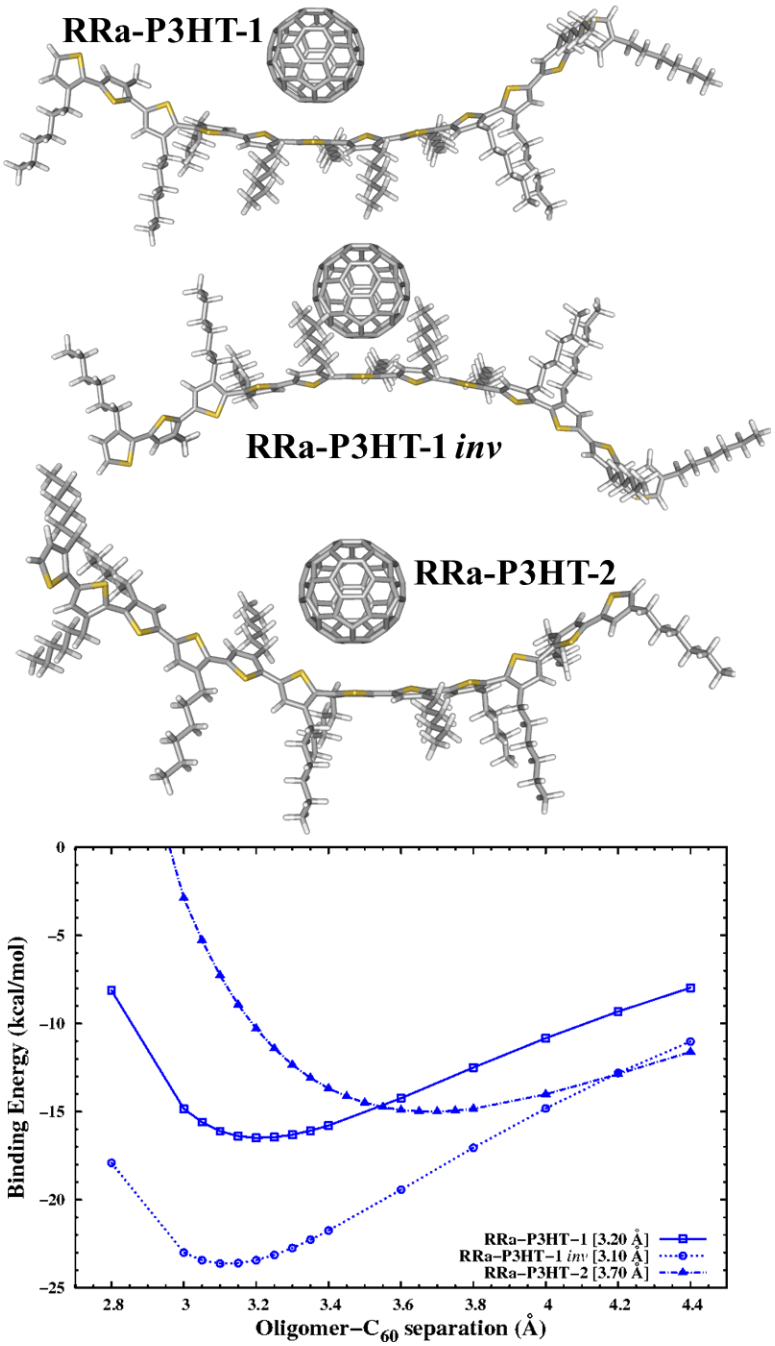

Figure A.5.13 RRa-P3HT−C_{60} interactions: Geometry and binding energy with respect to infinite separation distance. The separation distance at the largest binding energy is included in the legend.

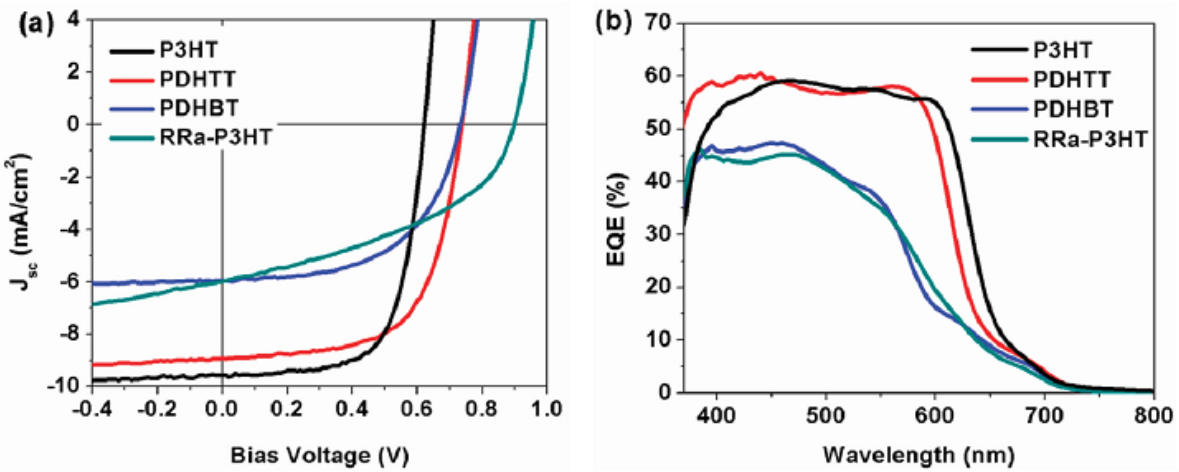

Figure A.5.14 Current-voltage plots under illumination with 1.5G solar simulated light and (b) external quantum efficiency (EQE) for polymer:$PC_{71}BM$ bulk heterojunction solar cells.

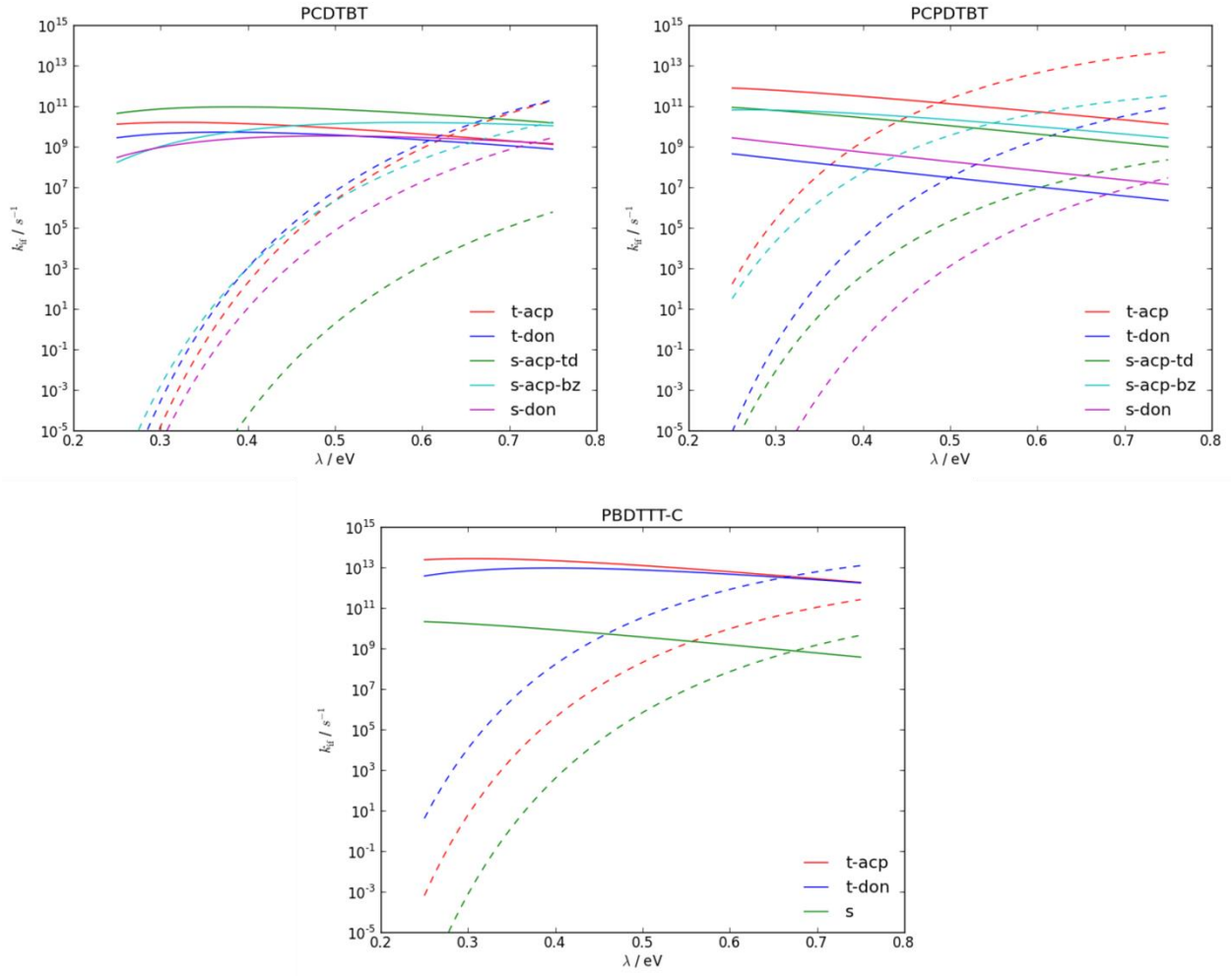

Figure A.6.1 Charge-transfer and charge-recombination rates as a function of reorganization energy for dyads including oligomers PCDTBT, PCPDTBT, and PBDTTT-C.